Department of Electronics and Nanoengineering

Characterizing Multipath Radio Environments for 5G Wireless Systems and Beyond

Usman Tahir Virk

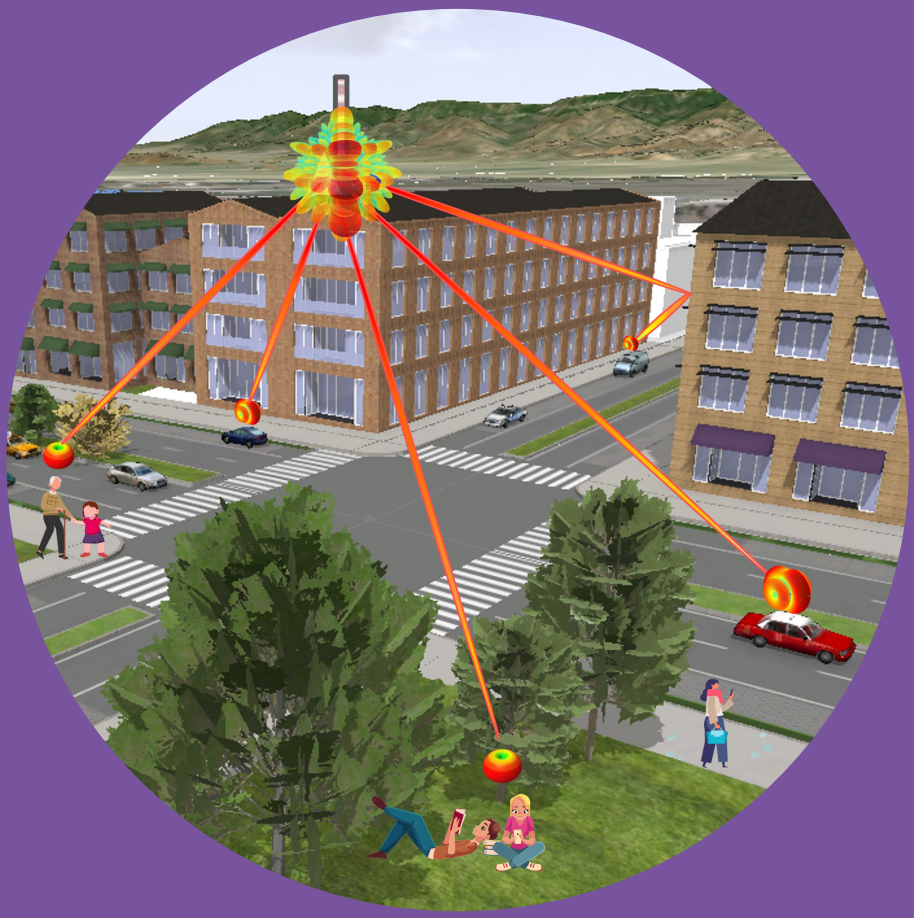

Aalto University

DOCTORAL THESES

Aalto University publication series
DOCTORAL THESES 136/2023

Characterizing Multipath Radio Environments for 5G Wireless Systems and Beyond

Usman Tahir Virk

A doctoral thesis completed for the degree of Doctor of Science (Technology) to be defended, with the permission of the Aalto University School of Electrical Engineering, at a public examination held at the lecture hall AS1 of the school on 29 September 2023 at 12 pm.

Aalto University
School of Electrical Engineering
Department of Electronics and Nanoengineering
Antennas and Propagation

Supervising professors
Prof. Ville Viikari, Aalto University, Finland (Until Oct. 2013)
Assoc. Prof. Katsuyuki Haneda, Aalto University, Finland (Since Oct. 2013)

Thesis advisor
Assoc. Prof. Katsuyuki Haneda, Aalto University, Finland
Assoc. Prof. Jean-Frederic Wagen, HEIA-FR, Switzerland (Until Dec. 2015)

Preliminary examiners
Assoc. Prof. Christopher Anderson, United States Naval Academy, USA
Prof. Torbjorn Ekman, Norwegian University of Science and Technology (NTNU), Norway

Opponent
Prof. Luis M. Correia, IST University of Lisbon, Portugal

Aalto University publication series
DOCTORAL THESES 136/2023

ISBN 978-952-64-1408-9 (printed)
ISBN 978-952-64-1409-6 (pdf)
ISSN 1799-4934 (printed)
ISSN 1799-4942 (pdf)
http://urn.fi/URN:ISBN:978-952-64-1409-6

Unigrafia Oy
Helsinki 2023

Finland

NORDIC SWAN ECOLABEL
Printed matter
4041-0619

Author
Usman Tahir Virk

Name of the doctoral thesis
Characterizing Multipath Radio Environments for 5G Wireless Systems and Beyond

Publisher School of Electrical Engineering

Unit Department of Electronics and Nanoengineering

Series Aalto University publication series DOCTORAL THESES 136/2023

Field of research Radio Engineering

Manuscript submitted 18 December 2022 **Date of the defence** 29 September 2023

Permission for public defence granted (date) 27 June 2023 **Language** English

☐ **Monograph** ☒ **Article thesis** ☐ **Essay thesis**

Abstract

The envelope of performance in Fifth generation (5G) technology will be much greater than what we see in legacy technologies, featuring low latency, ultra-high data rates, massive connectivity, and increased security. 5G wireless systems operating in centimeter (cm) and millimeter (mm) wave parts of the frequency spectrum must deal with all sorts of radio wave propagation conditions imposed by a radio channel. This entails thoroughly characterizing radio channels across the desired frequency range for efficient system design and performance. The primary focus of this thesis is (1) to model the interaction of radio waves with material objects in radio environments, and (2) to characterize multipath radio channels at cmWave and mmWave frequencies. The key contributions of the thesis are summarized as follows. First, a comprehensive evaluation of transmission and reflection losses for material objects in built environments is carried out at the 70 GHz frequency band. The results demonstrate that energy-efficient building windows, laminated plywood, and plasterboard are good reflectors of mmWave signals, while humans and some energy-efficient windows attenuate mmWave signals as high as 40 dB. Second, a novel method is proposed for the on-site estimation of the permittivity of built-in materials using the point cloud geometrical database and limited channel measurements of a given radio environment. The estimated material permittivities of a large indoor office are visualized through a colored three-dimensional (3D) point cloud map of the environment. Third, human blockage losses are measured through anechoic chamber measurements for 15 human subjects with different weights and sizes at 15, 28, and 60 GHz frequency bands. Moreover, a novel double-truncated multiple knife-edge (DTKME) model is proposed that reasonably predicts the measured human blockage loss for different body orientations and illuminating antenna heights. Fourth, the feasibility of applying full-wave numerical techniques for coverage predictions is determined by finite-difference time-domain (FDTD) simulations for the coverage analysis inside a small indoor office. It is transpired that the full-wave methods are computationally expensive, and a trade-off exists between the accuracy and complexity of these simulations. Finally, multipath characterization of cmWave and mmWave radio channels is performed for indoor and outdoor radio environments in terms of their power, delay, and angular domain behavior. The fluctuations in the signal envelope of mmWave channels are more significant than their cmWave counterparts. The mmWave channels exhibit less delay dispersion compared to cmWave radio channels. The spatial spread of multipath is similar in line-of-sight (LOS) conditions across cmWave and mmWave radio channels, while in non-LOS (NLOS) propagation conditions, the cmWave radio channels offer more spatial spread of multipath than mmWave radio channels.

Keywords centimeter wave, millimeter wave, human blockage, point cloud, permittivity map, channel modeling

ISBN (printed) 978-952-64-1408-9 **ISBN (pdf)** 978-952-64-1409-6

ISSN (printed) 1799-4934 **ISSN (pdf)** 1799-4942

Location of publisher Helsinki **Location of printing** Helsinki **Year** 2023

Pages 226 **urn** http://urn.fi/URN:ISBN:978-952-64-1409-6

To My Mom and Dad

Preface

"In the name of Allah, Most Gracious, Most Merciful."

— Al-Quran, 1:1

I was always fascinated by telephony in my early childhood, and as I grew, this inquisitiveness and curiosity delved deeper in me, thriving and only ceasing on the day I die. It's a great blessing of Allah that I have been able to pursue knowledge in the field of my interest. For all the learning opportunities and felicities in life, the most exalted words I can recite are:

"Praise be to Allah, The Cherisher and Sustainer of the Worlds."

— Al-Quran, 1:2

The evolution of wireless communication technologies over the past few decades has been an incredible journey from basic voice calls to the high-speed, interconnected world of 5G and beyond. Each generation has built upon the previous one, ushering in new possibilities and transforming the way we communicate and interact with the world around us. This thesis embarks on an expedition into the heart of wireless communication's hidden hero – the radio channel. It explores the science that makes the ethereal tangible, the mathematics that turns the problems into solutions and the innovations that are emerged from understanding. As it navigates the intricacies of radio channel characterization and modeling, we gain not only insight into the technical prowess that shapes our connected world but also a profound appreciation for the symphony of invisible signals playing out silently in our surroundings. As Guglielmo Marconi rightly said, *"In the new era, thought itself will be transmitted by radio."*

My endeavors for higher education got their true inspiration when I met Late Prof. Pertti Vainikainen who mentored our first batch of international master's degree students. Pertti was the epitome of knowledge and

kindness. May he rest in peace. My doctoral supervisor Prof. Katsuyuki Haneda deserves my deepest gratitude. It is due to his constant support and guidance, great patience, commendable knowledge and expertise, and constructive feedback and mentoring that I have been able to research some very interesting topics during my doctoral studies, some of which led us to win three best paper awards. He also provided me with opportunities for research collaboration and supported my international visits to HEIA Fribourg, Switzerland, the University of Southern California (USC), USA, and COST IC1004 meetings. I am grateful to Prof. Ville Viikari for officially supervising the first few months of my doctoral studies. I would also like to thank Prof. Jean-Frederic Wagen of HEIA for advising and funding part of my studies. I am grateful to Prof. Andreas Molisch for hosting my research visits at USC and it was great to work alongside his team. I extend my gratitude to the preliminary examiners of this thesis, Prof. Chris Anderson and Prof. Torbjon Ekman, for their thorough and thought-provoking inputs that improved the quality of this thesis. I am grateful to Prof. Luis M. Correia for acting as the Opponent of my thesis defense.

Thanks to Prof. Antti Raisanen, the former head of the department, who has always encouraged and guided me. I would also like to acknowledge all professors and teachers who taught us with utmost diligence and created an enabling environment for learning. I appreciate my former colleagues and fellow researchers, Dr. Veli-Matti Kolmonen, Dr. Afroza Khatun, Prof. Azremi Abdullah Al-Hadi, Dr. Jan Jarvelainen, Dr. Sathya Narayana, Dr. Aki Kartunen, Dr. Sinh Nguyen, Dr. Mikko Heino, Md. Suzan Miah and others for their delightful camaraderie, insightful discussions, and collaborative spirit that enriched my research experience. The former and current administrative and laboratory staff at our department, Lorenz, Eikka, Matti, Timo, and all others, deserve a special mention for their seamless assistance and coordination. The resources and facilities provided by Aalto University were instrumental in the successful completion of this research, and I am pleased with their firm commitment to academic excellence. I am thankful to the Nokia Foundation for awarding me the Scholarship. I would also like to express my earnest gratitude and respect to my current team at Keysight Technologies, especially Dr. Pekka Kyosti, Jukka Kyrolainen, Lassi Hentila, Dr. Antti Rovainen, and Dr. Essi Suikkanen, for their knowledge and expertise, professionalism, ingenuity, trustworthiness, teamwork, and kindness. I can proudly say

that they are some of the best people I have ever worked with. I also like to thank my friend and colleague Dr. Md. Mazidul Islam for all the positive conversations we had over the years. His willingness to lend an ear during moments of doubt has been invaluable.

As I reach the culmination of this arduous journey, my heart overflows with profound gratitude for the unwavering love, immense support, continuous encouragement, and guidance I have received from my dear mom, Shahida Saeed, and dad Dr. Amjad Virk at every step of life. They are the reason I could reach this far. Their countless efforts and sacrifices made me worthy of being the man I am today. The values they instilled in me have been a foundation upon which my life is built and pulled me straight every time I staggered. The presence of my siblings, Dr. Sana Virk, Zeeshan Virk, and Dr. Shiza Virk, in my life has always been a source of strength, motivation, and inspiration. Their faith in my abilities has been my guiding light. Finally, I would like to say fervent and heartfelt thanks to my beloved wife, Rabia Jabeen, for her steadfast belief in my capabilities, unending patience, staunch support, and ardent love and affection that provided me strength to persevere through challenges and setbacks. My precious children, Umar Virk, Zainab Virk, and Ayesha Virk, have filled my life with joy and happiness with their boundless energy, innocence, and smiles. I conclude by saying that if sanity prevails, adversity becomes a partner in a person's progress so one should never lose hope and courage.

Oulu, Finland, September 11, 2023,

Usman Tahir Virk

Contents

List of Publications

This thesis is an overview of the following publications, referred to in the text with upper case Roman numerals.

I U. T. Virk, K. Haneda, V-M. Kolmonen, P. Vainikainen, and Y. Kaipainen. Characterization of vehicle penetration loss at wireless communication frequencies. In *Proc. 8th European Conference on Antennas and Propagation (EuCAP'14)*, The Hague, Netherlands, April 2014.

II U. T. Virk, J-F. Wagen, and K. Haneda. Simulating specular reflections for point cloud geometrical database of the environment. In *Proc. Loughborough Antennas and Propagation Conference (LAPC'15)*, Loughborough, UK, November 2015.

III U. T. Virk, K. Haneda, and J. Putkonen. Estimating reflection and transmission losses for link-obstructing objects at 70 GHz for 5G wireless backhauling. In *Proc. Loughborough Antennas and Propagation Conference (LAPC'18)*, Loughborough, UK, November 2018.

IV U. T. Virk, S. L. H. Nguyen, K. Haneda, and J-F. Wagen. On-site permittivity estimation at 60 GHz through reflecting surface identification in the point cloud. *IEEE Transactions on Antennas and Propagation*, vol. 66, no. 7, pp. 3599–3609, July 2018.

V U. T. Virk and K. Haneda. Modeling human blockage at 5G millimeter-wave frequencies. *IEEE Transactions on Antennas and Propagation*, vol. 68, no. 3, pp. 2256–2266, March 2020.

VI U. T. Virk, K. Haneda, V-M. Kolmonen, J-F. Wagen, and P. Vainikainen. Full-wave characterization of indoor office environment for accurate coverage analysis. In *Proc. International Conference on Electromagnetics in Advanced Applications (ICEAA'13)*, Turin, Italy, September

2013.

VII U. T. Virk, S. L. H. Nguyen, and K. Haneda. Multi-frequency power angular spectrum comparison for an indoor environment. In *Proc. 11th European Conference on Antennas and Propagation (EuCAP'17)*, Paris, France, April 2017.

VIII S. Sangadoyin, U. T. Virk, D. Burghal, K. Haneda, and A-F. Molisch. Joint characterization of mm-wave and cm-wave device-to-device fading channels. In *Proc. Military Communications Conference (MILCOMM'18)*, Los Angeles, USA, October 2018.

Author's Contribution

Publication I: "Characterization of vehicle penetration loss at wireless communication frequencies"

The study of vehicle penetration loss was part of the research collaboration between Renesas Mobile and Aalto University. The author contributed to the planning of radio channel measurements that were jointly conducted by the author, Prof. Katsuyuki Haneda, and Dr. Veli-Mati Kolmonen. The author was responsible for simulations, analysis, and writing of the manuscript. Prof. Katsuyuki Haneda contributed to the analysis and supervised the work.

Publication II: "Simulating specular reflections for point cloud geometrical database of the environment"

The author and Prof. Katsuyuki Haneda identified the problem of insufficient prediction accuracy for specular reflections in the point cloud for large environments with dominant specular multipath. The author and Prof. Jean-Frederic Wagen jointly proposed the theoretical formulation for specular reflection modeling in the point cloud of an environment. Prof. Katsuyuki Haneda provided the channel measurement data of a large indoor office environment. The author carried out simulations and analyses. Prof. Jean-Frederic Wagen and Prof. Katsuyuki Haneda supervised the work. The author was responsible for writing the paper.

Publication III: "Estimating reflection and transmission losses for link-obstructing objects at 70 GHz for 5G wireless backhauling"

The analysis of reflection and transmission properties of typical objects in a radio environment at 70 GHz was part of the research collaboration between Nokia Bell-labs (previously Nokia-Siemens Network) and Aalto University. The author planned and conducted the measurements, performed data analysis, and was responsible for writing the manuscript. Prof. Katsuyuki Haneda assisted the measurements and supervised the work.

Publication IV: "On-site permittivity estimation at 60 GHz through reflecting surface identification in the point cloud"

Prof. Katsuyuki Haneda contrived the idea of on-site permittivity estimation and generating a 3D point cloud permittivity map of a given radio environment. The author and Prof. Katsuyuki Haneda jointly developed the methodology. Prof. Katsuyuki Haneda provided the measurement data of a large indoor office environment. Dr. Sinh Nguyen assisted with the channel parameter estimation from the measurement data. The author carried out the ray-based point cloud simulations, performed data analysis, and was responsible for writing the manuscript. Prof. Katsuyuki Haneda supervised the work.

Publication V: "Modeling human blockage at 5G millimeter-wave frequencies"

The evaluation of human blockage at mmWave frequencies was included as a potential topic for investigation by Prof. Katsuyuki Haneda and Prof. Andreas Molisch as a part of the research collaboration between Aalto University and the University of Southern California (USC), Los Angeles under the WiFiUS consortium. The idea was refined during the collaborative discussions. The author conducted comprehensive human blockage measurements and carried out data analysis. Prof. Katsuyuki Haneda and the author jointly contributed to the analytical formulation of the proposed human blockage model. The author was responsible for writing the paper. Prof. Katsuyuki Haneda supervised the work.

Publication VI: "Full-wave characterization of indoor office environment for accurate coverage analysis"

Prof. Pertti Vainikainen, Dr. Veli-Matti Kolmonen, and Prof. Katsuyuki Haneda jointly proposed the idea of exploring the feasibility of full-wave numerical simulations for radio wave propagation problems. The author carried out radio channel simulations and analysis for an indoor office environment using a commercially available full-wave finite-difference time-domain (FDTD) simulation software, SEMCAD. Prof. Katsuyuki provided the measurement data for validating the simulations results. The work was instructed by Dr. Veli-Matti Kolmonen and supervised by Prof. Katsuyuki Haneda. The author was responsible for writing the paper.

Publication VII: "Multi-frequency power angular spectrum comparison for an indoor environment"

The idea of comparing power angular spectrum (PAS) for frequency bands below and above 6 GHz to study the angular spread of multipath was proposed by Prof. Katsuyuki Haneda as a part of the collaborative discussions during the WiFiUS project. Dr. Sinh Nguyen assisted with the parameter estimation from the measurement data. The author carried out the analysis and was responsible for writing the paper. Prof. Katsuyuki Haneda supervised the work.

Publication VIII: "Joint characterization of mm-wave and cm-wave device-to-device fading channels"

The author proposed the idea of the joint characterization of mmWave and cmWave device-to-device (D2D) radio channels in an outdoor quad scenario. The author planned and carried out radio channel measurements along with Dr. Seun Sangodoyin, and Dr. Daoud Burghal at Health Campus of University of Southern California (USC) in Los Angeles. Dr. Seun Sangodoyin contributed to the analysis and was responsible for writing the paper.

List of Abbreviations

2D	Two-dimensional
2G	Second generation
3D	Three-dimensional
3G	Third generation
4G	Fourth generation
5G	Fifth generation
6G	Sixth generation
3GPP	Third Generation Partnership Project
5GMF	5G Mobile Communication Promotion
ACF	Auto-correlation function
AMPS	Advanced Mobile Phone System
APS	Angle power spectrum
AR	Augmented reality
ARIB	Association of Radio Industries and Businesses
B2B	Back-to-back
BER	Bit error rate
BS	Base station
CA	Carrier aggregation
CCSA	China Communications Standards Association
CDF	Cumulative distribution function
CDMA	Code Division Multiple Access
cmWave	Centimeter wave
CoMP	Coordinated Multi-point
COST	European Cooperation in Science and Technology
D2D	Device-to-device
dB	Power ratio in decibel scale
dBm	Power ratio in decibel scale with reference to one milliwatt (mW)
DOA	Direction-of-arrival

DOD	Direction-of-departure
DSS	Dynamic spectrum sharing
DTMKE	Double-truncated multiple Knife-edge
DUT	Device-under-test
DVB	Digital Video Broadcasting
EDGE	Enhanced Data Rates for GSM Evolution
EHF	Extra-high frequencies
EIRP	Effective Isotropic Radiated Power
eMBB	Enhanced mobile broadband
ER	Effective roughness
ETSI	European Telecommunications Standards Institute
FCC	Federal Communications Commission
FDMA	Frequency Division Multiple Access
FDTD	Finite-difference time-domain
FEM	Finite element method
FM	Frequency modulation
GHz	Gigahertz
GO	Geometric optics
GPRS	General Packet Radio System
GPS	Global Positioning System
GPU	Graphical processing unit
GSCM	Geometry-based stochastic channel model
GSM	Global System for Mobile Communication
GTD	Geometric theory of diffraction
HD	High-definition
HST	High speed train
IAB	Integrated Access Backhaul
ICN	Information-Centric Networking
IF	Intermediate frequency
i.i.d.	Independent and identically distributed
IP	Internet Protocol
IMT	International Mobile Telecommunications
InF	Indoor factory
InH	Indoor hotspot
InO	Indoor office
IoE	Internet of Everything
IoT	Internet of Things
IRS	Intelligent reflecting surface

ISI	Inter-symbol interference
ITU	International Telecommunication Union
ITU-R	ITU Radiocommunication Sector
KHz	Kilohertz
LNA	Low-noise amplifier
LO	Local oscillator
LOS	Line-of-sight
LTE	Long Term Evolution
MTC	Machine-type communications
MDF	Medium density fiber
MHz	Megahertz
MIMO	Multiple-input multiple-output
MISO	Multiple-input single-output
MR	Mixed reality
mMIMO	Massive MIMO
mmWave	Millimeter wave
MoM	Method of Moments
MS	Mobile station
MSE	Mean square error
MU	Multi-user
NGMN	Next Generation Mobile Networks
NLOS	Non line-of-sight
NMTS	Nordic Mobile Telephone System
NR	New Radio
NTN	Non-Terrestrial Networks
NTT	Nippon Telephone and Telegraph
OFC	Optical fiber cable
OFDM	Orthogonal frequency-division multiplexing
OLOS	Obstructed LOS
PAS	Power angular spectrum
PEC	Perfect electric conductor
PDC	Personal Digital Cellular
PDF	Probability distribution function
PDP	Power-delay profile
PN	Pseudo noise
QoS	Quality of service
RAN	Radio Access Network
RF	Radio frequency

RIS	Reconfigurable intelligent surface
RMa	Rural macrocellular
RMS	Root mean square
RX	Receiver
SDN	Software Defined Networks
SHF	Super-high frequencies
SIMO	Single-input multiple-output
SISO	Single-input single-output
SNR	Signal-to-noise ratio
TACS	Total Access Communication System
TDD	Time-division duplexing
TDL	Tapped delay line
TE	Transverse Electric
THz	Terahertz
TM	Transverse Magnetic
TSDSI	Telecommunications Standards Development Society
TTA	Telecommunications Technology Association
TTC	Telecommunications Technology Committee
TX	Transmitter
UE	User equipment
UHF	Ultra-high frequencies
uHSLLC	Ultra-high speed low-latency communications
ULA	Uniform linear array
UMa	Urban macrocellular
UMi	Urban microcellular
uMUB	Ubiquitous mobile ultra-broadband
URRLC	Ultra-reliable low-latency communication
US	Uncorrelated scattering
UTD	Uniform theory of diffraction
V2I	Vehicle-to-infrastructure
V2V	Vehicle-to-vehicle
V2X	Vehicle-to-everything
VHF	Very-high frequencies
VNA	Vector network analyzer
VPL	Vehicle Penetration Loss
WiMAX	Worldwide Interoperability for Microwave Access
WLAN	Wireless Local Area Network
WSS	Wide-sense stationary

List of Symbols

Greek

ϵ	Complex permittivity
ϵ_r	Relative permittivity
ϵ_0	Permittivity in free space
μ	Permeability
μ_r	Relative permeability
μ_0	Permeability in free space
η	Wave impedance
$\tan\delta$	Loss tangent
γ	Complex propagation constant
λ	Wavelength
θ_i	Angle of incidence
θ_r	Angle of reflection
θ_t	Angle of transmission
$\Gamma_\parallel$	Reflection coefficient for parallel polarization
$\Gamma_\perp$	Reflection coefficient for perpendicular polarization
$\Delta\tau$	Delay resolution
τ_rms	Root mean squared delay spread
τ_m	Mean delay
μ_Ω	Mean departure angle
ξ_σ	Shadowing gain
σ	Standard deviation
Ω_A	Direction-of-arrival
Ω_D	Direction-of-departure
ζ	Distortion error

Latin

A_{RX}	Receiver antenna aperture
B	System bandwidth
$\mathbf{B}$	Magnetic flux density
B_{c}	Coherence bandwidth
$\mathbf{D}$	Electric flux density
d_{TX}	Transmitter distance
d_{RX}	Receiver distance
$\mathbf{E}$	Electric field
E_{t}	Transmitted electric field
E_{r}	Reflected electric field
E_{s}	Scattered electric field
f_{c}	Carrier frequency
f_{Dmax}	Maximum Doppler frequency
G_{Tx}	Transmitter antenna gain
G_{Rx}	Receiver antenna gain
$\tilde{G}_{\mathrm{TX}}$	Complex transmitter radiation pattern
$\tilde{G}_{\mathrm{RX}}$	Complex receiver radiation pattern
$\tilde{g}_t$	Sounding signal
$\mathbf{H}$	Magnetic field
$h(\tau)$	Channel impulse response
$H(f)$	Channel transfer function
H_{ij}	Multiple-input multiple-output (MIMO) matrix
$\mathbf{J}$	Electric current
K	Small-scale fading K-factor
k	Wave number
l_{e}	Electrical length
L_{VPL}	Vehicle penetration loss
L_{r}	Pathloss
n	Refractive index
O	Origin in Cartesian coordinate system
$P(\tau)$	Power-delay profile
P_{TX}	Transmit power
P_{RX}	Receive power
P_{BF}	Beamforming power angle spectrum
P_{th}	Threshold power
P_{CF}	Crest factor
P_{n}	Noise power

$\mathbf{P_e}$	Dipole moment
$\mathscr{P}$	Poynting vector
$p(\tilde{\tau})$	Channel sounder impulse response
$\hat{R}$	Spatial covariance vector
R_{h}	Impulse response auto-correlation function
S_{F}	Area of Fresnel zone
S_{Ω}	Angle spread
T_{r}	Sounding signal duration
$T_{\parallel}$	Transmission coefficient for parallel polarization
$T_{\perp}$	Transmission coefficient for perpendicular polarization
T_{chirp}	Chirp duration
u_{p}	Group velocity
v_{max}	Receiver speed
w_{Fn}	Radius of nth Fresnel zone
$\mathrm{w_{BF}}$	Beamforming weights
X	Shadowing loss

Math operators

∇	Gradient
$E[.]$	Expectation
$\frac{d}{dx}$	Derivative with respect to variable x
$\frac{\partial}{\partial x}$	Partial derivative with respect to variable x
$\Re(.)$	Real part
$\sum$	Sum
$\int$	Integral
$\circledast$	Convolution

1. Introduction

Communication has always been pivotal throughout human history. It has evolved in tandem with human evolution, from basic audio and visual signaling to this era's advanced and sophisticated communication systems. Primitive wireless communication constituted subtle processes, such as sounds or smoke signals to convey messages. However, the most disruptive innovation in the area of wireless communications began with the revolutionary work of Maxwell and Hertz, who laid the foundation of electromagnetic wave transmission. Tesla later demonstrated the transfer of information through these waves, which could be conveniently referred to as the first wireless communication system. On the other hand, Marconi made the debut public exhibit of wireless communication by transmitting Morse-coded signals through radio waves over the English Channel in July 1899. Today, we can connect through our mobile phones in merely a few seconds, thanks to the astounding research and developments in the field of wireless communication. The telecommunication industry of this age is a global enterprise and continues to expand its horizons by enabling us with state-of-the-art technology. Fifth generation (5G) is the contemporary and innovative wireless technology in the limelight of today's telecommunication industry. Let us glance at the evolution of cellular technologies from First generation (1G) to 5G.

1.1 The 5G evolution: A journey from 1G to 5G

The exponential growth of wireless technology is coupled with the rapid advancement of system-on-chip, incredibly reshaping the Internet and other similar technologies. Still, it has enormous potential to develop further, especially when a vast frequency spectrum resource remains unexploited. The phenomenal evolution of wireless communication networks

spans several generations over the past four decades, ever since the first analog communications network emerged in the early 1980s. This exceptional progress in technology, handsets, coverage, services, regulations, and standards is inconceivable for such a short period in the history of the world. We observe a symmetric growth trend where a new generation of wireless networks and standards arrives approximately every ten years, as illustrated in Figure 1.1 along with the timeline. At the beginning of the new millennium, around the year 2002, mobile phone subscribers surpassed the fixed-line telephone subscribers globally [1], marking a new history in telecommunications with mobile technology as the dominant means of voice communication.

1.1.1 Pre-5G cellular networks

First generation (1G)

The 1G wireless networks were deployed in the 1980s, mainly aiming at voice services with a minimal data rate of up to 2.4 kbps. It quickly gained significant popularity, and different standard networks became active in the world, for example, Nordic Mobile Telephone System (NMTS) in the Nordic countries, Advanced Mobile Phone System (AMPS) in the USA, Total Access Communication System (TACS) in Europe, and Japanese TACS and TZ-801 to TZ-803 by Nippon Telephone and Telegraph (NTT) company in Japan. 1G wireless systems were capable of transmitting analog signals at either 400, 800 and 900 MHz carrier frequency with limited bandwidth of 30 kHz leading to several disadvantages, such as poor voice quality due to interference, large sized handsets, hand-off issues, low transmission efficiency and lack of security. Frequency Division Multiple Access (FDMA) and frequency modulation (FM) were adopted as multiple access and modulation schemes, respectively.

Second generation (2G)

The Second generation (2G) wireless systems were developed in the early 1990s to provide better voice quality and capacity by transitioning from analog to digital communication technology, employing modulation techniques, e.g., Time Division Multiple Access (TDMA) and Code Division Multiple Access (CDMA). The prominent frequency bands of operation were 900 and 1800 MHz. The maximum data rate for 2G was 9.6 kbit/sec with the signal bandwidth of 1.25 MHz for CDMA and 200 kHz for Global

System for Mobile Communication (GSM), enabling the Short Message Service (SMS) service. In 2G, the GSM was essentially the predominant technology worldwide; however, Digital AMPS (IS-54/136) and CMDAOne (IS-95) were the central systems in North America, while Personal Digital Cellular (PDC) was operated in Japan. Over the next several years, 2G continued to upgrade itself with new technologies, such as General Packet Radio Service (GPRS) and Enhanced Data Rates for GSM Evolution (EDGE).

Third generation (3G)

In collaboration with the cellular community worldwide, International Telecommunicaton Union (ITU) adopted Third generation (3G) set of standards, popularly referred to as International Mobile Telecommunication-2000 (IMT-2000), to meet the growing need for faster speeds, multimedia services, and global compatibility. The 3G standards were enacted towards the end of the year 2000 in an effort to consolidate existing incompatible mobile environments into a seamless global network. 3G wireless networks are still operational in many parts of the world, providing data transfer rates of $144\,\mathrm{kbit/sec}$ up to $2\,\mathrm{Mbit/sec}$ offering nominal-speed access to the Internet. It includes new services that were not supported by previous generation networks, including web browsing, video streaming, and navigational maps. To achieve inter-connectivity and services like international roaming, Third Generation Partnership Project (3GPP), a consortium comprising seven telecommunication standards development organizations (ARIB, ATIS, CCSA, ETSI, TSDSI, TTA, TTC) was established to specify technical standards for cellular telecommunication technologies and it continues the standardization efforts for latest technologies to this date. Altogether, the 3G technology was the first to unleash the potential of connectivity and mobility.

Fourth generation (4G)

The Fourth generation (4G) was the first broadband and Internet Protocol (IP)-based cellular network complying with the capabilities defined by ITU and International Mobile Telecommunications-Advanced (IMT-Advanced) Standards. It was introduced in 2009, with Worldwide Interoperability for Microwave Access (WiMAX) and Long Term Evolution (LTE) being the two core technologies. 4G is capable of providing high-speed data rates up to $100\,\mathrm{Mbit/sec}$ for LTE and $300\,\mathrm{Mbit/sec}$ for LTE-Advanced. It provides much better spectral efficiency than 3G. Furthermore, it reduces latency

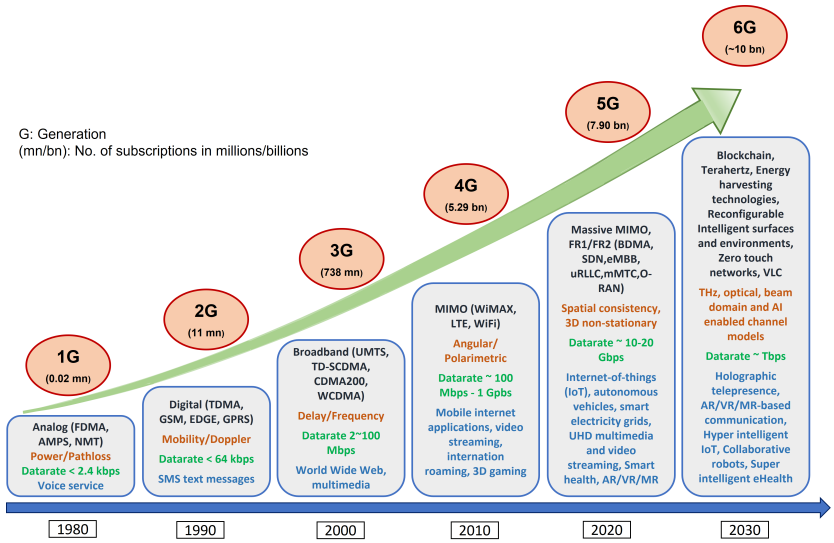

Figure 1.1. Evolution of wireless communication systems [1–6]

to accommodate the requirements set by advanced applications like Digital Video Broadcasting (DVB), high-definition (HD) mobile TV, and video conferencing. Furthermore, another outstanding feature enabled by 4G is device mobility across geographical boundaries through automatic roaming to provide smooth wireless services at any time and place. LTE successfully integrated existing and new technologies, such as multiple-input multiple-output (MIMO), and orthogonal frequency-division multiplexing (OFDM), and Coordinated Multi-Point transmission/reception (CoMP). Virtually, 4G technology relinquished the possibility of accessible information and social engagement through social media.

To sum up, wireless communication is pervasive, rendering billions (bns) of subscribers worldwide. In 4G networks, the subscribers skyrocketed, reaching 4.7 bn by the end of 2021 compared to the earlier projected number of 9 million (mn), and cellular traffic has increased 300 times within a decade, as explained in the latest mobility report by Ericsson [2, 3].

1.1.2 The 5G wireless technology

The Fifth generation (5G) wireless technology is expanding the mobile ecosystem to a completely new realm. 5G's unified and more capable air interface has been designed with an extended capacity to enable next-generation user experiences, empowering new deployment models and delivering new services. With the goal of achieving high speeds, superior reliability and low latency, wide-scale connectivity, and high energy effi-

ciency [7–10], 5G technology strives to create a deeper impact on various industries, ranging from transportation, remote healthcare, telesurgery, smart agricultural farms, digital and intelligent logistics, etc. It utilizes both sub-$6\,\mathrm{GHz}$ or centimeter wave (cmWave) (FR1) and above-$6\,\mathrm{GHz}$ millimeter wave (mmWave) (FR2) bands for the first time, enabling data rates up to $10\,\mathrm{Gbit/sec}$. For improving network performance, 5G is capable of integrating several emerging technologies, such as massive MIMO (mMIMO) for tremendous channel capacities, Software Defined Networks (SDN) for scalability in the network, device-to-device (D2D) for spectral efficiency, Information-Centric Networking (ICN) for efficient network traffic control and network slicing. 5G IMT-2020 [11] envisioned diverse 5G use cases under three main categories, including (1) Enhanced mobile broadband (eMBB) for new immersive user experience, (2) Ultra-reliable and low latency communications (URLLC) for patronizing sensitive services, such as remote controlling of critical infrastructure, and (3) massive machine-type communications (mMTC) to coherently connect a considerable number of embedded sensors providing lean connectivity. 5G technology essentially unlocked the capability of machines and sensing. As 5G is rolling towards commercial deployment, the research community has already started to brainstorm futuristic ideas for the next-generation of wireless networks, i.e., Sixth generation (6G), which is projected to be deployed around 2030.

The 5G telecommunication system is an unprecedented technology with cutting-edge transformation from its predecessors in terms of functional capabilities, such as low latency, astronomical data rates, high network reliability, enhanced security, massive connectivity, and avid spectrum and energy efficiency [7]. These features will massively benefit the Internet of Things (IoT), ultra-high speed connectivity, augmented and virtual reality (AR/VR), machine-type communication (MTC), autonomous vehicles, smart electric grids, etc. The initial deployment of 5G networks has already set a global footprint, and its success relies heavily on the continuing research and development (R&D) [9, 12], and standardization efforts [13–15]. The current focus of the telecommunication industry is on accelerating 5G across the communication ecosystem, making it a global commercial reality. In a broader perspective, 5G is not just about the consumer market, but there are also many other new growth opportunities, such as the enterprise sector where operators have started to launch 5G private networks supporting Industry 4.0 services. In a nutshell, there will be two leading 5G network segments, i.e., consumer market and business experience. From a

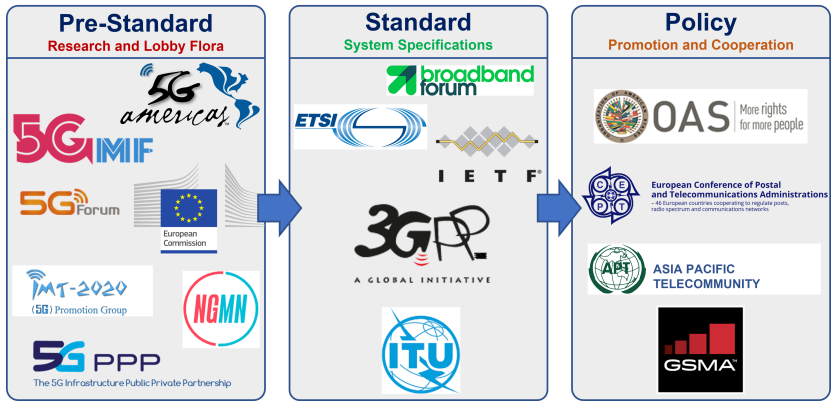

Figure 1.2. The brief landscape of 5G standardization.

network technology point-of-view, this means improving the system performance in terms of reliability, flexibility, and scalability based on endpoint market verticals. Security is another crucial aspect of this technology equation, especially when Information Technology (IT) and Operational Technology (OT) converge.

Standardization efforts

Standardization is critical for the mobile telecommunications industry. At its core, standardization is the process of researching, developing, and implementing technical standards based on the consensus of different parties that include influential 3GPP players, vendors, operators, and other interest groups. Standards enable differentiation and competition rather than homogenization. In essence, standardization maximizes technology compatibility, interoperability, security, repeatability, and quality. The 5G standardization is a complex and innovative process that involves countless stakeholders across diverse industries. The standardization of 5G started in 2016 and continues to this date.

For further elaborating the 5G standardization process, it can be conveniently divided into three main phases, i.e., (1) Pre-Standard, (2) Technical Specification, and (3) Policy. The standardization landscape of 5G is illustrated in Figure 1.2 [16], highlighting different stakeholders that have been involved in the three phases of the 5G standardization process.

The first phase encompasses the vision elaborated by the industry and other research stakeholders, mainly in terms of White Papers. In the recent past, several White Papers have been published by different associations and syndicates, such as 5G Americas [17], European Union [18], 5G Forum [19], 5GMF [20], NGMN [21], and many other platforms.

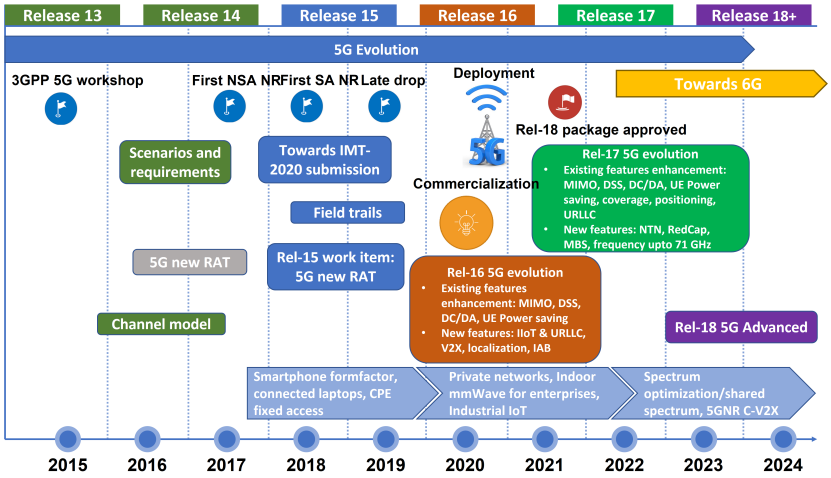

Figure 1.3. Tentative timeline for 5G releases.

The second phase deals with the technical standards and specifications, a collaboration of various standards development organizations, each working on a subset of the entire system. The final 5G standards will be endorsed by ITU-Radiocommunication Sector (ITU-R) [22] with 3GPP [13] playing the central role in specifying the complete 5G system and its related aspects, complying with ITU-R regulations.

The final segment of the standardization process represents the policy, cooperation, and regulation activities. These, for instance, include the regulations for 5G spectrum and interoperability for the broadloom delivery of 5G services.

The 3GPP Release-15 in June 2018 marks the first step towards the commercial deployment of 5G networks worldwide [23]. Ever since, there have been concerted efforts for the evolution of 5G technology following Release-16 and Release-17 for further enhancements and the inclusion of new use cases [24]. Recently, 3GPP has approved the work package for Release-18, which will be the framework for 5G-Advanced and a cornerstone for the next-generation wireless technology, i.e., 6G. Figure 1.3 shows the 3GPP's 5G evolution roadmap from 5G to 5G-Advanced.

Release-15

The most crucial specification in Release-15 was the new 5G air interface, popularly known as 5G New Radio (NR), for supporting features such as eMBB, URLLC, and mMTC. 5G NR allows both the non-standalone (NSA) operation that relies on Long Term Evolution (LTE) for initial access and mobility handling and the standalone (SA) operation without anchoring on

LTE. The salient features of 5G NR include high-frequency operation and spectrum flexibility, ultra-lean design, forward compatibility, low-latency support, and advanced antenna technologies, among others [25].

Release-16

The process of 5G evolution began with the Release-16, initiating significant enhancements for improving the existing features and introducing new use cases and deployment scenarios. The essential improvements are subjected to the existing features, such as MIMO, beamforming, dynamic spectrum sharing (DSS), reduced latency in dual connectivity and carrier aggregation (CA), and power saving for uuser equipment (UE). Release 16 also expanded the 5G NR to new verticals, such as industrial Internet of Things (IIoT) and URLLC, operation in unlicensed spectrum, vehicle-to-everything (V2X) communications, positioning services, and Integrated Access and Backhaul (IAB) [26, 27]. The ITU approved Release-15 and Release-16 submissions from 3GPP as IMT-2020 5G technology in the year 2020.

Release-17

As a continuation of 3GPP's 5G evolution, Release-17 focused on new use cases and deployment scenarios, such as Reduced Capability (RedCap) UE, extension of 5GNR operation to $71\,\mathrm{GHz}$, Multicast Broadcast Service (MBS), and Non-Terrestrial Networks (NTNs) for supporting satellite communication [26, 27].

Release-18

The work package on Release-18 triggers the work on 5G-Advanced. The scope of Release-18 was admitted to the 3GPP Radio Access Network (RAN) Release-18 workshop, which invited hundreds of proposals. After intensive deliberation, the 3GPP approved the Release-18 package in RAN plenary meeting on December 2021 [28]. This work package constitutes around 30 diverse study and work items.

1.1.3 6G: The next milestone

The Sixth generation (6G) wireless networks will supersede 5G technology in the future. Primarily, 6G technology is contemplated to provide enhanced performance and user experience than 5G, mainly through much higher data transmission up to $1\,\mathrm{Tbit/sec}$ and optimizing rate-reliability-latency tradeoffs. With 6G, the concept of communication networks will be

rattled with the intense proliferation of Internet of Everything (IoE) applications and services connecting billions of devices, involving multisensory extended reality (XR) as a combination of augmented, mixed, and virtual reality (AR/MR/VR), autonomous and flying vehicles, brain-computer interface systems, telemedicine, haptics, and blockchain distributed ledger technology [29]. Furthermore, energy harvesting technologies and advanced intelligent materials will enhance energy efficiency realizing more sustainable networks. 6G wireless systems features communication and spatial multiplexing at terahertz (THz) carrier frequencies, delivering 1000 times higher capacity than 5G networks. The 6G usage scenarios mainly fall into two main categories: (1) ubiquitous mobile ultra-broadband (uMUB) and (2) ultra-high speed low-latency communications (uHSLLC). Substantially, 6G technology will connect human and digital worlds by offloading mundane tasks from humans to machines and advanced features like holographic communication where one can teleport itself to a different environment. Further reading is encouraged to explore 6G vision through available papers and online resources [4–6, 30–38].

1.2 The radio propagation channel

The transmission medium, referred to as the Channel, is the core component of every communication system. In wireless communications, the transmission medium is the passband radio channel between the tansmitter (TX) and receiver (RX). While propagating from TX to RX through several propagation paths, the electromagnetic waves may interact with objects during their journey and hence undergo different physical phenomena. It is noteworthy that the propagation channel together with TX and RX antennas constitute a radio channel to form a radio link. Figure 1.4 depicts a typical radio wave propagation scenario.

The goal of an ideal wireless communication system is to achieve effective and reliable communication to provide the end user with the best possible and most satisfying experience. This could be realized only with a thorough understanding of the underlying radio propagation channel that imposes rudimentary limits on the performance of any wireless communication system. Only recently, the propagation channel was considered the only component of wireless communication systems that could not be architected. However, a new emerging paradigm is the concept of smart and reconfigurable radio environments with Intelligent Reflecting Surfaces

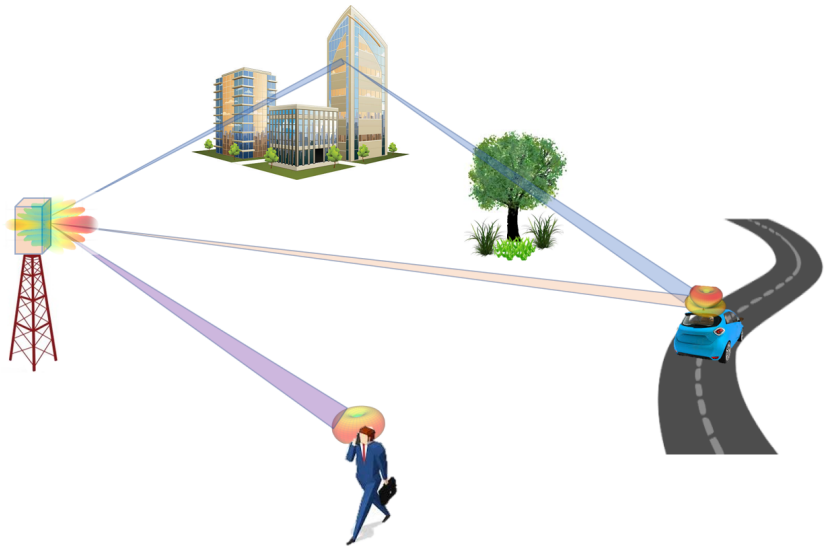

Figure 1.4. The radio propagation channel

(IRS) or Reconfigurable Intelligent Surfaces (RIS) as the promising and key enabling technology. RIS is a digitally-controlled metasurface with many low-cost passive reflecting surface elements that can induce a change in the amplitude and/or phase of the incident signals [39, 40]. RIS or other wireless system components, such as TX, RX, antennas, algorithms, protocols, etc., must be designed and built according to propagation channel constraints. Hence, this illuminates the very fact that adequate radio channel models are crucial for the wireless systems design and their operational deployment. Any realistic channel model is essentially a mathematical framework parameterized through an extensive set of measurements and retains the capability of reasonably reproducing the discrete effects of a radio channel. The scientific studies in this thesis revolve around the interaction of radio waves with physical objects of radio environments and the multipath characterization of radio channels; hence, these topics will be the main focus of the discussion hereafter. [4–6, 30–38, 41].

1.3 Channel modeling for 5G wireless systems

The design concept of 5G is driven by high data rate requirements to fuel its innovative features. (mmWave) is part of the frequency spectrum where large bandwidths are available, and hence, it is an intrinsic choice for achieving high data rates in 5G wireless communication systems. Similar to any radio system, the radio channel characteristics at mmWave bands

have a cardinal impact on communication system components and architecture in terms of design and performance. However, the radio channel characteristics at mmWave frequencies radically differ from those of the legacy sub-6 GHz frequency bands. This difference resides in the fact that propagation phenomena related to the interaction of radio waves with the propagation environment are frequency dependent [42–45].

1.3.1 Requirements and challenges

The advanced features of 5G and their technical prospects determine novel requirements for the channel modeling framework, which is necessary for the evaluation of 5G communication systems. Furthermore, assessing how these requirements differ from the existing channel models and what challenges are associated with them is vital. Some key 5G channel modeling requirements have been described thoroughly in [7, 46, 47] and are briefly summarized below.

1. **Frequency agility and large bandwidths:** To serve a variety of use cases and scenarios and meet high data rate requirements, 5G channel model is required to cover a wide range of carrier frequencies, such as 0.5–100 GHz, and ultra-wide bandwidths, such as 1–4 GHz. Although propagation phenomena behave differently across this broad frequency spectrum, the channel model should be consistent and applicable over all frequencies. It is demanding as it requires extensive channel model parameterization from theoretical and experimental viewpoints.

2. **Diverse scenarios:** The 5G channel model should also handle diverse scenarios, such as indoor, outdoor, indoor-to-outdoor, outdoor-to-indoor, rural, urban, suburban, industrial, high-speed train, and underground tunnels.

3. **3D double-directional modeling:** Unlike a radio channel, a propagation channel excludes the effect of TX and RX antennas and is described through a double-directional channel response. The angular spread information is known at TX and RX in a double-directional channel. This hefty attribute enables us to exploit the inherent basis of radio wave propagation, i.e., multipath components [48]. The 5G channel model is mandated to be double-directional with accurate modeling of antenna and propagation parameters in 3D.

4. **Spatial consistency:** Spatial consistency is paramount when we discuss the intricacy and quality of a channel model, and hence, is a core requirement for 5G channel model. It refers to the channel condition when TX or RX terminals in proximity observe similar channel behavior in terms of angle, delay, power, and polarization state. Thus, for a channel model to be classified as spatially consistent, its parameters must evolve smoothly and continuously over time of mobile user movement and hence their locations over space. Dual mobility scenarios, such as device-to-device (D2D) and vehicle-to-vehicle (V2V) communication, sustain unique challenges for satisfying spatial consistency in a channel model since temporal consistency must also be maintained simultaneously. The absence of spatial consistency in a channel model would result in inaccuracies in network performance evaluation for mMIMO and multi-user (MU) MIMO networks, especially for beamforming, beam tracking, and handovers in mobility scenarios [49].

5. **Massive antenna systems:** Higher frequencies are a prime candidate for 5G cellular systems, enabled by the deployment of massive antenna arrays with hundreds of antenna elements at the base station to surmount high pathloss through significant array gains and belligerent spatial multiplexing for increased sum-rate capacities. The fundamental physics behind this tremendous increase in channel capacity is the energy-focusing capability of antenna arrays with a large number of elements in the form of sharp, high gain *pencil* beams by the coherent superposition of wavefronts [50, 51]. It is noteworthy that when the array antennas are large with respect to the wavelength, electromagnetic waves emitting from radio sources or scatter from objects cannot be approximated as plane waves anymore because the distance between RX and TX (or scatterer) may become smaller than the Rayleigh or far-field distance characterized by $2\mathrm{D}^2/\lambda$, where D is the largest dimension of the antenna array and λ is the wavelength of the carrier frequency [52, 53]. Therefore, radiating waves need to be considered spherical waves, which may affect the beamforming techniques. Another crucial aspect to consider is the overall size of the array. When it becomes enormous, it reduces the channel hardening and spatial diversity gain due to variation in the strength of multipath over the array [7, 54]. The small-scale fading decreases in the channel hardening effect, and the channel

becomes deterministic. Furthermore, with the limitations on the form factor of large-scale arrays, the mMIMO arrays will most likely be 3D planar, or cylindrical arrays with profound angle spread in the elevation plane, which must be considered in the 5G spatial channel model.

6. **High mobility:** The advancement in the field of urban transportation introduces new use cases for 5G cellular networks, such as high-speed train (HST) scenario where the speed of the train could exceed $500\,\mathrm{km\,h^{-1}}$. The 5G channel model should be capable of reproducing the high Doppler spectrum with reasonable accuracy. Moreover, the channel model must reliably evaluate channel conditions in various HST scenario settings, including open outdoors, mountainous terrain, underground tunnel, and station.

7. **Computational complexity:** For 5G channel model to be tractable, it must be concise and descriptive to ensure unambiguous and clear implementation. Furthermore, the functional model implementation should not be too complex to require heavy computational resources.

1.3.2 Target channel models

After many development stages in 3GPP and ITU-R, 5G channel model standards were proposed in [15, 55, 56] and continue to evolve. These standards are valid for wide frequency ranges and large bandwidths, featuring the modeling of pathloss, blockage, penetration loss, atmospheric absorption losses, and spatial consistency. Traditionally, the 3GPP and ITU-R channel models assumed constant propagation channel parameters as the user moves along a path confined by the stationarity distance of the parameters. This, along with the resulting channel description, holds according to the special Bello conditions [57]. Some key aspects of 5G channel models are briefly described below, and a more thorough historical perspective on the evolution of standardized models towards 5G is available in [41].

Pathloss models

The cooperation between multiple industrial and academic organizations [58] to propose a 5G channel model for frequencies up to $100\,\mathrm{GHz}$ involved extensive radio channel measurement campaigns. As a result of this joint effort, pathloss models for 3GPP/ITU-R were proposed and presented in [15, 56]. The pathloss model parameters in [56] follow a similar pattern

as legacy standard pathloss models but are frequency dependent. There are four categories of pathloss models based on radio environments described in [56] for 5G, both in Line-of-sight (LOS) and Non line-of-sight (NLOS) conditions. These include, rural macrocellular (RMa), urban macrocellular (UMa), urban microcellular (UMi), indoor hotspot (InH), and indoor factory (InF).

Directionally resolved models

The channel models proposed in 3GPP and ITU-R are directionally-resolved models and follow the principle framework of *Geometry-based stochastic channel model* (GSCM). In GSCM, the location of scatterers is determined by a random probability distribution, unlike deterministic raytracing models, which describe scatterers' locations in a three-dimensional (3D) geometry of a given radio environment. These models follow many fundamental concepts introduced in European Cooperation in Science and Technology (COST) channel models [59–62]. The distinction between the COST and 3GPP/ITU-R model relates to the fact that COST models are complex for system-level simulations and their discretized versions for standards are unavailable. From the implementation perspective, the 3GPP and ITU-R models deal with the angular dispersion as an extension of the tapped delay line (TDL) model to the angular characteristics [41]. For 5G NR, [56] prescribes a systematic procedure for generating correlation in propagation parameters over frequencies.

Blockage models

The shadowing effect at mmWave frequencies is more evident as compared to cmWave frequencies since diffraction is less significant. Other than the shadowing, i.e., large fluctuations in the received power caused by the trajectory of the moving user, the auxiliary shadowing effect, i.e., blockage, due to the blocking of multipath by humans or objects in the radio environment is also considered by the standardized 5G models. The self-shadowing is categorized under the same blockage models, which depends on the device's orientation with respect to the user's holding position. Two blockage models are included by 3GPP and ITU-R, namely Model A and Model B [15, 56]. Model A is applied to human and vehicular blockage scenarios, which modifies the small-scale fading cluster parameters through an iterative step-by-step method. Blockage region parameters are defined for RMa, UMa, UMi, InH, and InF scenarios. Model B implements a geometrical modeling methodology in both LOS and NLOS propagation

conditions. Table 7.6.4.2–5 in [56] presents the parameters of Model B, including the number, size, and mobility of the blockers and the projected distances between the receiver and blocker edges.

LOS probability models

The LOS probability refers to the chance that a mobile station (MS) undergo LOS propagation conditions with the base station (BS) and the LOS component has zero angular spread. The standard models in [15, 56] determine the LOS condition by analyzing whether the LOS path between the BS and MS is interrupted or not. The effect of scattering environments, such as buildings, cars, lampposts, and other interacting objects, is not included and modeled separately. Due to this, the LOS probability is not a function of the carrier frequency. The standardized LOS probability model in [56] are defined for RMa, UMa, UMi, indoor office (InO), and InF scenarios.

Spatial consistent models

Spatial consistency is mandated by 3GPP for 5G NR channel models. The legacy 3GPP and ITU-R channel models are devoid of spatial consistency and employ the concept of *drop*, which is regarded as the instantaneous channel segment according to the standardization nomenclature. For a given *drop*, the small-scale and large-scale parameters follow specific statistical distributions in order to generate the consolidated channel impulse response. However, the channel parameters are not continuous between the *drops*. In practice, the continuity of propagation parameters is highly favorable across multiple channel realizations, especially when the channel is dynamic. Furthermore, the system-level performance analysis for the beam tracking algorithms in Release-16 and Release-17 [45, 63] 3GPP emphasizes the need for spatially consistent channel models. For spatially consistent channel modeling, the 3GPP and ITU-R specify two procedures in [15, 56], called Model A and Model B. Model A involves an iterative algorithm for updating propagation parameters but is restricted to a limited user movement defined according to the correlation distance of the parameters. In Model B, the propagation parameters are independently obtained for each user location, thereby generating cluster delay and angles with a modified procedure.

Map-based hybrid models

The site-specific map-based hybrid channel models are essentially a combination of deterministic raytracing and stochastic channel modeling approach that utilizes a 3D geometry of the radio environment where buildings and other relevant structures are assigned with accurate material properties. The link geometries are configured with antennas, and clusters are placed deterministically. The directionally resolved channel impulse resolved is then generated following the 3GPP GSCM recipe. The 3GPP describes map-based models in [56] as an alternative channel modeling approach for accurate system-level analysis of 5G systems.

1.4 Scope and objectives of the thesis

For developing state-of-the-art radio channel models to suit different 5G applications, it is imperative to have an all-inclusive knowledge of radio channels at the desired frequency spectrum. The timeline of the research studies undertaken in this thesis is aligned with the standardization activities for 5G, which highlights their significance, timeliness, and potential scientific impact. Predominantly, this thesis focuses on modeling the interaction of radio waves with surrounding objects in the environment and multipath characterization of radio channels at cmWave and mmWave frequencies. Thus, the scope of the thesis is set on the premise of investigating following questions, defining the overall perimeter in which the research was carried out.

Question 1*: How do different interacting objects in built environments affect wave propagation at radio frequencies?* The objects in a radio environment influence the propagation of mmWave signals at different levels depending on their material properties. Specifically, the scientific community is deeply interested in understanding the interaction of mmWave signals with material objects and quantifying it in terms of propagation losses, such as transmissions and reflections, so that these can be accounted for in the modeling phase.

Question 2*: What is the impact of human blockage on mmWave radio signals?* Humans are the main beneficiary of advanced and ubiquitous wireless systems around them. The dense population of humans in urban areas and their size becoming much larger than the wavelength at mmWave frequencies make the signals more susceptible to blockage effects causing temporal variations in radio channels. Therefore, it is deemed nec-

essary to characterize and model human blockage at mmWave frequencies to facilitate the design of 5G wireless systems.

Question 3*: Can we make efficient use of full-wave numerical techniques for radio coverage predictions?* The most accurate solution of the electromagnetic Maxwell equation is available in the form of full-wave numerical methods. Since radio coverage analysis is momentous for planning and deploying wireless networks, it is an exciting endeavor to evaluate the feasibility of full-wave numerical methods for this purpose.

Question 4*: How different are the radio channels at cmWave and mmWave frequencies? Can we identify some unique characteristics that may aid the design of 5G wireless systems?* 5G wireless systems aim to operate at both cmWave and mmWave frequency bands, which require the evaluation of essential differences in power, delay, and spatial domains between cmWave and mmWave radio channels for different propagation settings.

To invigorate the research questions illuminated above, the main objectives of the thesis are:

1. Characterize and model the interaction of radio waves with humans and objects within radio environments in terms of reflection, transmission, and blockage losses at cmWave and mmWave frequencies.

2. Estimate permittivity of composite materials at mmWave frequencies for aiding coverage predictions.

3. Determine the feasibility of full-wave numerical methods, such as finite-differece time-domain (FDTD) method for radio wave coverage analysis.

4. Characterize indoor and outdoor multipath radio environments at cmWave and mmWave frequencies for small and large-scale multipath fading and angular selectivity.

1.5 Research methodology of the thesis

This thesis follows a quantitative research methodology where the data is gathered either through radio channel measurements or numerical simulations. The collected data is then subjected to statistical analysis, and results are demonstrated in a tabulated or graphical format to provide meaningful interpretation. Briefly,

(a). A thorough literature review is conducted on each research topic to accentuate the problem statement and highlight the novelty of the work.

(b). The experiments involved radio channel sounders developed at Aalto University, Finland, and the University of Southern California, USA.

(c). Simulations, data processing, and data analysis is carried out using MATLAB software.

(d). Some studies also involved measurements in a specialized anechoic chamber at Aalto University.

(e). The feasibility of full-wave numerical methods for coverage predictions is evaluated using a commercially available FDTD software, SEMCAD-X, which was supported with graphical processing unit (GPU) acceleration.

1.6 Scientific contributions of the thesis

This thesis constitutes the summary of eight publications and the main scientific contribution for each of these is briefly described below.

[I] Characterizes Vehicle Penetration Loss (VPL) at sub-6 GHz frequencies employing commercially available window films. The study concludes that metalized automotive window films typically employed for infrared (IR) and ultraviolet (UV) light rejection may deteriorate radio signals up to $20\,\mathrm{dB}$, significantly affecting cellular communication into vehicles.

[II] Presents a novel method for modeling specular reflections in a 3D point cloud geometrical description of a given radio environment using the Fresnel reflection zone concept, thereby improving the accuracy of point cloud raytracing simulations for radio coverage.

[III] Evaluates transmission and reflection losses experienced by typical interacting objects in radio environments for $70\,\mathrm{GHz}$ mmWave signals. Based on the estimated results, it is inferred that particular objects, such as specialized windows, laminated plywood, plasterboard, etc., are good reflectors of mmWave signals and could help maintain good signal strength in NLOS. On the other hand, in transmission mode,

humans and specialized building windows attenuate signals at this frequency band as high as 40dB, causing intermittent link outages.

[IV] Introduces a novel approach for estimating the permittivity of materials in a built environment with the aid of accurate geometrical description and limited channel measurements of the radio environment. The estimated results are visualized as a colored 3D permittivity point cloud map, consistent with the values available in ITU-R recommendation. The proposed method is efficient, essentially reducing the need for isolated RF measurements for characterizing composite materials in a radio environment.

[V] Reports human blockage losses for 15 human subjects with different weights and sizes through anechoic chamber measurements at 15, 28, and 60 GHz frequency bands. Furthermore, a novel double-truncated multiple Knife-edge (DTMKE) model is proposed, which adequately predicts the measured human blockage loss for different body orientations and radiating antenna heights.

[VI] Demonstrates the feasibility of full-wave FDTD electromagnetic method for radio coverage predictions in an indoor environment. The simulations are validated against the measurements of the same radio environment. The results suggest that numerical methods require high computational effort and that there is a trade-off between the accuracy and complexity of the simulation.

[VII] Delineate comprehensive radio channel measurements in an indoor coffee room at cmWave (2 GHz) and mmWave (15, 28, and 60 GHz) frequency bands and compare power angular spectrum (PAS) of these radio channels to study and understand frequency dependency and spatial consistency of multipath in the angular domain. The results explain that the spatial spread of multipath LOS conditions is similar across cmWave and mmWave radio channels. On the other hand, the cmWave radio channels offer more spatial spread of multipath in NLOS conditions than mmWave radio channels.

[VIII] Describes radio channel measurements performed in an outdoor plaza environment at cmWave (2 GHz) and mmWave (60 GHz) frequencies. The results indicate that the large-scale fluctuations in the signal envelope of mmWave channels are more extensive than those observed

in cmWave channels. Furthermore, the mmWave channels exhibit less delay dispersion as compared to cmWave channels.

1.7 Organization of the thesis

This thesis is produced in an article-type format with a concise summary of eight scientific publications in the field of radio channel characterization for 5G wireless systems. The summary also outlines the key concepts associated with the subject of the thesis and study topics of the publications. It further describes the scientific problems addressed through the publications and consists of four chapters. Chapter 1 delivers the opening of the thesis with a brief description of 5G evolution and related channel modeling requirements, objectives and scope of the thesis, main scientific contributions of the thesis, and finally, the organization of the thesis. Chapter 2 focuses on the interaction of radio waves with physical objects in a radio environment by first articulating the fundamentals of radio wave propagation and then construing the contribution of the thesis on this subject covering publications [I] to [V]. Chapter 3 discusses the multipath characterization of radio channels from both narrowband and wideband perspectives. It also describes common radio channel sounding techniques, including those that were exploited for radio channel measurements intended for this thesis. Furthermore, different radio channel modeling approaches are introduced, followed by a brief discourse on the contributions of the thesis based on publications [VI] to [VIII]. Chapter 4 presents a brief summary of each of the publications included in the thesis. Finally, Chapter 5 concludes the thesis with a comprehensive synopsis of the research undertaken and presents key takeaway messages.

2. Modeling the Interaction of Radio Waves with Material Objects

The wireless communication systems surrounding us rely on the physics of electromagnetic wave propagation in free space and their interaction with different material objects often termed as *scatterers* in literature. This chapter presents a theoretical perspective of radio wave propagation and its associated mechanism. Further, it describes the thesis's contribution to modeling the interaction of radio waves with material objects.

2.1 Fundamentals of radio wave propagation

Maxwell equations provide a relationship between electric ($\mathbf{E}$) field, magnetic field ($\mathbf{H}$) and their sources, i.e., electric current and charge densities $\mathbf{J}$ and ρ, respectively. From hereafter, the vector quantities will be represented with boldfaced letters. The time-harmonic differential form of Maxwell equations are [64]

$$\nabla \cdot \mathbf{D} = \boldsymbol{\rho}, \tag{2.1}$$

$$\nabla \cdot \mathbf{B} = 0, \tag{2.2}$$

$$\nabla \times \mathbf{E} = -j\omega\mathbf{B}, \tag{2.3}$$

$$\nabla \times \mathbf{H} = \mathbf{J} + j\omega\mathbf{D}. \tag{2.4}$$

The effect of the medium is taken into account by the electric flux density $\mathbf{D}$ and the magnetic flux density $\mathbf{B}$. The Maxwell equations amicably confirm the existence of electromagnetic waves capable of transporting power from one point to another in a propagation medium. The field strengths and flux densities are constrained by the media in which electromagnetic waves are propagating; hence, the constitutive relations that describe the correlation between $\mathbf{D}$ and $\mathbf{E}$ and between $\mathbf{B}$ and $\mathbf{H}$ necessary to solve the Maxwell

equations are

$$\mathbf{D} = \epsilon \mathbf{E}, \tag{2.5}$$

$$\mathbf{B} = \mu \mathbf{H}. \tag{2.6}$$

Hence, (2.3) and (2.4) can be further elaborated as

$$\nabla \times \mathbf{E} = -j\omega\mu\mathbf{H}, \tag{2.7}$$

$$\nabla \times \mathbf{H} = (\sigma + j\omega\epsilon)\mathbf{E}, \tag{2.8}$$

where $J = \sigma\mathbf{E}$ is the current charge density, ϵ is the permittivity (Farad/meter = F/m), μ is the permeability (Henry/meter = H/m) and σ is the conductivity of the medium (Siemens/meter = S/m).

Material properties

Classifying a material medium into different types is possible based on how its properties vary with field strength, location, and direction. If the properties of a medium are constant and independent of location, it is known as a homogeneous medium. A medium is isotropic if its properties are the same in all directions. On the other hand, a medium exhibiting different properties in all directions is called an anisotropic medium. The properties of linear media are independent of the field strength. In vacuum, $\epsilon = \epsilon_0 \approx 8.8542 \times 10^{12}$ F/m and $\mu = \mu_0 = 4\pi \times 10^{-7}$ H/m. In other homogeneous media, $\epsilon = \epsilon_{\mathrm{r}}\epsilon_0$ and $\mu = \mu_{\mathrm{r}}\mu_0$, where relative permittivity ϵ_{r} and relative permeability μ_{r} depend on the structure of the material. For air, we can assume $\epsilon_{\mathrm{r}} = \mu_{\mathrm{r}} = 1$ for most radio engineering applications. Generally, in lossy media, ϵ_{r} or μ_{r} are complex quantities, while in anisotropic medium, these are tensors.

To further elaborate the effect of propagation medium, let's expand expression (2.5) as

$$\mathbf{D} = \epsilon_0 \mathbf{E} + \mathbf{P_e}, \tag{2.9}$$

where ϵ_0 refers to the permittivity of vacuum and $\mathbf{P_e}$ is the dipole moment per unit polarization. In a linear medium, the electric field polarization depends linearly on the field strength as

$$\mathbf{P_e} = \epsilon_0 \chi_e \mathbf{E}, \tag{2.10}$$

where χ_e refers to the electric susceptibility and can be a complex quantity. Now combining (2.9) and (2.10), we obtain

$$\mathbf{D} = \epsilon_0(1 + \chi_e)\mathbf{E} = \epsilon\mathbf{E}, \tag{2.11}$$

where

$$\epsilon = \epsilon_0(1 + \chi_e) = \epsilon_0\epsilon_r = \epsilon_0(\epsilon_r^{'} - j\epsilon_r^{''}) \tag{2.12}$$

is the complex permittivity whose imaginary part represents the Ohmic loss in the medium. Both $\epsilon_r^{'}$ and $\epsilon_r^{''}$ can be functions of frequency.

Referring to equation (2.4) and introducing electric current density $\mathbf{J} = \sigma\mathbf{E}$, we have

$$\nabla \times \mathbf{H} = j\omega\left(\epsilon + \frac{\sigma}{j\omega}\right)\mathbf{E} = j\omega\epsilon_0\left(\epsilon_{\mathrm{r}}^{'} - j\epsilon_{\mathrm{r}}^{''} - j\frac{\sigma}{\omega\epsilon_0}\right)\mathbf{E}. \tag{2.13}$$

Ohmic loss of a medium is typically characterized by its loss tangent

$$\tan\delta = \frac{\sigma}{\omega\epsilon} = \frac{\epsilon_{\mathrm{r}}^{''} + \sigma/(\omega\epsilon_0)}{\epsilon_{\mathrm{r}}^{'}} \approxeq \frac{\epsilon^{''}}{\epsilon^{'}}, \tag{2.14}$$

where δ is also sometimes referred as loss angle. Using (2.14) reduces the expression in (2.13) to

$$\nabla \times \mathbf{H} = j\omega\epsilon_0\epsilon_{\mathrm{r}}^{'}(1 - j\tan\delta)\mathbf{E}. \tag{2.15}$$

A similar argument holds for the magnetic field component. The magnetic dipole moments are aligned by the magnetic field, polarizing the material magnetically. The complex permeability μ can be split into a real part $\mu_{\mathrm{r}}^{'}$ and an imaginary part $\mu_{\mathrm{r}}^{''}$ that causes magnetic loss.

$$\mu = \mu_0(\mu_{\mathrm{r}}^{'} - j\mu_{\mathrm{r}}^{''}) \tag{2.16}$$

From (2.13), we can deduce that a material medium is a good insulator if $\omega\epsilon \gg \sigma$ and a good conductor if $\omega\epsilon \ll \sigma$. Hence, a material medium may exhibit good conductivity at low frequencies but may be a lossy dielectric at very high frequencies.

Plane wave: A solution of Helmholtz equation

A uniform plane wave is a unique solution of Maxwell's equations where **E** and **H** field have the same magnitude, direction and phase along infinite planes, perpendicular to each other and the direction of propagation. A uniform plane wave does not exist in reality since it would require an

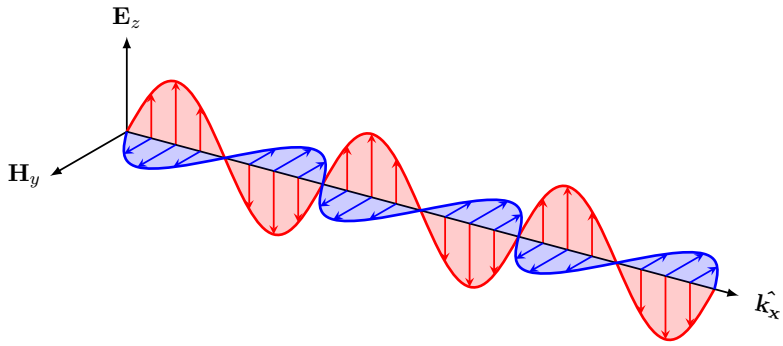

Figure 2.1. A plane wave propagating $+x$ direction.

infinite source to generate it. However, with a far-field assumption of a point source, a small differential element of a spherical wavefront can be approximated as a plane. For practical purposes, the plane wave solution of Maxwell's equation becomes a foundation of advanced electromagnetic wave propagation concepts. In a Cartesian coordinate system, a plane wave propagating in $+x$ direction is illustrated in Figure 2.1, with its $\mathbf{E}$ and $\mathbf{H}$ field components perpendicular to each other and direction of propagation.

A nonconducting source-free medium is defined by $\rho = 0$, $\mathbf{J} = 0$, and $\sigma = 0$, thus, the Maxwell's equations in (2.1) to (2.4) become

$$\nabla \cdot \mathbf{E} = 0, \tag{2.17}$$

$$\nabla \cdot \mathbf{H} = 0, \tag{2.18}$$

$$\nabla \times \mathbf{E} = -j\omega\mu\mathbf{H}, \tag{2.19}$$

$$\nabla \times \mathbf{H} = j\omega\epsilon\mathbf{E}. \tag{2.20}$$

Combining (2.17) to (2.20) yields second order partial differential equations in $\mathbf{E}$ and $\mathbf{H}$, famously known as homogeneous Helmholtz's wave equation

$$\nabla^2\mathbf{E} + k^2\mathbf{E} = 0, \tag{2.21}$$

and

$$\nabla^2\mathbf{H} + k^2\mathbf{H} = 0, \tag{2.22}$$

where $k = \omega\sqrt{\mu\epsilon}$ is the wavenumber $[1/\mathrm{m}]$.

Let us first assume the electromagnetic wave propagation in a lossless

medium, where ϵ_{r}, μ_{r}, and k are real quantities. In a Cartesian coordinate system, (2.21) is equivalent to

$$\left(\frac{\partial^2}{\partial x^2}+\frac{\partial^2}{\partial y^2}+\frac{\partial^2}{\partial z^2}+k^2\right)\mathbf{E}=0. \tag{2.23}$$

A plane wave defined by its uniform E_z component having constant magnitude and phase over planes perpendicular to the direction of propagation x, i.e., $\partial^2 E_y/\partial y^2 = 0$ and $\partial^2 E_z/\partial z^2 = 0$, the expression in (2.23) simplifies to an ordinary partial differential equation as

$$\left(\frac{\partial^2}{\partial x^2}+k^2\right)E_z=0, \tag{2.24}$$

The solution of (2.24) can be seen as

$$E_z(x)=E_0^+e^{-jkx}+E_0^-e^{jkx}, \tag{2.25}$$

where E_0^+ and E_0^- are arbitrary complex constants and their values are determined by the source and boundary conditions. The time-harmonic representation of (2.25) is given as

$$\Re\left\{E_z(x)e^{j\omega t}\right\}=E_0^+\cos(\omega t-kx)+E_0^-\cos(\omega t+kx), \tag{2.26}$$

where first and second terms of (2.26) refer to the waves traveling in $+x$ and $-x$ direction, respectively. For a given point on the propagating wave, the phase is constant. Setting $\cos(\omega t - kx) = \text{constant}$ and taking its differential results in

$$u_{\mathrm{p}}=\frac{dz}{dt}=\frac{\omega}{k}=\frac{1}{\sqrt{\mu\epsilon}}=c\ (3\times10^8\ \mathrm{m/s}). \tag{2.27}$$

which refers to the phase velocity, i.e., the velocity of propagation of an equiphase front and is equivalent to the speed of light in free space.

Similar to the solution for **E** in (2.25), the associated magnetic field component perpendicular to the electric field and propagation direction of the plane wave can be evaluated as

$$H_y(x)=\frac{1}{\eta}(E_0^+e^{-jkx}-E_0^-e^{jkx}), \tag{2.28}$$

The ratio of **E** and **H** introduces a new quantity known as the intrinsic impedance of free space or simply, the wave impedance $\eta = \sqrt{\mu/\epsilon}$. For vacuum, it is $\eta_0 = \sqrt{\mu_0/\epsilon_0} \approx 120\pi\Omega \approx 377\Omega$.

Now considering plane wave propagation in a source-free lossy medium,

referring to (2.7) and (2.8), the solution of Helmholtz's equation is

$$\nabla^2 \mathbf{H} + \omega^2 \mu\epsilon \left(1 - j\frac{\sigma}{\omega\epsilon}\right) \mathbf{E} = 0, \tag{2.29}$$

where jk is substituted by γ, the complex *propagation constant*, such that

$$\gamma = \alpha + j\beta = j\omega\sqrt{\mu\epsilon}\left(1 - j\frac{\sigma}{j\omega\epsilon}\right)^{1/2} \tag{2.30}$$

where α and β are the real and imaginary parts representing *attenuation* and *phase constant*, respectively. Now for a plane wave propagating in $+x$ direction, Helmholtz's wave equation takes the form,

$$\left(\frac{\partial^2}{\partial x^2} + \gamma^2\right) E_z = 0, \tag{2.31}$$

which can be solved as

$$E_z(x) = E_0^+ e^{-\gamma x} + E_0^- e^{\gamma x}, \tag{2.32}$$

and its time-harmonic state is

$$\Re\left\{E_z(x) e^{j\omega t}\right\} = E_0^+ e^{-\alpha x}\cos(\omega t - \beta x) + E_0^- e^{\alpha x}\cos(\omega t + \beta x). \tag{2.33}$$

Good dielectric materials have non-zero conductivity, such that, $\epsilon^{''} \ll \epsilon^{'}$ or $\sigma/\omega\epsilon \ll 1$, under which the propagation constant γ can be approximated using binomial expansion as

$$\gamma = \alpha + j\beta \approxeq j\omega\sqrt{\mu\epsilon^{'}}\left[1 - j\frac{\epsilon^{''}}{2\epsilon^{'}} + \frac{1}{8}\left(\frac{\epsilon^{''}}{\epsilon^{'}}\right)^2\right], \tag{2.34}$$

where $\alpha \approxeq \omega\epsilon^{''}\sqrt{\mu/4\epsilon^{'}}\,\mathrm{Np/m}$ and $\beta \approxeq \omega\sqrt{\mu\epsilon^{'}}(1 + 0.125(\epsilon^{''}/\epsilon^{'})^2)\,\mathrm{rad/m}$.

A material is considered a good conductor when $\sigma/\omega\epsilon \gg 1$, the propagation constant can be approximated as

$$\gamma \approxeq \alpha + j\beta = j\omega\sqrt{\mu\epsilon}\sqrt{\frac{\sigma}{j\omega\epsilon}} = (1+j)\sqrt{\mu\omega\sigma/2}. \tag{2.35}$$

The factor $\delta_\mathrm{s} = 1/\alpha = (2/\mu\omega\sigma)^{1/2}$ is the distance through which the magnitude of propagating electromagnetic wave attenuates by a factor of e^{-1} or 0.368. This attenuation distance is also commonly referred to as *skin depth* or *depth of penetration*.

The orientation of $\mathbf{E}$ in space determines the *polarization* of a propagating plane wave, which may be fixed on a specific plane (*linear*) or vary with

time (*circular* or *elliptical*) polarization.

When a wave propagates through contiguous media with different constituent properties, it is necessary to define boundary conditions that must be satisfied by $\mathbf{E}$, $\mathbf{H}$, $\mathbf{B}$ and $\mathbf{D}$ fields [64, 65].

The quantity that describes the flow of electromagnetic power per unit area is called *Poynting* vector, which is essentially the power density vector of the electromagnetic field,

$$\mathscr{P} = \mathbf{E} \times \mathbf{H} \ (\mathrm{W/m^2}). \tag{2.36}$$

2.2 Propagation mechanisms

A radio wave transmitted from a TX antenna while propagating in an environment may undergo different propagation mechanisms before finally arriving at the RX antenna. It may follow a direct path between TX and RX through free space or interacts with a material object of the environment through physical phenomena, such as reflection, transmission, diffraction, and scattering. The factors that determine the type of propagation effect experienced by a propagating wave may include the electrical properties of the propagation medium and interacting objects, carrier frequency, and orientation of the impinging wave. This section briefly discusses the main propagation effects as follows.

2.2.1 Free space propagation

In Section 2.1, we have discussed the propagation of electromagnetic plane waves in bounded and unbounded media from a theoretical perspective in light of Maxwell's equations. Here, we consider the radio wave propagation with a more practical notion, i.e., electromagnetic energy emanating from the TX antenna, propagates in free space, and is received at the RX antenna, thus formulating a relationship of received power as a function of distance.

The law of energy conservation tells us that the integral of power density on a closed spherical surface around the TX antenna is equal to the power transmitted by it. Assuming TX at the center of the sphere with a radius r and radiating isotropically, the power density on the surface of the sphere is $P_{\mathrm{TX}}/4\pi r^2$ $(\mathrm{W/m^2})$, which is also referred to as the *inverse square law*. Now, the received power at the RX antenna with an effective aperture area

$A_{\mathrm{RX}}\,(\mathrm{m}^2)$, collecting all the incident energy, is

$$P_{\mathrm{RX}}(r) = \frac{P_{\mathrm{TX}}}{4\pi r^2} A_{\mathrm{RX}}. \tag{2.37}$$

A real antenna has some gain associated with it, i.e., how much power density it can radiate in the desired direction compared to an isotropic antenna. If G_{TX} is the gain of the TX antenna, equation (2.37) becomes

$$P_{\mathrm{RX}}(r) = \frac{P_{\mathrm{TX}} G_{\mathrm{TX}}}{4\pi r^2} A_{\mathrm{RX}}, \tag{2.38}$$

where the product $P_{\mathrm{TX}} G_{\mathrm{TX}}$ is commonly known as Effective Isotropic Radiated Power (EIRP). The relationship between A_{RX} and gain of RX antenna G_{RX} as a function of wavelength $\lambda\,(\mathrm{m})$ can be elaborated through the following expression

$$A_{\mathrm{RX}} = \frac{\lambda^2}{4\pi} G_{\mathrm{RX}}, \tag{2.39}$$

which when substituted in (2.38) gives

$$P_{\mathrm{RX}}(r) = P_{\mathrm{TX}} G_{\mathrm{TX}} G_{\mathrm{RX}} \left(\frac{\lambda}{4\pi r}\right)^2. \tag{2.40}$$

The expression (2.40) is famously known as the *Friis' equation*, indicating the attenuation of energy as it propagates away in free space with certain frequency and increasing distance. It is also important to note that *Friis' equation* is limited to the *far-field* region of the antenna. The antenna space can be categorized into three distinct regions depending on the properties of the radiated field, i.e., *reactive near-field*, *radiating near-field or Fresnel*, and *far-field or Fraunhofer* regions. In the *far-field* region, the normalized radiation pattern of the antenna becomes independent of the distance. The demarcation between *radiating near-field* and *far-field* region is given by the Rayleigh distance $r_{\mathrm{R}} = 2D_{\mathrm{a}}^2/\lambda$, where D_{a}^2 is the largest dimension of the antenna. Also, the far-field assumption dictates that $r \gg \lambda$ and $r \gg D_{\mathrm{a}}^2$.

2.2.2 Reflection and transmission

A homogeneous electromagnetic plane wave incident at the surface of an interacting object may get partly reflected and partly transmitted through it. More specifically, the *specular reflection* is the interaction of a radio wave with a flat and smooth surface whose dimension is larger than the wavelength. In this case, the power of the reflected path received at the RX

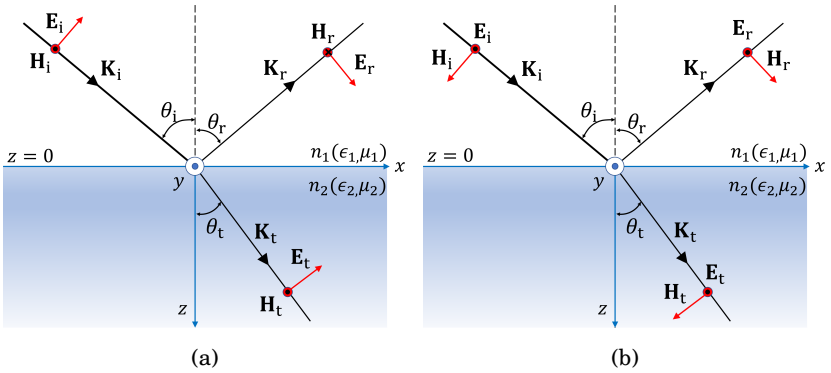

Figure 2.2. Reflection and transmission of a plane wave incident at the interface of two lossless media with a slanting angle: (a) parallel polarization and (b) Perpendicular polarization.

is affected by the reflection coefficient Γ, which depends on the dielectric properties of the material surface, wave polarization, incidence angle, and frequency. Transmission, on the other hand, deals with the absorption and penetration of radio waves through an interacting object. At this point, it would be worth distinguishing between the term *transmission* and *penetration*. The former is a typical term referring to the propagation of radio waves from one medium to another with infinite depth. The latter is used when the second medium is of finite depth. However, the two terms described above are used interchangeably in this thesis and the studies involved. The situation of an impinging plane wave onto the boundary the dielectric material can be distinguished between two cases: (1) Transverse Magnetic (TM) wave when **E** and **H** field components are parallel and perpendicular to the plane of incidence, respectively, known as parallel polarization, and (2) Transverse Electric (TE) wave when **E** and **H** field components are perpendicular and parallel to the plane of incidence, known as perpendicular polarization. Figure 2.2 illustrates the transmission and reflection of plane waves between two media.

Now, let θ_i, θ_t, and θ_r be the angle of incidence, transmission, and reflection, respectively. The interface between two dielectric media is characterized by their respective refractive index n_1 and n_2. The refractive index, $n = \sqrt{\mu\epsilon}$, is a dimensionless quantity that defines the dielectric and magnetic properties of a medium governing the waves' propagation. The direction of propagation of the incident, transmitted, and reflected wave is denoted by the propagation vectors $\mathbf{K_i}$, $\mathbf{K_t}$ and $\mathbf{K_r}$, respectively. From *Snell's law*, we know that $\theta_\mathrm{i} = \theta_\mathrm{r}$. The angle of the transmitted wave is

$$\frac{\sin\theta_{\mathrm{t}}}{\sin\theta_{\mathrm{i}}} = \frac{\sqrt{\mu_1\epsilon_1}}{\sqrt{\mu_2\epsilon_2}} = \frac{n_1}{n_2}, \tag{2.41}$$

where ϵ_1, μ_1 and ϵ_2, μ_2 are the permittivity and permeability of the two media. For most of the cases of interest in radio wave propagation and studies in this thesis, materials are considered non-magnetic and require $\mu_{\mathrm{r}} = 1$. Thus, $\mu_1 = \mu_2 = \mu_0$, therefore, (2.41) reduces to

$$\frac{\sin\theta_{\mathrm{t}}}{\sin\theta_{\mathrm{i}}} = \frac{\sqrt{\epsilon_1}}{\sqrt{\epsilon_2}} = \frac{n_1}{n_2}. \tag{2.42}$$

Reflection and transmission coefficients can be calculated by applying the boundary conditions for the continuity of tangential field components of **E** and **H** across the interface. For parallel (TM) polarization, application of boundary conditions to the **E** leads to

$$E_{\mathrm{i}}\cos\theta_{\mathrm{i}} + E_{\mathrm{r}}\cos\theta_{\mathrm{r}} = E_{\mathrm{t}}\cos\theta_{\mathrm{t}}, \tag{2.43}$$

using (2.41) yields

$$(E_{\mathrm{i}} + E_{\mathrm{r}})\cos\theta_{\mathrm{i}} = E_{\mathrm{t}}\sqrt{1 - \frac{\epsilon_1}{\epsilon_2}\sin^2\theta_{\mathrm{i}}}. \tag{2.44}$$

Similarly, applying boundary condition to **H** that has single component in the y axis direction gives

$$(E_{\mathrm{i}} - E_{\mathrm{r}})\sqrt{\epsilon_1} = E_{\mathrm{t}}\sqrt{\epsilon_2}. \tag{2.45}$$

Solving (2.44) and (2.45) provides the reflection coefficient $\Gamma_{\parallel}$ and transmission coefficient $T_{\parallel}$, respectively, as

$$\Gamma_{\parallel} = \frac{E_{\mathrm{r}}}{E_{\mathrm{i}}} = \frac{\sqrt{\frac{\epsilon_2}{\epsilon_1} - \sin^2\theta_{\mathrm{i}}} - \frac{\epsilon_2}{\epsilon_1}\cos\theta_{\mathrm{i}}}{\sqrt{\frac{\epsilon_2}{\epsilon_1} - \sin^2\theta_{\mathrm{i}}} + \frac{\epsilon_2}{\epsilon_1}\cos\theta_{\mathrm{i}}}, \tag{2.46}$$

$$T_{\parallel} = \frac{E_{\mathrm{t}}}{E_{\mathrm{i}}} = \frac{2\sqrt{\frac{\epsilon_2}{\epsilon_1}}\cos\theta_{\mathrm{i}}}{\sqrt{\frac{\epsilon_2}{\epsilon_1} - \sin^2\theta_{\mathrm{i}}} + \frac{\epsilon_2}{\epsilon_1}\cos\theta_{\mathrm{i}}}, \tag{2.47}$$

and when θ_{i} approaches 90°, we have $T = 1 + \Gamma$.

Applying the boundary conditions for the perpendicular (TE) polarization, we get

$$E_{\mathrm{i}} + E_{\mathrm{r}} = E_{\mathrm{t}}, \tag{2.48}$$

$$(E_{\mathrm{i}} - E_{\mathrm{r}})\sqrt{\epsilon_1}\cos\theta_{\mathrm{i}} = E_{\mathrm{t}}\sqrt{\epsilon_2}\cos\theta_{\mathrm{t}}, \tag{2.49}$$

and solving for $\Gamma_\perp$ and $T_\perp$, respectively,

$$\Gamma_\perp = \frac{E_{\mathrm{r}}}{E_{\mathrm{i}}} = \frac{\cos\theta_{\mathrm{i}} - \sqrt{\dfrac{\epsilon_2}{\epsilon_1} - \sin^2\theta_{\mathrm{i}}}}{\sqrt{\dfrac{\epsilon_2}{\epsilon_1} - \sin^2\theta_{\mathrm{i}}} + \cos\theta_{\mathrm{i}}}, \tag{2.50}$$

$$T_\perp = \frac{E_{\mathrm{t}}}{E_{\mathrm{i}}} = \frac{2\cos\theta_{\mathrm{i}}}{\sqrt{\dfrac{\epsilon_2}{\epsilon_1} - \sin^2\theta_{\mathrm{i}}} + \cos\theta_{\mathrm{i}}}. \tag{2.51}$$

In the case of layered dielectric materials where incident wave from one medium penetrates the second medium and emerges in the third medium, and so forth, the calculation of reflection and transmission coefficients becomes more complex. This resembles the situation in which radio waves penetrate a building, and wall structures are typically comprised of several layers with different dielectric properties. The combined reflection and transmission coefficients for a dielectric material with two layers are evaluated by assuming partial waves and are [43]

$$\Gamma = \frac{\Gamma_1 + \Gamma_2 e^{-j2\ell_{\mathrm{e}}}}{1 + \Gamma_1\Gamma_2 e^{-j2\ell_{\mathrm{e}}}}, \tag{2.52}$$

$$T = \frac{T_1 T_2 e^{-j\ell_{\mathrm{e}}}}{1 + \Gamma_1\Gamma_2 e^{-j2\ell_{\mathrm{e}}}} \tag{2.53}$$

where T_1 and Γ_1 refers to the transmission and reflection coefficients from air to dielectric material, respectively, and T_2 and Γ_2 from dielectric to air, respectively. ℓ_{e} corresponds to the electrical length of a given dielectric layer with thickness t_{d} and depends on frequency, θ_{t}, and its ϵ_{r}

$$\ell_{\mathrm{e}} = \frac{2\pi}{\lambda}\sqrt{\epsilon_{\mathrm{r}}}t_{\mathrm{d}}\cos\theta_{\mathrm{t}}, \tag{2.54}$$

It is noteworthy that Γ can be positive or negative depending on whether ϵ_2 is greater or less than ϵ_1. When media are lossy, ϵ_1 and ϵ_2 are complex quantities, thus, Γ and T will also be complex quantities. This implies that Γ or T will introduce a phase shift at the interface boundary upon reflection or transmission. If the second medium is a perfect electric conductor (PEC) it will reflect all the incident energy to the same medium, i.e., $T = 0$ and

$\Gamma = -1$. The $\Gamma_{\parallel} = 0$ at *Brewster's* angle, given as

$$\theta_{\mathrm{B}} = \sqrt{\frac{\epsilon_2}{\epsilon_1 + \epsilon_2}}, \tag{2.55}$$

and total reflection occurs at the incident angle

$$\theta_{\mathrm{i}} \geq \sqrt{\frac{\epsilon_2}{\epsilon_1}}. \tag{2.56}$$

The ITU-R P.2040-1 [45] simplifies the reflection (R) and transmission (T) coefficients for a single-layer slab as

$$R = \frac{\Gamma(1 - e^{-j2q})}{1 - \Gamma^2 e^{-j2q}} \tag{2.57}$$

$$T = \frac{(1 - \Gamma^2)e^{-jq}}{1 - \Gamma^2 e^{-j2q}} \tag{2.58}$$

where Γ is the reflection coefficient from air to the material slab due to parallel or perpendicular polarization of the incident $\mathbf{E}$ field and q is given as

$$q = \frac{2\pi d}{\lambda}\sqrt{\epsilon - \sin^2\theta_{\mathrm{i}}} \tag{2.59}$$

where d is the thickness of the slab, θ_{i} is the incident angle, and $\epsilon = \epsilon' - j\epsilon''$ is the permittivity. The real and imaginary part of the permittivity are $\epsilon' = af^b$ and $\epsilon'' = 17.98(\sigma/f)$, respectively, with $\sigma = cf^d$ and f as the frequency in GHz. The values for $a, b, c,$ and d vary with frequency for different materials and are available for some materials in Table 3 of ITU-R P.2040-2 [66]. The same ITU-R approximates attenuation rate in $\mathrm{dB/m}$ for dielectric and conductors, respectively, as

$$A_{\mathrm{dielectric}} = 1636\left(\frac{\sigma}{\sqrt{\epsilon'}}\right) \text{ and} \tag{2.60}$$

$$A_{\mathrm{conductor}} = 545.8\sqrt{\sigma f}. \tag{2.61}$$

2.2.3 Fresnel zone

Before examining the wave diffraction problem, it is important to determine the local nature of wave propagation in space as it sets a foundation for other complex propagation mechanisms. Let us consider a spherical wave emanating from TX that arrives at a given RX location on the x axis

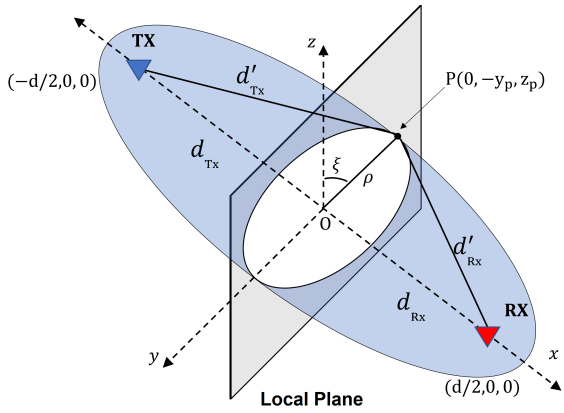

Figure 2.3. Local nature of wave propagation with TX and RX as the foci of Fresnel ellipsoid.

with a separation of distance d, as illustrated in Figure 2.3. Consider a local plane at the origin O of the Cartesian coordinate system, midway between TX and RX, and a point $P(0, -y_{\rm p}, z_{\rm p})$ on it such that it is located on the circumference of a circular region of the local plane. Suppose an absorbing screen of finite dimensions now substitutes the local plane. The circular region at $x = 0$ can be represented as a transmission coefficient $T(\rho)$, which is function of the radius ρ. The incident **E** field at the plane at $x = 0$ is

$$E(0, y, z) = E_0 \frac{e^{-jkd'_{\rm TX}}}{d'_{\rm TX}}, \tag{2.62}$$

where $d'_{\rm TX} = \sqrt{(d_{\rm TX})^2 + \rho^2} = \sqrt{(d/2)^2 + \rho^2}$ is the distance between point P and TX. Now the **E** field at the RX past the absorbing screen can be obtained by applying the Kirchhoff-Huygens integral on the product of incident field given by (2.62) and transmission coefficient $T(\rho)$ as

$$E(d, 0, 0) = \int_0^{\infty} \int_0^{2\pi} E_0 \frac{e^{-jkd_{\rm TX}}}{d_{\rm TX}} T(\rho) \frac{-jke^{-jkd_{\rm RX}}}{2\pi d_{\rm RX}} \, d\xi \rho \, d\rho, \tag{2.63}$$

where $d'_{\rm RX} = \sqrt{(d_{\rm RX})^2 + \rho^2} = \sqrt{(d/2)^2 + \rho^2}$ is the distance between integration point and RX. Assuming a Gaussian approximation of the transmission coefficient, i.e., $T(\rho) = \exp\left(-\rho^2/w^2\right)$, where $w = \rho/e$. This transforms the expression (2.63) to

$$E(d, 0, 0) = \int_0^{\infty} \int_0^{2\pi} E_0 \frac{e^{-jkd'_{\rm TX}}}{d'_{\rm TX}} \exp\left(\frac{-\rho^2}{w^2}\right) \frac{-jke^{-jkd'_{\rm RX}}}{2\pi d'_{\rm RX}} \, d\xi \rho \, d\rho. \tag{2.64}$$

To evaluate the integral in (2.64) in closed form, we observe that the

Gaussian function limits the contribution of ρ near the origin O, and therefore, $d_{\mathrm{TX}}^{'}$ and $d_{\mathrm{RX}}^{'}$ can be approximated as

$$\begin{aligned} d_{\mathrm{TX}}^{'} &= \sqrt{(d_{\mathrm{TX}}/2)^2 + \rho^2} \quad \approx d_{\mathrm{TX}} + \frac{\rho^2}{2d_{\mathrm{TX}}} \\ d_{\mathrm{RX}}^{'} &= \sqrt{(d_{\mathrm{RX}}/2)^2 + \rho^2} \quad \approx d_{\mathrm{RX}} + \frac{\rho^2}{2d_{\mathrm{RX}}}. \end{aligned} \tag{2.65}$$

Furthermore, with the preceding approximation and the fact that the denominator of (2.64) and (2.65) results in only a small variation of the integrand, we can further reduce the expression (2.65) to $d_{\mathrm{TX}}^{'} = d_{\mathrm{RX}}^{'} \approx d_{\mathrm{TX}} = d_{\mathrm{RX}} = d/2$. Also, the integrand becomes independent of ξ close to the origin O, thus solving the integral yields

$$E(d, 0, 0) = \left(E_0 \frac{e^{-jkd}}{d}\right) \frac{1}{1 - j\dfrac{2d}{kw^2}}, \tag{2.66}$$

where the second part of (2.66) refers to the field distorting factor due to the absorbing screen and depends on the radius w of the hole in the screen, the **E** field at the RX becomes less distorted as w increases. We can quantify this field distortion with the error ζ as

$$\zeta = \frac{2d}{kw^2} = \frac{\lambda d}{2\pi w^2}. \tag{2.67}$$

The above expressions tell us that phase of the **E** field at RX is distorted by a factor $\arctan\zeta$, while its amplitude is distorted by the factor $\sqrt{1+\zeta^2}$. For a given error ζ, the radius w of the hole in the absorbing screen provides the cross-section of the local region in space that allows the fields to propagate from TX to RX, and its more generic form is given as

$$w = \sqrt{\frac{\lambda d_{\mathrm{TX}} d_{\mathrm{RX}}}{\pi\zeta(d_{\mathrm{TX}} + d_{\mathrm{RX}})}}. \tag{2.68}$$

This renders the concept of Fresnel zones that are ellipsoid of revolution about the LOS path between TX and RX. For nth Fresnel zone, the difference between the LOS path $d_{\mathrm{TX}} + d_{\mathrm{RX}}$ and the path through any point on the ellipsoid is

$$(d_{\mathrm{TX}}^{'} + d_{\mathrm{RX}}^{'}) - (d_{\mathrm{TX}} + d_{\mathrm{RX}}) = n\frac{\lambda}{2}. \tag{2.69}$$

If $d_{\mathrm{TX}} + d_{\mathrm{RX}} \gg \lambda$, we can approximate (2.69) using (2.65), the radius of nth Fresnel zone w_{Fn} is given by

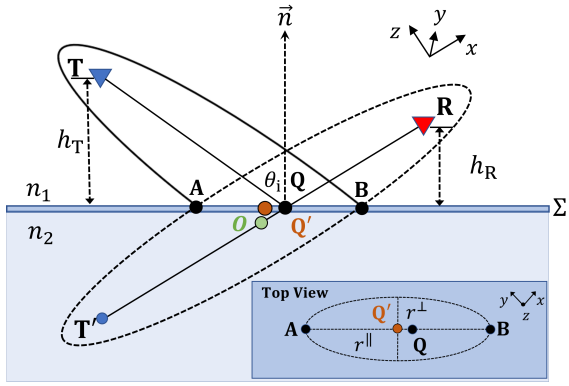

Figure 2.4. Interface Fresnel zone (IFZ) for the reflection path between TX and RX.

$$w_{\mathrm{Fn}} = \sqrt{n\frac{\lambda(d_{\mathrm{TX}}d_{\mathrm{RX}})}{d_{\mathrm{TX}}+d_{\mathrm{RX}}}}. \tag{2.70}$$

By analyzing (2.68) and (2.70), we can observe that distortion error $\zeta = 1/n\pi$. This implies that for $n = 1$, the phase error is $60°$, while the amplitude error is $10\,\%$ (Section 5.1a, Page 112 [67]). From this, we can conveniently infer that the wave propagation phenomenon has a local nature that can be elegantly described through the concept of Fresnel zones. Any object intruding Fresnel zones can cause the additional contribution to the E field at RX due to scattering, which can become significant for $n = 1$, i.e., the first Fresnel zone. For the simple case, as illustrated in Figure 2.3, the Fresnel zone is widest at the midpoint between TX and RX, hence the size of the first Fresnel zone is $w_{\mathrm{F1}} = \sqrt{\lambda d}/2$. This indicates that the Fresnel zone essentially represents the spatial volume around the electromagnetic wave path trajectory influencing the received field at the RX. The $w_{\mathrm{F_n}}$ is frequency dependent; hence, the Fresnel volume is broader at low and narrow at high frequencies for a given TX and RX separation.

The concept of the Fresnel zone can be extended to the reflections of radio waves. This entails that the reflecting surface must be flat and electrically large, occupying several Fresnel reflection zones to generate reflected field components such that the reflection coefficient $\Gamma \to 1$. This is commonly referred to as the *interface Fresnel zone* or *Fresnel reflection zone* [68,69] and is illustrated in Figure 2.4. For raytracing simulations and other practical purposes, it is crucial to determine the size of the *interface Fresnel zone* to evaluate if the reflected contribution is specular and has significant power. To characterize the *interface Fresnel zone*, let us consider a radiating source T at a height h_{T} from a smooth plane surface interface

$\sum$ between two media with refractive index n_1 and n_2, respectively. The radio wave emitted from T is incident on the interface $\sum$ at the point of incidence Q with an angle θ_i and arrives at the receiver point R at a height h_R from the interface $\sum$ after getting reflected from it. Also, assuming that the reflected wave is entirely located inside the plane of incidence, perpendicular to the interface $\sum$ and passes through T and R. The total length of the reflected path is denoted by $l_\mathrm{p} = \overline{TQ} + \overline{QR}$, and the direct path length $r_\mathrm{d} = \overline{TR}$.

To evaluate the size of the *interface Fresnel zone*, we consider the image source T' located symmetrically with respect to T on the other half space of the interface $\sum$. The separation $\overline{T'R}$ equals the reflected path length l_p. The problem is thus reduced to finding the planar section of the Fresnel volume corresponding to T' and R. It is important to emphasize here that the origin of the Cartesian coordinate system is located at the midpoint between T' and R and is not related to the interface. Let us clarify and introduce some other notations to describe the problem better. The plane containing the rotational axis of the Fresnel volume is represented by $\sum_\mathrm{F}$ and is perpendicular to the interface $\sum$. The rotational axis is oriented along the x axis, and $\sum_\mathrm{F}$ is perpendicular to the z axis, which means it lies in the xy plane in the Cartesian coordinate system, where x_0 represents the x-coordinate of the point Q. The interface $\sum$ is parallel to the z axis and intersects the rotational axis at point $\mathrm{Q} = (x_0, 0, 0)$ between point A and B. Thus the equation of the interface plane can be expressed as

$$x = x_0 + gy, \tag{2.71}$$

where $g = \tan\theta_\mathrm{i}$. The Fresnel volume with T' and R as *foci* constitutes all the points that satisfy the following condition

$$\left[\left(x - \frac{l_\mathrm{p}}{2}\right)^2 + r^2\right]^{1/2} + \left[\left(x + \frac{l_\mathrm{p}}{2}\right)^2 + r^2\right]^{1/2} - l_\mathrm{p} = \frac{\lambda}{2}, \tag{2.72}$$

where $r^2 = y^2 + z^2$, and λ refers to the wavelength in meters. Algebraic simplification of (2.72) yields

$$\frac{x^2}{a_1^2} + \frac{y^2}{b_1^2} = 1, \tag{2.73}$$

with $a_1 = \frac{l_\mathrm{p}(2+\lambda)}{4}$ and $b_1 = \frac{\lambda}{2}\sqrt{l_\mathrm{p} + \frac{\lambda}{4}}$ as the semi-axis of the ellipsoid. The ratio $v = b_1/a_1 \approx \sqrt{\frac{\lambda}{\mathrm{p}}}$ is called *fatness ratio*. Now the Cartesian coordinates of the points A, B of the intersection of plane $\sum$ with the Fresnel volume

in the plane $\sum_{\mathrm{F}}$ is obtained by solving (2.71) and (2.73)

$$y_{\mathrm{A,B}} = \frac{-2x_0gb_1^2 \pm \sqrt{\mathrm{D_c}}}{2(a_1^2 + g^2b_1^2)}, \quad \text{and} \tag{2.74}$$

$$x_{\mathrm{A,B}} = \frac{2x_0ga_1^2 \pm g\sqrt{\mathrm{D_c}}}{2(a_1^2 + g^2b_1^2)}, \tag{2.75}$$

where $\mathrm{D_c} = 4g^2b_1^4x_0^2 + 4b_1^2(a_1^2 - x_0^2)(a_1^2 - b_1^2g^2)$.

Let us characterize the size of the *interface Fresnel zone* ellipse by defining its *major* or *in-plane* and *minor* or *transverse* semi-axis, denoted as $r^{\parallel}$ and $r^{\perp}$, respectively. The *major* or *in-plane* semi-axis $r^{\parallel}$ is one-half of the distance between A and B, given as

$$r^{\parallel} = \frac{1}{2}\overline{\mathrm{AB}} = \frac{1}{2}\left[(x_{\mathrm{B}} - x_{\mathrm{A}})^2 + (y_{\mathrm{B}} - y_{\mathrm{A}})^2\right]^{1/2}, \tag{2.76}$$

$$r^{\parallel} = \frac{1}{2}\frac{\sqrt{1+g^2}\sqrt{\mathrm{D_c}}}{a_1^2 + g^2b_1^2} = b_1\frac{\sqrt{1+g^2}}{1+g^2v^2}\left[1 - \frac{x_0^2}{a_1^2} + g^2v^2\right]^{1/2}. \tag{2.77}$$

It is noteworthy that if $h_{\mathrm{T}} \neq h_{\mathrm{R}}$, the actual center of the *Fresnel interface zone* ellipse is located at $\mathrm{Q}' = (x_{\mathrm{Q}'}, x_{\mathrm{y}'}, 0)$, the mid-point between A and B, instead of Q, as shown in Figure 2.4. The x and y coordinates of Q' are given as

$$x_{\mathrm{Q}'} = \frac{1}{2}(x_{\mathrm{A}} + x_{\mathrm{B}}) = \frac{x_0a_1^2}{a_1^2 + g^2b_1^2}, \tag{2.78}$$

$$y_{\mathrm{Q}'} = \frac{1}{2}(y_{\mathrm{A}} + y_{\mathrm{B}}) = -\frac{x_0gb_1^2}{a_1^2 + g^2b_1^2}. \tag{2.79}$$

Solving for the minor or *transverse* semi-axis $r^{\perp}$, we get

$$r^{\perp} = b_1\frac{1}{\sqrt{1+g^2v^2}}\left[1 - \frac{x_0^2}{a_1^2} + g^2v^2\right]^{1/2}. \tag{2.80}$$

Expressing the terms x_0 and l_{p} in the given practical quantities as

$$x_0 = \frac{1}{2}(h_{\mathrm{R}} - h_{\mathrm{T}})\sqrt{1+g^2}, \tag{2.81}$$

$$l_{\mathrm{p}} = (h_{\mathrm{T}} + h_{\mathrm{R}})\sqrt{1+g^2}, \tag{2.82}$$

$$g = \tan\theta_{\mathrm{i}} = \frac{r_{\mathrm{d}}}{(h_{\mathrm{T}} + h_{\mathrm{R}})}. \tag{2.83}$$

When $h_{\mathrm{T}} = h_{\mathrm{R}}$, the $x_0 = 0$, therefore, (2.77) and (2.80) are reduced to

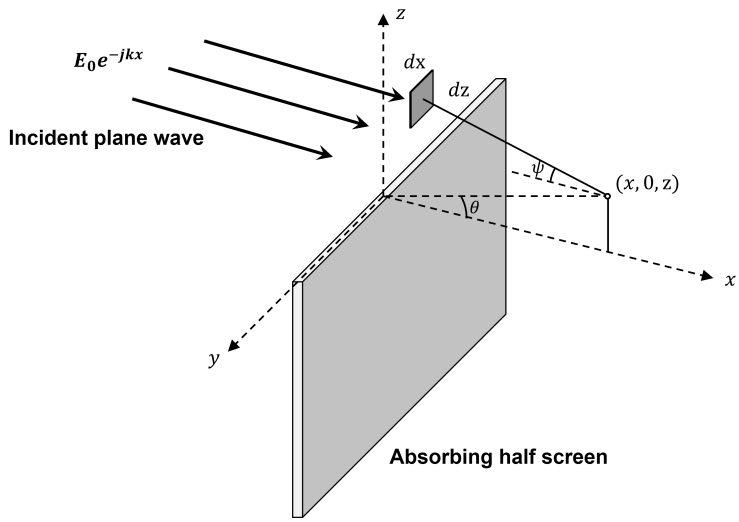

Figure 2.5. Diffraction of a plane wave from absorbing half screen.

$$r^{\parallel} = b_1 \sqrt{\frac{1+g^2}{1+g^2 v^2}}, \tag{2.84}$$

$$r^{\perp} = b_1. \tag{2.85}$$

Finally, the area $\mathbb{A}_{\mathrm{IFZ}}$ of the *interface Fresnel zone* is given as

$$\mathbb{A}_{\mathrm{IFZ}} = \pi \cdot r^{\parallel} \cdot r^{\perp} = \frac{\pi b_1^2 \sqrt{1+g^2}}{1+g^2 v^2} \left[1 - \frac{x_0^2}{a_1^2} + g^2 v^2 \right]. \tag{2.86}$$

2.2.4 Diffraction

The diffraction of a plane wave from an edge is a precursor for various shadowing problems in radio engineering. Figure 2.5 manifests this process where a plane wave originating from a far-off source illuminates an absorbing screen whose edge center is situated at the origin in the Cartesian coordinate system. The plane wave propagating along the x axis with angle of incidence $\psi = 0$ has an **E** field component along the y axis, and is given as

$$E_y = E_0 e^{-jkx}, \tag{2.87}$$

where E_0 is the amplitude of the plane wave in free space. The scalar Kirchhoff approximation allows us to calculate the field diffracted by the edge in different regions past the absorbing screen [70–72], now assuming

that the receiving point is at $y = 0$ plane, we have

$$E_y = E_0 \frac{jk}{4\pi} \int_0^\infty \int_{-\infty}^\infty (1 + \cos\psi) \frac{e^{-jkd_\mathrm{R}}}{d_\mathrm{R}} \, dy' \, dz', \tag{2.88}$$

where $d_\mathrm{R} = \sqrt{x^2 + y'^2 + (z - z')^2}$ is the distance between the integration and the receiver point. The integral in (2.88) has two components, i.e., y' and z' integration. Let us first consider the y' integration where the main contribution originates from the Fresnel region of y', which is small compared to x for $x \gg \lambda$. The center of this Fresnel region is the stationary-phase point where the derivative $-jkd_\mathrm{R} \, dy'$ disappears. The stationary-phase approximation is an asymptotic analysis method for describing the limiting behavior of a quantity. It is based on the cancellation of sinusoids with rapidly varying phases. In the region of primary contribution to the y' integral, the terms $\cos\psi$ and d_R in the denominator varies by a small fractional amount and can be considered as constant; however, d_R in the exponent can vary by several wavelengths. Therefore, making a second order approximation on d_R for the exponent, we get

$$d_\mathrm{R} \approx \rho_\mathrm{R} + \frac{y'^2}{2\rho_\mathrm{R}}, \tag{2.89}$$

where $\rho_\mathrm{R} = \sqrt{x^2 + (z - z')^2}$. Let's first simply the y' integration part of the equation (2.88) as

$$\int_{-\infty}^\infty (1 + \cos\psi) \frac{e^{-jkd_\mathrm{R}}}{d_\mathrm{R}} \, dy' \approx (1 + \cos\psi) \frac{e^{-jk\rho_\mathrm{R}}}{\rho_\mathrm{R}} \int_{-\infty}^\infty e^{\frac{-jky'^2}{2\rho_\mathrm{R}}} \, dy', \tag{2.90}$$

using the substitution $u = y' e^{j\pi/4} \sqrt{k/2\rho_\mathrm{R}}$, the **E** field at the RX point is given by solving (2.90) for closed form as

$$E_y = E_0 \frac{e^{j\pi/4}}{2} \sqrt{\frac{k}{2\pi}} \int_0^\infty (1 + \cos\psi) \frac{e^{-jk\rho_\mathrm{R}}}{\rho_\mathrm{R}} \, dz'. \tag{2.91}$$

The integration over z' is evaluated for the RX points in the illuminated region for $z > 0$, shadow region $z < 0$, and at the transition region $z = 0$. The stationary-phase method is also applied for the z' integration, and in (2.91), the stationary-phase point is at $z' = z$ where the derivative $d\rho_\mathrm{R} / \, dz'$ disappears. The second order approximation of ρ_R about the stationary-phase point gives

$$\rho_\mathrm{R} \approx x + \frac{1}{2x}(z' - z)^2. \tag{2.92}$$

Now separating the stationary-point contribution $z' = z$ from the endpoint contribution $z' = 0$, the expression in (2.91) can be written as

$$E_y = E_0 \frac{e^{j\pi/4}}{2}\sqrt{\frac{k}{2\pi}}\left[\int_{-\infty}^{\infty}(1+\cos\psi)\frac{e^{-jk\rho_{\mathrm{R}}}}{\sqrt{\rho_{\mathrm{R}}}}\,dz' - \int_{-\infty}^{0}(1+\cos\psi)\frac{e^{-jk\rho_{\mathrm{R}}}}{\sqrt{\rho_{\mathrm{R}}}}\,dz'\right]. \tag{2.93}$$

Following the same approach as y' integration, the first integral in (2.93) can be solved by evaluating the amplitude terms at the stationary-phase point $z' = z$, where $\psi = 0$ and $\rho_{\mathrm{R}} = x$ can be taken outside the integral and ρ_{R} in the exponent is approximated using (2.92), yielding

$$\int_{-\infty}^{\infty}(1+\cos\psi)\frac{e^{-jk\rho_{\mathrm{R}}}}{\sqrt{\rho_{\mathrm{R}}}}\,dz' \approx \frac{2e^{-jkx}}{\sqrt{x}}\int_{-\infty}^{\infty}e^{-j\frac{k}{2x}(z'-z)^2}\,dz' = 2e^{-j\pi/4}\sqrt{\frac{2\pi}{k}}e^{-jkx}. \tag{2.94}$$

The second integral in (2.93) results in the main contribution originating from the region around the endpoint $z' = 0$. Assuming that z is large enough to differentiate stationary-phase from the endpoint, the contribution from the endpoint can be approximated about the point $z' = 0$ such that $\rho_{\mathrm{R}} \approx \rho - z'\frac{z}{\rho}$, where $\rho = \sqrt{x^2+z^2}$ is the distance from the edge of absorbing screen to the receiver point. With the preceding assumption, the second integral is evaluated as

$$\int_{-\infty}^{0}(1+\cos\psi)\frac{e^{-jk\rho_{\mathrm{R}}}}{\sqrt{\rho_{\mathrm{R}}}}\,dz' = (1+\cos\theta)\frac{e^{-jk\rho}}{\sqrt{\rho}}\int_{-\infty}^{0}e^{jk(z'\frac{z}{\rho})}\,dz' = \frac{1+\cos\theta e^{-jk\rho}}{jk(z/\rho)\sqrt{\rho}}, \tag{2.95}$$

where θ is the angle between the x axis and the line from the edge of the absorbing screen and the receiving point, such that $\sin\theta = z/\rho$, as illustrated in Figure 2.5. Now, substituting (2.94) and (2.95) in (2.93), we get the $\mathbf{E}$ field in the illuminated region $z > 0$ as

$$E_y = E_0 e^{-jkx} + E_0\frac{e^{-j(\pi/4+k\rho)}}{\sqrt{\rho}}D(\theta), \tag{2.96}$$

where $D(\theta)$ is the diffraction coefficient give as

$$D(\theta) = -\frac{1+\cos\theta}{2\sin\theta\sqrt{2\pi k}}. \tag{2.97}$$

The expression in (2.96) is the sum of the incident and diffracted field in the illuminated region with a direction dependence of $D(\theta)$, which is singular on the shadow boundary $z = 0$ between illuminated and the shadow region.

This is because stationary-phase and endpoints are not well differentiated at the shadow boundary, and integral approximation in (2.94) is not valid anymore.

In $z < 0$ region, the stationary-phase point in the integrand of (2.91) is now situated outside the integration range. When $|z|$ is large, the stationary-phase point is well differentiated from the endpoint, allowing us to utilize the endpoint approximation for the integral. Thus using $\rho_{\mathrm{R}} \approx \rho - z'\frac{z}{\rho}$, the (2.91) reduces to

$$E_y = E_0 \frac{e^{j\pi/4}}{2}\sqrt{\frac{k}{2\pi}}(1+\cos\theta)\frac{e^{-jk\rho_{\mathrm{R}}}}{\sqrt{\rho}}\int_0^{\infty} e^{jk(z'\frac{z}{\rho})}\,dz'. \tag{2.98}$$

Solving the integral in (2.98) where k gets a negligibly small negative imaginary part for the convergence at the upper limit, we get

$$E_y = E_0 \frac{e^{-j(\pi/4+k\rho)}}{\sqrt{\rho}} D(\theta), \tag{2.99}$$

where the diffraction coefficient $D(\theta)$ is the same as that in (2.97). This shows that the **E** field is only made of the cylindrical wave that propagates away from the edge of the absorbing screen. Finally, the total field past the absorbing screen in both the illuminated and the shadow region can be expressed as

$$E_y = E_0 e^{-jkx} U(\theta) + E_0 \frac{e^{-j(\pi/4+k\rho)}}{\sqrt{\rho}} D(\theta), \tag{2.100}$$

where $U(\theta)$ in the first part of (2.100) is a unit step function indicating the presence of the incident **E** field in the illuminated region only. The second part of (2.100) defines the cylindrical wave due to the edge of the absorbing screen. Equation (2.100) is popularly known as *geometric theory of diffraction* (GTD) of plane wave incident onto an absorbing screen, which is based on the premise of GTD theory introduced by J.B. Keller [73]. Withal, there is a limitation of GTD that it is not valid around the transition region between the illumination and the shadow region, i.e., shadow boundary. This is because $D(\theta)$ exhibits a discontinuity around the shadow boundary, which does not represent the bounded and continuous field in reality. This deficiency can be addressed by applying *uniform theory of diffraction* (UTD) [74], which derives a function to eliminate the singularity of $D(\theta)$ and makes the total **E** field continuous across the shadow boundary. Hence, the (2.100) can be written as

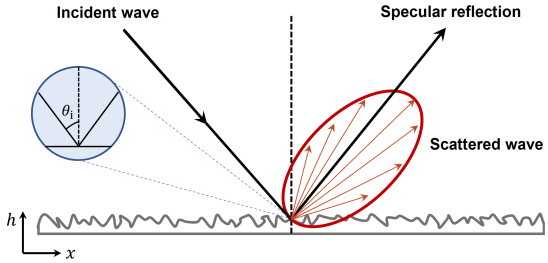

Figure 2.6. Scattering of a plane wave incident on a rough surface profile.

$$E_y = E_0 e^{-jkx} U(z) + E_0 \frac{e^{-j(\pi/4+k\rho)}}{\sqrt{\rho}} D_{\mathrm{T}}(\theta), \tag{2.101}$$

where $D_{\mathrm{T}}(\theta) = D(\theta)F(S)$ is the diffraction coefficient from UTD, with $D(\theta)$ as GTD diffraction coefficient given by (2.97) and $F(S)$ being the transition function which can be calculated as

$$F(S) = \sqrt{2\pi S}\left[f(\sqrt{2S/\pi}) + jg(\sqrt{2S/\pi})\right]. \tag{2.102}$$

The functions $f(\Theta)$ and $g(\Theta)$ are related to the Fresnel integrals and can be evaluated for the positive values of Θ using the approximations described in [75], as

$$f(\Theta) = \frac{1 + 0.926\Theta}{2 + 1.792\Theta + 3.104\Theta^2}, \tag{2.103}$$

$$g(\Theta) = \frac{1}{2 + 4.142\Theta + 3.492\Theta^2 + 6.670\Theta^3}. \tag{2.104}$$

2.2.5 Scattering

Scattering of electromagnetic waves occurs when a plane wave is incident onto a rough surface [76]. It is a profound problem in electromagnetic wave propagation that has a strong effect on the received power at the RX antenna. In the real world, no surface is ideally flat and smooth; therefore, the scattering of radio waves from a surface is greatly influenced by its morphology and roughness profile. Substantial studies have been carried out at both theoretical and experimental levels to address wave scattering problems for various applications [77–82]. Kirchhoff's theory [43, 83] investigates wave scattering in the far-field of a rough surface by assuming that the scattering points on the surface have finite height gradients. The effective reflection coefficient Γ_{rough} which deals with the power scattered

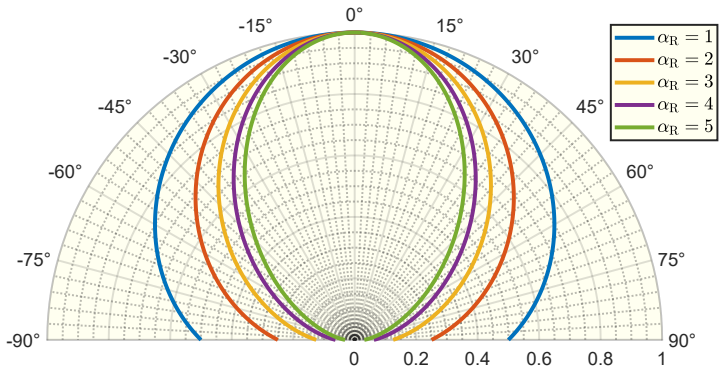

Figure 2.7. Normalized scattering patterns for different α_{R}.

in a specular direction, is given by

$$\Gamma_{\mathrm{rough}} = \Gamma_{\mathrm{specular}} e^{-2(k\sigma_{\mathrm{h}} \sin\theta_{\mathrm{i}})^2}, \tag{2.105}$$

where $\Gamma_{\mathrm{specular}}$ is the reflection coefficient from (2.46) or (2.50) for flat and smooth surface, σ_{h} refers to the standard deviation of the height distribution, $k = 2\pi/\lambda$ is the wavenumber in free space, and θ_{i} is the incident angle of the impinging wave with respect to the surface normal. Rayleigh criterion [84] provides a smooth surface approximation as $\sigma_{\mathrm{h}} = \lambda < 8/\cos\theta_{\mathrm{i}}$, while, Fraunhofer criterion [76, 85] lays out a more stern approximation as $\sigma_{\mathrm{h}} = \lambda < 32/\cos\theta_{\mathrm{i}}$. The relation (2.105) exhibits strong frequency dependence. Figure 2.6 demonstrates the scattering phenomenon from the rough surfaces in contrast to the specular reflection. The power scattered in the direction of specular reflection decreases and causes energy to spread in other directions as the surface is electrically more rough.

The effective roughness (ER) method [86] is another practical approach to model diffuse scattering from rough surfaces and the effect of small objects. ER method further categorizes the modeling of diffuse scattering as a non-directional Lambertian model or as a single-lobe directive model. The scattered field for the single-lobe directive model is given as

$$|\mathbf{E}_{\mathrm{s}}| = \left(\frac{S\mathbf{E}_{\mathrm{i}}}{r_i r_s} \cdot \frac{\lambda}{4\pi}\right)^2 \cdot \frac{dS\cos\theta_{\mathrm{i}}}{F_{\alpha_{\mathrm{R}}}} \cdot \left(\frac{1+\cos\psi_{\mathrm{R}}}{2}\right)^{\alpha_{\mathrm{R}}}, \tag{2.106}$$

where $\mathbf{E}_{\mathrm{i}}$ is the incident field, $S = |\mathbf{E}_{\mathrm{s}}|/|\mathbf{E}_{\mathrm{i}}| \in [0, 1]$ is the scattering coefficient, r_{i} and r_{s} are the distances of scatterers from TX and RX antennas, respectively, dS is elementary surface area, ψ_{R} is the angle between reflected and scattered wave directions, $\alpha_{\mathrm{R}} \in [1, 2, 3...]$ ascertains the width or directivity of the scattering lobe, and $F_{\alpha_{\mathrm{R}}}$ is the scaling factor described

by

$$F_{\alpha_{\mathrm{R}}} = \frac{1}{2^{\alpha_{\mathrm{R}}}} \cdot \sum_{\mathrm{j}=0}^{\alpha_{\mathrm{R}}} \binom{\alpha_{\mathrm{R}}}{\mathrm{j}} \cdot I_{\mathrm{j}}, \tag{2.107}$$

and

$$I_{\mathrm{j}} = \frac{2\pi}{\mathrm{j}+1} \cdot \left[\cos\theta_{\mathrm{i}} \cdot \sum_{w=0}^{\frac{\mathrm{j}-1}{2}} \binom{2w}{w} \cdot \frac{\sin^{2w}\theta_{\mathrm{i}}}{2^{2w}} \right]^{\frac{1-(-1)^{\mathrm{j}}}{2}}. \tag{2.108}$$

The normalized scattered patterns for different α_{R} are illustrated in Figure 2.7, demonstrating that the desired directivity of the scattering lobe can be achieved by selecting a suitable value of α_{R}.

2.3 Contributions of the thesis

2.3.1 Vehicle penetration loss at sub-6 GHz frequencies

Metalized automotive window films and glass are typical in automobiles for reducing thermal and ultraviolet (UV) flux into cars and controlling glare for night driving. However, metalization could adversely affect the communication of desired cellular radio signals into vehicles. This entails a thorough evaluation of radio wave propagation loss into vehicles, generally referred to as, Vehicle Penetration Loss (VPL), and is mathematically expressed as

$$L_{\mathrm{VPL}}[\mathrm{dB}] = 10\log_{10}\frac{\mathrm{P}_{\mathrm{out}}}{\mathrm{P}_{\mathrm{in}}}, \tag{2.109}$$

where P_{out} is the power level immediately outside the vehicle and P_{in} refers to the power level inside the vehicle. Referring to Section 2.3.3, we see that theoretically the transmission of radio waves through the interface between two media is characterized by the transmission coefficient, given by (2.58). The VPL in (2.109) is calculated from the measured channel data and is simply the difference of P_{out} without the car chassis and P_{in} that includes the effect of car chassis. VPL is characterized at sub-$6\,\mathrm{GHz}$ frequencies in [I] for automotive window films. For this purpose, ultra-wideband radio channel measurements were carried out on a modern hatchback passenger car inside an indoor industrial environment at an isolated storage facility in Helsinki. The directional characteristics of VPL were analyzed with respect to the car structure by circumnavigating the RX antenna at different angles around the car and with its windows

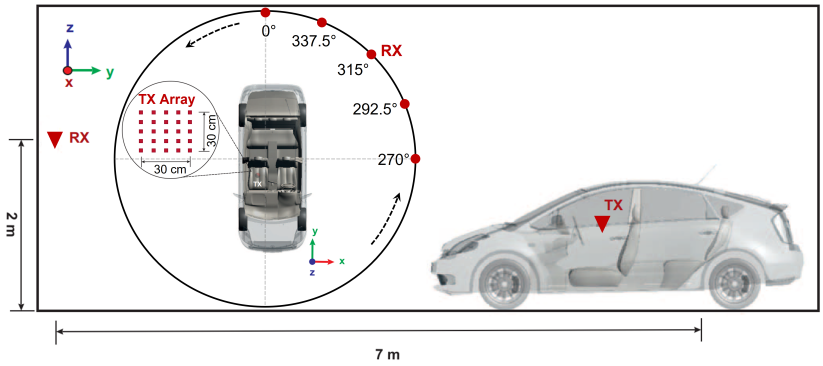

Figure 2.8. Setup layout for VPL measurements, top and side views.

covered with different coatings, as shown in Figure 2.8. The frequency domain measurement setup was implemented as multiple-input single-output (MISO) with a vector network analyzer (VNA) as the core data acquisition device. Mean VPL estimated for no coating, window film, and Aluminum foil cases are $3\,\mathrm{dB}$, $6.6\,\mathrm{dB}$, and $20.7\,\mathrm{dB}$, respectively over the full frequency band, i.e., $0.6 - 6\,\mathrm{GHz}$. The study strongly demonstrates that metalized automotive window film and metalized glass significantly attenuate radio signals penetrating into vehicles, reducing cellular radio coverage inside them.

2.3.2 Modeling specular reflections for the point cloud of an environment

Laser scanning of physical environments provides an accurate geometrical database in the form of a point cloud. Radio channel prediction employing the point cloud of an environment is a promising method at mmWave frequencies where specular reflections are significant propagation phenomena. The literature demonstrated that the ray-based radio channels prediction based on the effective roughness approach in the point cloud, described in 2.2.5, provides a reasonable prediction accuracy if the environment under consideration is small and diffuse dominant. However, specular paths dominate the radio channel when the environment becomes large and less cluttered, thereby requiring a mathematical conceptualization to improve the prediction accuracy in point cloud simulations. [II] presents the mathematical framework for simulating specular reflections based on a point cloud geometrical description of an environment. It evaluates the total specular reflected field as a coherent sum of the individual field contributions originating from the elementary surfaces over an area ap-

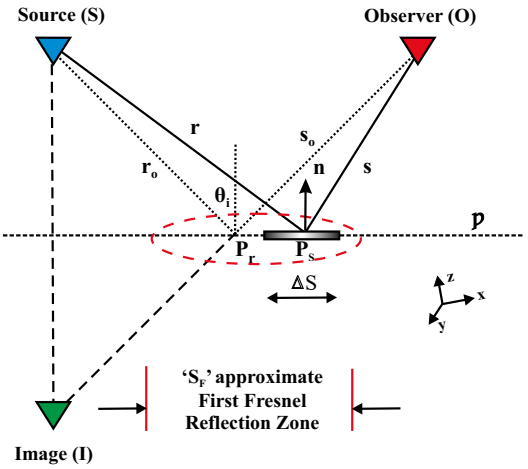

Figure 2.9. Geometrical illustration of specular reflection modeling for point cloud.

proximately equal to the first *Fresnel reflection zone* or *interface Fresnel zone*. The *interface Fresnel zone* is discussed thoroughly in Section 2.2.3.

Figure 2.9 illustrates the concept of modeling specular reflections for a given point cloud. The total reflected field $\mathbf{E}_{\mathrm{r}}(\mathbf{O})$ at the observation point $\mathbf{O}$ is the sum of individual field contributions $\mathbf{E}_{\mathrm{r}}(\Delta\mathrm{S})$ from elementary surfaces $\Delta\mathrm{S}$ that occupy the *interface Fresnel zone* $\mathrm{S_F}$, centered at $\mathbf{P}_{\mathrm{r}}$, is given as following assuming $h_{\mathrm{t}} = h_{\mathrm{r}}$

$$\mathbf{E}_{\mathrm{r}}(\mathrm{O}) = \sum_{\Delta\mathrm{S}\cap\mathrm{S_F}} \mathrm{R}(\mathbf{P}_{\mathrm{s}}) \cdot \mathbf{E}_{\mathrm{r}}(\Delta\mathrm{S}), \tag{2.110}$$

where R is a reflection coefficient, as defined in Section 2.3.3 through equation (2.57) , hence

$$\mathbf{E}_{\mathrm{r}}(\Delta\mathrm{S}) = \boldsymbol{e} \cdot \frac{e^{-jk(\mathrm{r_o}+\mathrm{s_o})}}{4\pi^2(\mathrm{r_o}\cdot\mathrm{s_o})} \cdot \Delta\mathrm{S}\cos\theta_{\mathrm{i}}. \tag{2.111}$$

Furthermore,

$\boldsymbol{e}$: unit vector in the direction of $\boldsymbol{E}$ field

k : wave propagation vector $(2\pi/\lambda)$

$\Delta\mathrm{S}$: elementary surface

θ_{i} : incident angle

$\mathrm{r_o}$: incident path length

$\mathrm{s_o}$: reflected path length

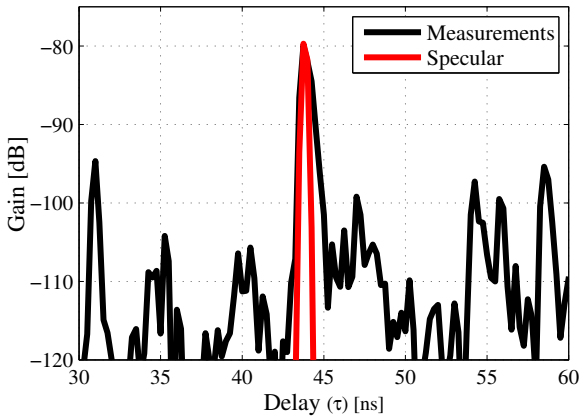

Figure 2.10. Measured and predicted ($R = 0.83$) specular peak from a scatterer.

where $\mathrm{r} = \|\mathbf{r}_{\mathrm{Pr}} - \mathbf{r}_{\mathrm{S}}\|$, $\mathrm{s} = \|\mathbf{r}_{\mathrm{O}} - \mathbf{r}_{\mathrm{Pr}}\|$, $\cos\theta_i = (\mathbf{r}_{\mathrm{o}} \cdot \mathbf{n})/\mathrm{r}_{\mathrm{o}}$, and $\|\cdot\|$ denotes the Euclidean norm of a vector. All paths lengths are normalized to the wavelength λ. The term $\mathbf{r}_{\mathrm{S}}$, $\mathbf{r}_{\mathrm{P_r}}$,$\mathbf{r}_{\mathrm{O}}$ corresponds to the position vectors between source $\mathbf{S}$, $\mathbf{P_r}$, $\mathbf{O}$, $\mathbf{I}$ and origin $\tilde{\mathbf{O}}$ of the Cartesian coordinate system, respectively. The detailed and exact expression of *interface Fresnel zone* according to the geometrical construction is presented in the Section 2.2.3 through equation (2.86). The approximate area of the first Fresnel reflection zone $\mathrm{S_F}$ normalized to the square of wavelength is given as,

$$\mathrm{S_F} = \pi \cdot \frac{\mathrm{r_o s_o}}{\mathrm{r_o} + \mathrm{s_o}} \cdot \frac{1}{\cos\theta_{\mathrm{i}}}. \tag{2.112}$$

Moreover, the summation in (2.110) can be interpreted as the sum of all contributions for which $\Delta\mathrm{S} \cap \mathrm{S_F}$ is valid and essentially refers to the surface $\sum \Delta\mathrm{S} \leq \mathrm{S_F}$ by construction. The numerical and experimental results demonstrate the accuracy of the proposed formulation, as illustrated in Figure 2.10.

2.3.3 Reflection and transmission losses for different objects in a radio environment at 70 GHz

Wireless backhaul connects the edge of a network to its core in a wireless manner and may become a feasible solution for 5G small cells densification at low interference mmWave frequency bands. Wireless backhaul links in typical deployment scenarios may get obstructed by various objects in the environment; hence, this interaction needs to be characterized. Furthermore, the mmWave spectrum is deemed necessary for high data-rate appli-

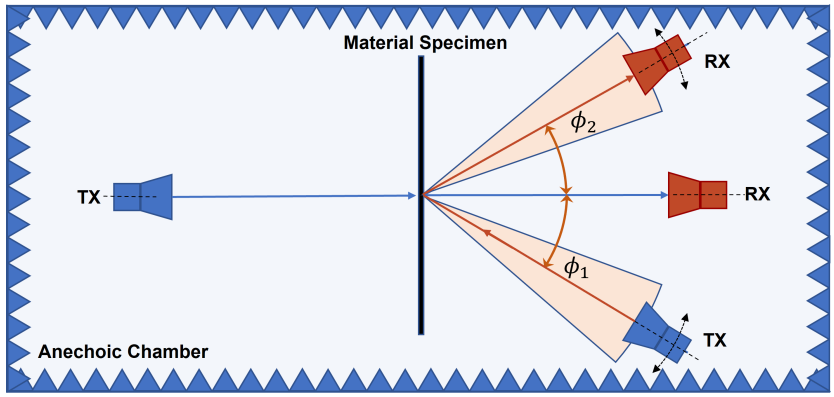

Figure 2.11. Transmission and bi-static reflection loss measurements layout in anechoic chamber.

cations and will be highly utilized in future generation networks; therefore, the interaction of mmWaves with different materials and associated losses must be thoroughly studied. [III] estimates reflection and transmission losses in obstructed-LOS (OLOS) and non-LOS (NLOS) conditions for various material objects in typical built-in and outdoor environments at the licensed $70\,\mathrm{GHz}$ band.

Reflection and transmission losses were estimated for various materials that were not previously measured at the $70\,\mathrm{GHz}$ band. These include energy-efficient building windows of different glass configurations, plywood, medium-density fiberboard (MDF), fabric, plasterboard, human body, asphalt, and common trees. The free space far-field reflection and transmission loss measurement setup in an anechoic chamber is illustrated in Figure 2.11, and measurements are depicted in Figure 2.12.

The experimental setup was based on a vector network analyzer (VNA) measuring the channel frequency response between TX and RX at the intermediate frequency (IF). The $70\,\mathrm{GHz}$ radio frequency (RF) signal was realized by mixing the IF and continuous-wave (CW) local oscillator (LO) signals with the help of frequency up- and down-converters. In transmission measurements, the material samples under study were illuminated at normal incidence, while for reflection measurements, the incident angle ϕ_1 is always kept equal to the reflection angle ϕ_2 for measuring the specular reflection only, as shown in Figure 2.11. It was ensured that the distance between the material sample, TX, and RX antennas is always greater than the Rayleigh distance, defined in the preceding Section 2.2.1. Furthermore, it was also ascertained that the size of a given material sample exceeds several Fresnel zones so that the link sufficiently covers

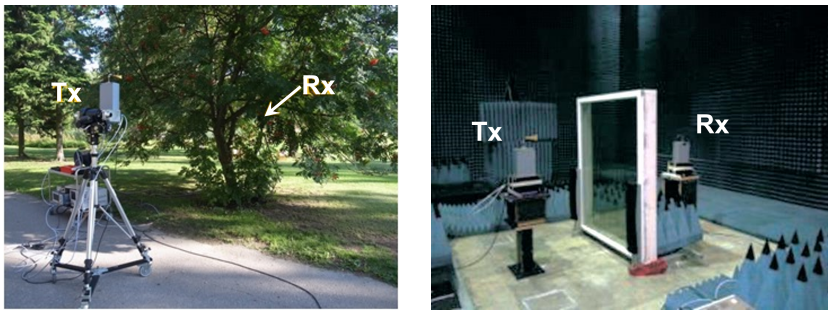

(a) (b)

Figure 2.12. Transmission and reflection loss measurements: (a) outdoor, and (b) anechoic chamber measurements.

the surface of the sample. The concept of Fresnel zones is discussed in Section 2.2.3. To calculate the losses, measured frequency responses were inverse-Fourier transformed and subjected to delay-gating to isolate the main specular reflection or transmission path between TX and RX from possible environmental reflections.

From the results, we can infer that energy-efficient building windows, plywood, human bodies, and trees offer significant attenuation $(10-48)\,\mathrm{dB}$ to mmWave signals in transmission mode. On the other hand, materials such as laminated plywood and metalized glass are highly reflective with low reflection losses (on average $\approx 5\,\mathrm{dB}$ over different incident angles) and may become helpful in establishing NLOS links. Different building windows specialized for heat rejection purposes, in which the inner surfaces of the glass panes are coated with metal, offer penetration loss between $37-70\,\mathrm{dB}$. Some window configurations offer on average $2\,\mathrm{dB}$ refection losses at different incident angles, while others offer as high as $15\,\mathrm{dB}$. We also see that human blockage loss is substantial for mmWave signals, i.e., $40\,\mathrm{dB}$ on average at $70\,\mathrm{GHz}$, which may result in sporadic link outages over time due to human activity. Other common building materials such as plasterboard, plywood, MDF, and fabric curtains have transmission losses in the range $1.5-8\,\mathrm{dB}$. Whereas, the reflection losses for these materials can be $15\,\mathrm{dB}$ on average, but are significantly reduced if the surface is laminated or painted.

2.3.4 On-site permittivity estimation at 60 GHz using point cloud of the environment

The cellular coverage is greatly influenced by the building and other material objects in radio environments, especially in cluttered urban envi-

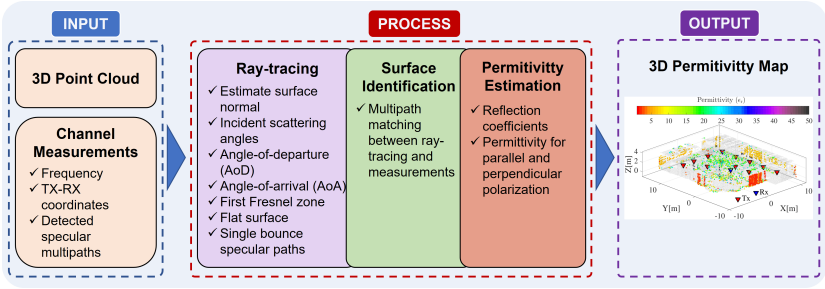

Figure 2.13. Flow diagram for generating a 3D permittivity map.

ronments. The deterministic coverage analyses based on raytracing or other numerical simulations require reasonably accurate knowledge of the RF properties of materials to maintain sufficient evaluation accuracy. For specular multipath, the surface reflection loss is calculated using the Fresnel reflection coefficient, discussed in Section 2.2.2 through equation (2.46) and (2.50), which involves the permittivity of the reflecting surface. The standard method of evaluating the permittivity of material samples is through isolated laboratory or anechoic chamber measurements. However, this has limited scope for estimating the permittivity of materials in built environments. On the contrary, reflection loss measurements can be performed *in situ* to determine the permittivity of each reflecting surface material. This approach can reasonably estimate the permittivity of built-in composite materials; withal, it is challenging and demanding to cover all surfaces in a given environment. To address this issue, [IV] proposes a novel technique for estimating the permittivity of composite materials in built environments. This is accomplished by measuring only a few TX-RX links in the desired radio environment, which is sufficient for estimating a large number of multipath. These multipath are then used for characterizing the permittivity of materials in a physical environment through the solution of the inverse reflection problem. The process involves three core steps for generating a 3D permittivity map of an environment, including (1) raytracing within the accurate 3D description of the environment in the form of a point cloud, (2) identification of reflecting surfaces, and finally (3) evaluating the corresponding permittivities. Figure 2.13 presents the flow diagram illustrating the process of creating a 3D permittivity map.

The raytracing generates multipath trajectories between TX, point cloud, and RX antenna, which are filtered based on Snell's law of reflection to isolate the specular reflections in the point cloud of the environment. Reflecting surfaces are subsequently identified by comparing the raytraced

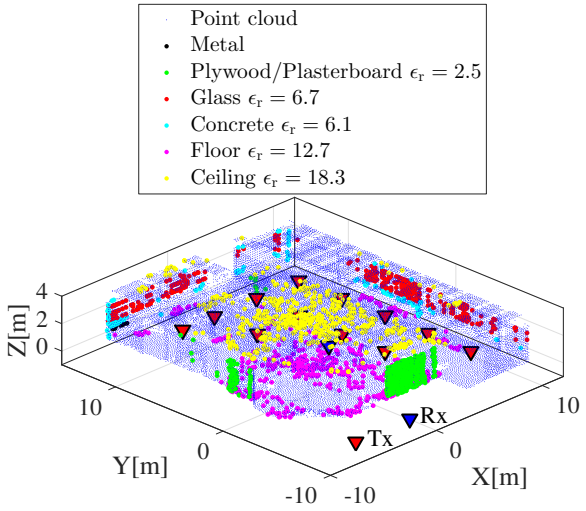

Figure 2.14. 3D permittivity map for a large indoor office environment.

specular paths on the point cloud with those available from the measurements of the same radio environment. A frequency-domain experimental setup was employed for radio channel measurements where the 60 GHz sounding signal was generated through a combination of VNA, LO, and frequency up- and down-converters. The specular paths are obtained by subjecting the measured channel responses to a multidimensional multipath detection algorithm. Finally, the permittivity is estimated for corresponding reflecting surfaces by solving the inverse problem on Fresnel reflection coefficients. The reflecting surfaces are classified into constituent materials by applying a heuristic clustering method to the point cloud based on the estimated permittivities and the values available in ITU-R P.2040-1 [66] for different materials. The identified surfaces are then visualized as a 3D permittivity map with mean permittivities representing different materials in different colors, as depicted in Figure 2.14. The proposed method successfully demonstrates that the permittivity of a large number of material objects in a radio environment can be characterized with a limited set of radio channel measurements without performing laborious *in situ* or anechoic chamber measurements.

The penetration depth of radio signals at 60 GHz is typically on the order of a few millimeters to a few centimeters depending on the material. This allows us to put less emphasis on the multilayered aspect of the built-in material structures. Therefore, the proposed method is valid at the higher frequencies where most of the materials exhibit low penetration of the radio signals. Furthermore, the large empty indoor office environment utilized

for this study constituted a small number of scatterers, offering a rather straightforward analysis. On the other hand, the proposed method may not work effectively at the lower frequencies and/or in cluttered environments as multiple reflections from the layered structure of the built-in materials and scattering due to the inhomogeneous materials are more profound.

As future work, we may consider performing raytracing simulations that employ on-site permittivity estimation values for the same environment. This would further demonstrate the suitability of the proposed method. In this study, the permittivity of materials estimated on-site at $60\,\mathrm{GHz}$ band through the proposed method for a large indoor office environment are well aligned with the generic values available in the ITU-R P.2040-1 [66], therefore, we are expected to see a good agreement between the simulated radio channels employing the two sets of permittivity values. On the contrary, we may also speculate that if for some radio environments, the estimated permittivity values of the materials are significantly different from the generic permittivity values available in the literature, a comparison of the simulated channels using the two sets of permittivity values will be conspicuously divergent from each other. Hence, it would indicate that the radio channel prediction based on generic permittivity values may not have sufficient accuracy against the measured radio channel.

2.3.5 Human blockage loss at mmWave frequencies

Humans are potential blockers of mmWaves between access points and mobile stations, prompting temporal variations in the radio channels. Radio channels can be modeled to accommodate human blockage effects using the geometrical description of TX-RX links, including wave scatterers and human bodies.

Most of the human blockage models available in the literature are eloquent and determine the human blockage loss based on body shape, dimension, and tissue material. These models are reasonably accurate with a trade-off between their computational complexity and accuracy; however, they lack a thorough measurements-based validation for different frequencies, body sizes and orientations, and antenna height dependence. [V] presents a comprehensive quantitative comparison of various human blockage models available in the literature and proposes a novel and vigorous human blockage model, called double-truncated multiple Knife-edge (DTMKE), at mmWave frequencies. Theoretically, the DTMKE is based on the fundamental concept of diffraction from an absorbing screen follow-

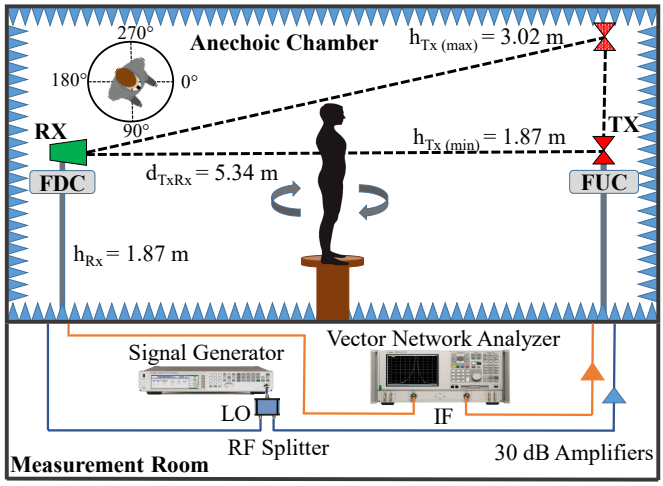

Figure 2.15. Experimental setup for human blockage measurements in anechoic chamber.

ing geometric theory of diffraction (GTD), as discussed thoroughly in the Section 2.2.4. The model is validated through anechoic chamber human blockage measurements at 15, 28, and 60 GHz by employing 15 human subjects of different sizes and weights at each frequency band.

The human blockage is influenced by the geometrical description of the TX-RX link with a human body and its tissue contents since diffraction at mmWaves around it is the primary propagation mechanism. The human blockage measurements constituted a frequency domain measurement setup employing a VNA for recording the complex frequency response of the channel between the biconical TX antenna and sectoral horn RX antenna, with a human subject amidst the TX-RX link inside the anechoic chamber, as illustrated in Figure 2.15. The proposed DTMKE model is based on canonical Knife-edge diffraction from an absorbing screen but reproduces human blockage losses better than the existing models. DTMKE models human blockage loss as the contribution of diffracting paths from four sides of a rectangular absorbing screen. The field at the RX is calculated as

$$E_{\mathrm{DTMKE}} = E_i \sum_{i=1}^{N} \exp\left(-j2\pi f \frac{\Delta d_i}{c}\right), \tag{2.113}$$

where E_i refers to the diffracting field of the i-th edge of the absorbing screen with $1 \leq i \leq 4$, Δd is the path length difference between the diffraction and LOS path, and c is the speed of light in vacuum. E_i is calculated using UTD equation in (2.101).

Figure 2.16 exemplifies the human blockage loss for different body ori-

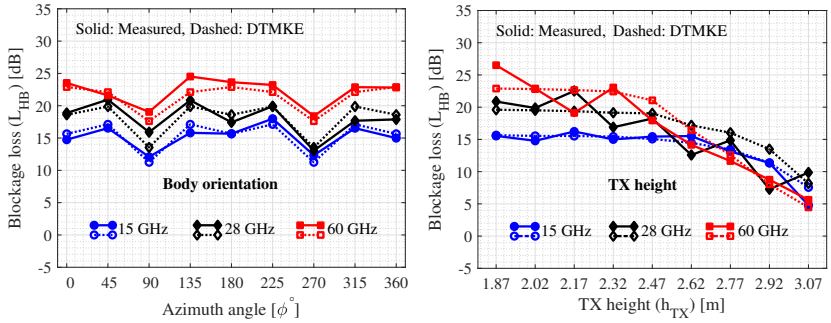

Figure 2.16. Comparison between measured and predicted median human blockage loss at 15, 28, and 60 GHz across 15 human subjects with respect to (a) body orientations and (b) TX antenna heights.

entations and TX antenna heights. It is observed that the human body's width, height, and thickness are the key parameters determining human blockage and must be incorporated into blockage models. The blockage loss increases with the increase in frequency regardless of the human body orientations and is on average $7-10\,\mathrm{dB}$ more at $60\,\mathrm{GHz}$ than at $15\,\mathrm{GHz}$. For different body orientations, the blockage loss is proportional to the cross-section of the human body with respect to the link. Furthermore, the human blockage loss decreases as the height of the transmitting antenna increases by $10\,\mathrm{dB}$ at $15\,\mathrm{GHz}$ and $20\,\mathrm{dB}$ at $60\,\mathrm{GHz}$ between the transmitter height difference of $1.24\,\mathrm{m}$. The marked decrease at $60\,\mathrm{GHz}$ is due to the clearance of the first Fresnel zone of the link when the TX antenna is elevated from base to the maximum height.

The proposed DTMKE model characterizes human blockage loss under the influence of shape, size, orientations of the body, and the height of the transmitting antenna. The results indicate that DTMKE provides better accuracy in predicting human blockage loss for different body orientations compared to the absorbing screen model. This implies that the DTMKE model can be effectively applied to the realistic and dynamic scenarios of channel simulations and models where relative geometries of antennas and wave scatterers are considered. Human bodies are defined on the same geometry and are constantly moving with random orientations. As future work, we may consider applying the DTMKE model to a dynamic scenario in raytracing simulations to demonstrate its efficacy.

3. Characterizing and Modeling Multipath Radio Channels

A radio channel links a transmitter (TX) to a receiver (RX), and the propagation of radio waves in it opens the door to our understanding of radio systems performance, including antenna implementation, TX power requirements, RX design, interference levels, and range of radio links. The TX signal arrives at the RX through many propagation paths undergoing different propagation mechanisms in the radio environment, such as free-space attenuation, transmission, reflection, diffraction, and scattering. These propagation effects have been described comprehensively in Section 2.2 of Chapter 2. Radio channel modeling is the art of delineating the propagation effects in a concise and efficient mathematical format. This mathematical framework is achieved through a detailed characterization of the radio channel using different evaluation metrics that are associated with its physical behavior. Furthermore, this also enables the development of meaningful knowledge to assist wireless system design. This chapter provides a theoretical overview of narrow and wideband radio channel characterization, emphasizing on the topics relevant to this thesis. Furthermore, it discusses different approaches to modeling radio channels and reviews various techniques for radio channel measurements.

3.1 Radio environments

Radio systems are developed to meet the specific requirements of intended users and thus differ in scope. Generally, the four primary goals associated with any radio system include coverage, mobility, capacity, and quality. A radio system must provide sufficient depth of coverage to its users and allow required flexibility concerning the allocation of resources, i.e., power and bandwidth. This allows the users to seamlessly move between different coverage sectors and maintain a certain level of service continuity for the

required quality of service (QoS). Similarly, a radio system must have the capacity to accommodate the growing number of users within the assigned frequency spectrum without affecting the quality to avoid user disruption. Radio environments can be defined based on operating radio systems; hence, in the following, several types of radio systems are defined.

Satellite systems
These types of links, operating in super-high (SHF: $3-30\,\mathrm{GHz}$) and extra-high (EHF: $30-300\,\mathrm{GHz}$) frequency bands, are established between geo-stationary earth satellites and fixed earth stations with large dish type antennas. The propagation typically occurs in the earth's atmosphere and is influenced by weather conditions, such as snow and rain.

Terrestrial systems
These are point-to-point fixed links operating in the frequency range of $0.45-100\,\mathrm{GHz}$. The main utilization of fixed terrestrial links is to support the cellular systems infrastructure with high data rate pipes for wireless backhaul and access networks. Atmospheric effects, building structures, and trees could significantly impact these links.

Megacells
These types of wireless systems are aimed at supporting critical communication services and are provided by low earth orbit (LEO) satellite systems to mobile users in a wide geographical area spanning hundreds of square kilometers. Global Positioning System (GPS) operating in *L* band is one such system that provides positioning, navigation, and timing services. The propagation is mainly influenced by the objects in the user's vicinity, while atmospheric effects are more profound at high frequencies. The common operating frequency bands include *L* ($1-2\,\mathrm{GHz}$), *S* ($2-4\,\mathrm{GHz}$), *K* ($18-26\,\mathrm{GHz}$), and *Ka* ($26-40\,\mathrm{GHz}$) bands.

Macrocells
These mainly provide cellular voice and data services to users in outdoors, rural, urban and suburban environments with medium mobile traffic densities. The links operate in very-high frequency (VHF) ($30-300\,\mathrm{MHz}$) and ultra-high frequency (UHF)($0.3-3\,\mathrm{GHz}$) range. Base stations service the cell coverage with high antennas to extend the range from $1\,\mathrm{km}$ to tens of kilometers—surrounding buildings and terrain influence the propagation of radio waves.

Microcells

These serve the high-density cellular traffic of users in urban and suburban areas outdoors and indoors. The base station antennas are mounted lower than street buildings' level height; hence, the coverage area is restricted to streets with a range length of about $500\,\mathrm{m}$. The building infrastructure and objects in the environment strongly influence the propagation. The microcell links also operate in VHF and UHF bands.

Picocells

Picocells typically deal with the dense user traffic and high data rate applications in indoor environments. The size of the environment determines coverage area and range. The propagation is greatly affected by furniture, humans, and other typical indoor objects.

Train, airplanes, and vehicles

Vehicle-to-infrastructure (V2I) and vehicle-to-vehicle (V2V) wireless communication have drawn much attention lately. Wireless connectivity for high data rate applications in trains, airplanes, and vehicles has seen an increased demand in recent years. The radio channels associated with such systems have high Doppler shifts and suffer non-stationarity since the relative environments are switched quickly at very high speed, from railway stations to urban and suburban environments, to bridges and tunnels, etc. Furthermore, the low latency of the wireless systems operating in such high mobility scenarios will be a crucial enabler for self or assisted-driving vehicles.

Outdoor-to-indoor

In modern architecture, radio systems are required to provide coherent connectivity with users constantly moving in and out of buildings. Reasonable prediction of the signals' penetration loss into building structures not only provides an estimation of the coverage extended into the buildings but also provides the evaluation of interference between radio systems operating in the vicinity.

3.2 Radio channel sounding

A radio channel may function in three dimensions, i.e., time, frequency, and space. The fundamental concept in characterizing and modeling radio channels is to evaluate their dependencies on these three dimensions as

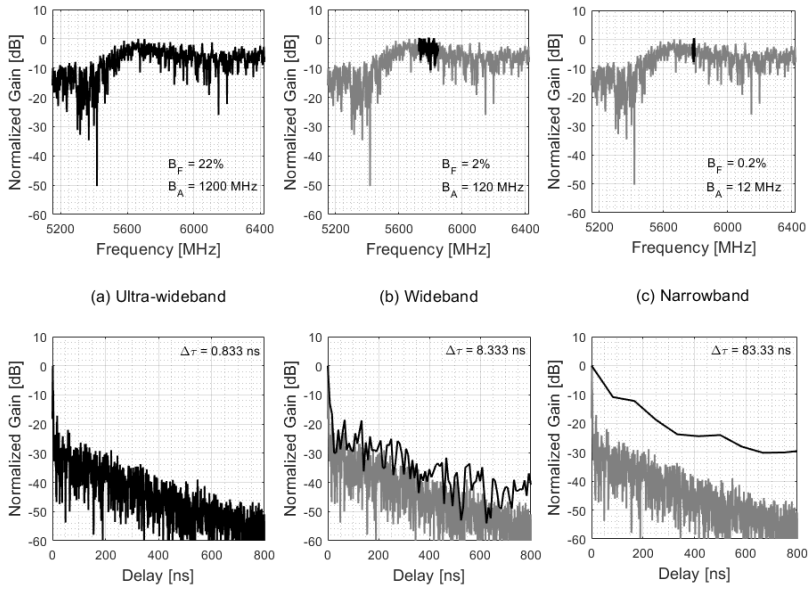

Figure 3.1. Frequency and time domain comparison between (a) ultra-wideband (b) wideband, and (c) narrowband channels.

coherent (constant) or *selective* (varying). Radio channels are typically characterized and modeled based on system bandwidth B, which determines delay resolution $\Delta\tau = 1/B$ that provides the ability to differentiate multipath in time-domain. Intuitively, the multipath delay range can be divided into $N_{\Delta\tau}$ discrete delay bins whose size is equal to the $\Delta\tau$. Let us consider two definitions of bandwidth to aid the classification of radio channels.

(a) *Absolute bandwidth* B_{A}: It is the difference between highest f_{H} and lowest f_{L} frequency in the band. i.e., $B_{\mathrm{A}} = \Delta f = f_{\mathrm{H}} - f_{\mathrm{L}}$.

(b) *Fractional bandwidth* B_{F}: It is the ratio of B_{A} and center frequency $f_{\mathrm{c}} = (f_{\mathrm{L}} + f_{\mathrm{H}})/2$ given in percentage as, $B_{\mathrm{F}}\% = \frac{B_{\mathrm{A}}}{f_{\mathrm{c}}} 100 = \frac{f_{\mathrm{H}} - f_{\mathrm{L}}}{f_{\mathrm{c}}} 100$.

Thus, the three main categories of radio channels are ultra-wideband, wideband and narrowband. Figure 3.1 illustrates the comparison of radio channels based on bandwidth in frequency and time domain. The ultra-wideband radio channels are characterized by their large relative bandwidth. The Federal Communications Commission (FCC) defines an ultra-wideband signal as " *the signal that occupies* $B_{\mathrm{A}} > 500\,\mathrm{MHz}$ *or* B_{F} *greater than* $20\,\%$ *of the* f_{c}". Ultra-wideband channels are not discussed further and are out of the scope of this thesis. On the other hand, wideband channels have $B_{\mathrm{F}} < 20\,\%$ of f_{c} while narrowband has a small B_{F}.

Measuring radio channels is a primary task in wireless communications because it enables us to dive deep into the propagation behavior of these radio channel. It is also popularly known as radio channel sounding, which originates from the notion that TX "sounds" or "excites" the radio channel with a specially designed signal, and RX receives the channel output. In a simple a mathematical way, the sounding signal $\hat{g}(t)$ is a set of periodically repeated pulses $p(t)$ with sampling interval T_{r}, as

$$\hat{g}(t) = \sum_{i=1}^{N_{\mathrm{p}}} p(t - iT_{\mathrm{r}}). \tag{3.1}$$

A channel model intended for a given radio environment, whether deterministic or statistical, is essentially based on measurements. More specifically, the parametrization of statistical channel models and validation of site-specific models require a reference to compare with, and radio channel measurements serve as the best reference.

The early channel sounders in the 1960s were required to measure field strength as it was the only metric of interest; however, their complexity has increased exorbitantly with the advancement of wireless systems and required channel models. The introduction of wideband wireless systems involved measuring channel impulse response, i.e., delay dispersion of the channel, and the research on multiple antenna systems instilled a high interest in directional channel properties. Until the 1990s, the channel measurements mainly focused on macrocells, but nowadays, there is a need to characterize a wide variety of scenarios at high delay resolution $\Delta\tau$.

3.2.1 Narrowband channel measurements

Narrowband channel measurements primarily aim at coverage analysis and evaluate large-scale channel effects from the received signal, such as pathloss and shadowing. In the past, a significant number of narrowband channel measurements were performed for radio coverage planning and deployment purposes [87–95]. In narrowband measurements, an unmodulated continuous-wave carrier or simply a *tone* with small B_{F} at the desired f_{c} is transmitted as a sounding signal from the TX and complex signal is captured at the RX. Practically, the sounding signal is generated from a signal generator, transmitted over the channel, and measured at the RX with a spectrum analyzer [96, 97]. This is a relatively simple sounder architecture with low instrumentation costs.

3.2.2 Wideband channel measurements

Wideband channel measurements are carried out either in delay- or frequency-domain where impulse response $h(t, \tau)$ is measured in the former and transfer function $H(f, t)$ is measured in the latter case, respectively. Delay-domain measurements acquire the channel's impulse response by exciting it with pulses or pseudo-noise sequences. On the other hand, frequency-domain measurements typically employ a chirp-like or some other multi-tone signal to sound the channel. The sounding signal should meet some requirements to enable high quality measurements [43], including:

(1) *Sufficiently large bandwidth* (B): The bandwidth is inversely proportional to the delay resolution. Hence, the greater the bandwidth of the sounding signal, the better the delay resolution.

(2) *Effective signal duration* T_{r}: In general, the TX power of wireless systems is always limited, and a sizeable time-bandwidth product $(T_{\mathrm{r}}B)$ enables the transmission of higher energy in the sounding signal to allow good signal-to-noise ratio (SNR) at the RX. It is desirable to keep the duration of the sounding signal T_{r} long enough to provide a large time-bandwidth $(T_{\mathrm{r}}B)$ product. However, T_{r} should not be more than the coherence time of the channel, i.e., the time for which the channel stays effectively constant.

(4) *Power spectral density*: In order to have similar quality of channel estimates at all frequencies, a uniform power spectral density $|P_{\mathrm{TX}}j\omega|^2$ is expected across the bandwidth of interest.

(5) *Low crest factor*: The crest factor refers to the sounding signal's peak-to-root mean square (rms) ratio. Efficient use of transmit power is possible with a low crest factor in the sounding signal because a high crest factor may drive power amplifiers toward a nonlinear operation. A rough initial estimate for the crest factor can be $1 < P_{\mathrm{CF}} \leq \sqrt{T_{\mathrm{r}}B}$ [98].

(6) *Correlation properties*: The sounding signals for the channel sounders with correlation-based architecture should have good properties of the ACF, such as a high power-to-off peak ratio and a zero mean.

We can measure a band-limited time-invariant channel as long as it is sampled at the Nyquist rate in the delay domain. However, additional conditions are required for time-variant channels. The most crucial is the

duration T_r of the sounding signal, which must be shorter than the coherence time of the channel, i.e., the channel does not vary over measurement duration. This predicates that the sampling frequency f_r must satisfy the following,

$$T_\mathrm{r} = \frac{1}{f_\mathrm{r}} \leq \frac{1}{2f_\mathrm{Dmax}}, \tag{3.2}$$

where $f_\mathrm{Dmax} = f_\mathrm{c} v_\mathrm{max}/c$ is the maximum Doppler frequency related to the maximum speed v_max of RX in downlink (TX to RX) channel, with f_c as the center frequency and c as the speed of light. Rearranging (3.2) allows us to evaluate the upper bound of the sampling distance for moving RX antenna during measurements as

$$\Delta x_\mathrm{s} \leq \frac{v}{f_\mathrm{Dmax}} \frac{\lambda_\mathrm{c}}{2} \leq \frac{\lambda_\mathrm{c}}{2}. \tag{3.3}$$

The upper bound expression in (3.3) reveals that at least two samples per wavelength are needed to avoid the aliasing effect.

Secondly, highly time-variant radio channels may become challenging with respect to the design of sounding signals as impulse responses from different sounding pulses may overlap. In order to avoid this overlapping, the delay dispersion of the channel must be taken into account. This means that T_r must be greater than the maximum excess delay τ_max of the channel, which is the difference between the first and last arriving multipath. However, this may contradict with the sampling frequency condition according to (3.2). This issue can be addressed if $2 f_\mathrm{Dmax} \tau_\mathrm{max} \leq 1$ is fulfilled, and such radio channels are said to be *underspread*. Most wireless channels are underspread, suggesting that the channel is slowly time-varying.

Another crucial aspect to consider while conducting channel sounding is the possible interference of other wireless systems operating in the same frequency band. In the presence of many interferers, the interference can be estimated as Gaussian noise, which can elevate the effective noise floor, thereby deteriorating the dynamic range.

Delay-domain measurements

In delay-domain measurements, the time-variant channel impulse response $h_\mathrm{meas}(t, \tau)$ is the convolution of the *actual* channel impulse response $h(t, \tau)$ and the impulse response of the channel sounder $\tilde{p}(\tau)$, i.e.,

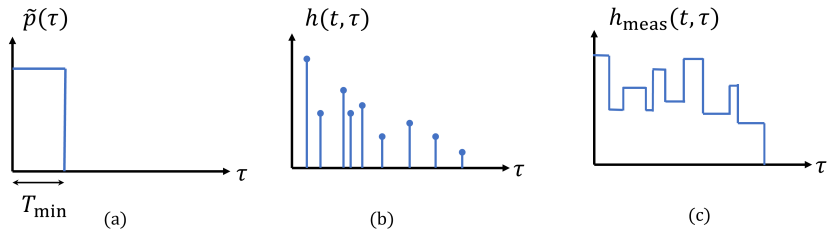

Figure 3.2. Impulse sounding: (a) TX pulse shape, (b) channel impulse response, and (c) measured impulse response at RX.

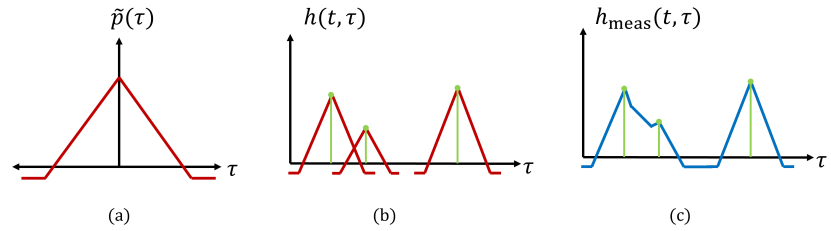

Figure 3.3. Correlative sounding: (a) correlation peak, (b) channel impulse response, and (c) measured impulse response at RX.

$$h_{\text{meas}}(t,\tau) = h(t,\tau) \circledast \tilde{p}(\tau), \tag{3.4}$$

where $\tilde{p}(\tau) = p_{\text{TX}}(\tau) \circledast p_{\text{RX}}(\tau)$, assuming linear channel and transceiver behavior. The term $p_{\text{TX}}(\tau)$ refers to the sounding TX pulse shape, $p_{\text{RX}}(\tau)$ is the RX filter response, and $(\circledast)$ is the convolution operator. Ideally, $\tilde{p}(\tau)$ should be as close to the Dirac delta function as possible to reduce the effect of the measurement system. This implies that the frequency spectrum should be flat over the given bandwidth. Otherwise, the process of deconvolving the undesired effects may lead to an increased effective noise level.

In *impulse* type of channel sounding, a burst of short pulses p_{TX} with high crest factor are transmitted. The short pulse time $T_{\min}$ and high pulse energy enable good spatial resolution and SNR. Figure 3.2 presents the idea where $h_{\text{meas}}(t,\tau)$ is measured at RX after the pulse is propagated through the radio channel. Generating high-energy pulses may become challenging as the required RF components are expensive or exhibit a non-linear behavior.

Correlative channel sounding is another type of time-domain sounding method that employs sounding pulses with high delay resolution but a low crest factor. The effective impulse response $\tilde{p}(\tau)$ of the sounder is the convolution of transmitted pulse shape p_{TX} and the impulse response p_{RX} of the RX filter. It determines the effect of the measurement system

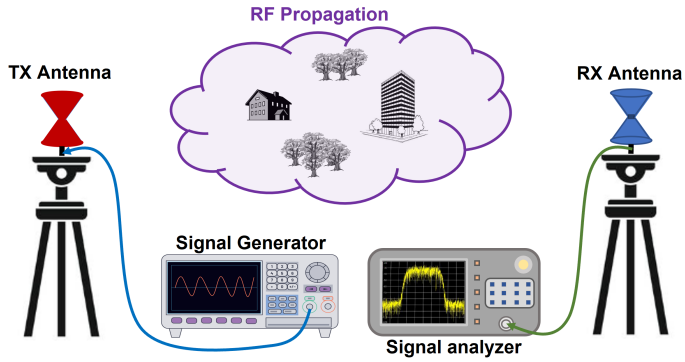

Figure 3.4. Delay-domain channel sounding using signal generator and signal analyzer.

on the measured impulse response, as illustrated in Figure 3.3. This allows additional room in designing the sounding signal since the SNR of the RX filter output is maximized if it is matched to the transmitted waveform [99]. The sounding signal's auto-correlation function (ACF) must be a good approximation of the delta function such that it has a high auto-correlation peak and low sidelobe levels (SLLs). The two types of sounding signals typically used in correlative channel sounding include periodic *Pseudo Noise* (PN) sequences [100–105] and multicarrier signals called *multisine* [106–108], where former is the most popular type. PN sequences are binary sequences that are statistically random, and a well-known variation of these used in Code Division Multiple Access (CDMA) systems are called Maximum-length PN sequences or simply *m-sequences*. These m-sequences can be generated using a linear feedback shift register. For time-variant channels, it is assumed that the channel remains constant for the duration of the PN sequence.

Figure 3.4 depicts a practical and straightforward delay domain measurement setup based on a signal or waveform generator transmitting the desired sounding signal through TX antenna and a signal analyzer capturing the received signal as *in-phase and quadrature* (Q) data through RX antenna.

Frequency-domain measurements

In contrast to the time-domain measurements where channel impulse response $h(t, \tau)$ is directly measured, the frequency-domain measurements estimate channel transfer function $H(t, f)$. However, the waveform or pulse shape is fundamentally different as the main design criteria are power spectral density $|P(j\omega)|^2$, which must be approximately constant over the desired frequency bandwidth. A frequency-domain transmit waveform

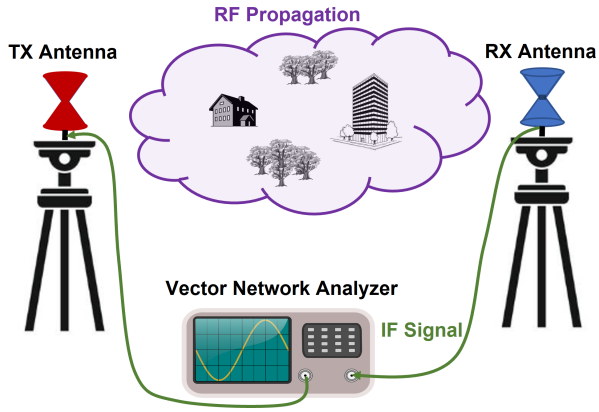

Figure 3.5. Frequency domain channel sounding with vector network analyzer (VNA).

based on chirping is given as [43]

$$p(t) = \exp\left[2\pi \mathrm{j}\left(f_\mathrm{c} t + \Delta f \frac{t^2}{2T_\mathrm{chirp}}\right)\right] \quad \forall \quad (0 \leq t \leq T_\mathrm{chirp}), \tag{3.5}$$

where f_c is the center frequency and Δf is the bandwidth. *Chirp* are linearly frequency-modulated signals. Thus, the instantaneous frequency is $f_c + \Delta f t / T_\mathrm{chirp}$, which changes linearly with time over the bandwidth. RX has a matched chirp filter that measures all frequencies in the given bandwidth at different time instants by sweeping through them.

An alternate method is to sound the channel with different frequencies simultaneously. This can be achieved by generating N_t sinusoidal signals or *tones* with different amplitudes a, phases ϕ, and frequency components and transmitting them from the TX antenna at the same time. Mathematically [43],

$$p(t) = \sum_{i=1}^{N_\mathrm{t}} a_i \exp\left[2\pi \mathrm{j} t \left(f_\mathrm{c} + i\frac{\Delta f}{N_t}\right) + \mathrm{j}\phi_i\right] \quad \forall \quad (0 \leq t \leq T_\mathrm{r}). \tag{3.6}$$

Generating analog $p(t)$ at multiple frequencies using different oscillators is challenging due to hardware costs and complex calibration. However, it is possible to generate digital $p(t)$ following the principles of Orthogonal Frequency Division Multiplexing (OFDM) [43].

A common way to perform frequency-domain channel measurements is through a vector network analyzer (VNA). This commercial off-the-shelf device measures the electrical network parameters of a device-under-test (DUT), such as scattering parameters or simply *S-parameters*. S-parameters describe the electric behavior of a linear electric network

[109]. For radio channel measurements, the forward complex scattering parameter $S_{21}(f)$ is of particular interest as it represents the channel transfer function $H(t, f)$. During the frequency sweep, the excitation signal is stepped through all the frequencies in the given bandwidth to obtain a discretized version of the complex channel transfer function $H(t, f)$. The time-domain channel impulse response $h(t, \tau)$ is obtained by subjecting $H(t, f)$ to inverse Fourier transform [110–112]. VNA is capable of wideband measurements with high dynamic range. A simple frequency-domain channel measurement based on VNA setup is illustrated in Figure 3.5.

Although VNA-based measurements are straightforward and accurate, there are also two notable disadvantages. First, measuring large bandwidths is usually time-consuming as the excitation signal steps through each frequency point during the sweep to acquire $H(t, f)$. This implies that the channel conditions must not change, and the environment remains static. Second, the TX-RX separation distance is limited because VNA transceiver is housed in the same casing and long RF cables are needed to extend the link range, which cause extra losses. Therefore, traditionally, VNA-based channel measurements have been restricted to indoor environments or short-range scenarios. However, in recent times, the RF is also extended by using RF-over-fiber solutions that have much smaller losses than RF cables. Since TX and RX in VNA share the same internal resources, such as local oscillators and timing circuits, VNA is highly accurate. Furthermore, VNA has well-defined and effective calibration procedures and uncertainty budget analyses. This makes VNA a great choice to serve as a reference for the other types of channel sounders.

For characterization of mmWave propagation, VNA-based or other channel sounder architectures utilize frequency up- and down-converters to achieve desired frequency range [VIII], [113–116]. Different radio channel sounder architectures for RF and mmWave are discussed in [43, 117].

Calibration

It is crucial to calibrate any channel sounder as a fundamental step to eliminate the influence of measurement setup from the measured data for its meaningful interpretation. The non-ideal characteristics of the measurement system include complex frequency response, complex antenna radiation patterns, attenuation, noise, and distortion.

In addition to some sophisticated procedures, the most candid calibration method of all is the back-to-back (B2B) calibration, which may be

applicable to all sorts of channel sounder architectures. Conducted B2B channel calibration tests are performed by connecting TX and RX through a calibrated attenuator. The actual measurements are then compensated for measurement artifacts by dividing the measured frequency response $Y_{\mathrm{meas}}(f)$ to the B2B frequency response $Y_{\mathrm{B2B}}(f)$, which is given as

$$Y_{\mathrm{B2B}}(f) = X(f) \cdot H_{\mathrm{TX}}(f) \cdot H_{\mathrm{B2B}}(f) \cdot H_{\mathrm{RX}}(f), \tag{3.7}$$

where $X(f)$ is input signal response, H_{B2B} is the attenuator and cables response, and $H_{\mathrm{TX}}(f)$ and $H_{\mathrm{RX}}(f)$ are the TX and RX responses, respectively. The calibrated response $\hat{Y}(f)$ is thus given as

$$\hat{Y}(f) = \frac{Y_{\mathrm{meas}}(f)}{Y_{\mathrm{B2B}}(f)} = \frac{X(f) \cdot H_{\mathrm{TX}}(f) \cdot H_{\mathrm{meas}}(f) \cdot H_{\mathrm{RX}}(f)}{X(f) \cdot H_{\mathrm{TX}}(f) \cdot H_{\mathrm{B2B}}(f) \cdot H_{\mathrm{RX}}(f)}. \tag{3.8}$$

Note that the calibrated response $\hat{Y}(f)$ in (3.8) still includes the effect of TX and RX antennas. In order to remove antenna effects from the measured response $Y_{\mathrm{meas}}(f)$, an over-the-air (OTA) reference measurement $Y_{\mathrm{OTA}}(f)$ can be performed in an anechoic chamber environment. The calibrated response is then given as

$$\hat{Y}(f) = \frac{Y_{\mathrm{meas}}(f)}{Y_{\mathrm{OTA}}(f)}. \tag{3.9}$$

Timing synchronization

The synchronization of TX and RX is challenging for radio channel sounding, especially in a multipath and dynamic environment. Large distances may separate the TX and RX; therefore, synchronization is required in both time and frequency. For the absolute measurement time reference, the initial point of the TX signal must be synchronized with the RX. Furthermore, to avoid delay spread error and artificial Doppler, it is crucial to frequency synchronize TX and RX oscillators to minimize the time drift. In practice, synchronization is achieved by using the same local oscillator for the TX and RX, like the VNA, or different oscillators in TX and RX, disciplined by reference clocks such as a $10\,\mathrm{MHz}$ continuous wave. The former restricts the link range because the common local oscillators have to be delivered over the range through a cable, while the latter allows a more extended measurement range. Various synchronization methods of the local oscillators are typically used depending on the practical considerations.

(a) *Cable synchronization*: For short-distance ranges, especially indoors,

a reference clock from one of the local oscillators can be fed to another with either coaxial or fiber-optic cables.

(b) *Global Positioning System* (GPS): In outdoor environments, GPS-disciplined reference clocks allow synchronization of the local oscillators to synchronize both in time and frequency. Additionally, the location of TX and RX are also recorded. However, the downside includes the LOS condition requirement between GPS satellites and TX/RX, which may not be possible in densely cluttered environments.

Noise floor

The measurement system introduces additive noise in each measured $h(t,\tau)$ sample. The noise level at RX bounds the measurements' dynamic range and may result in unwanted bias in the subsequent analysis of the measured channels. The main sources of RX noise are low-noise amplifiers (LNA) and analog-to-digital converters. The effective noise level depends on pathloss, fading, antennas, and polarization mismatch between TX and RX antennas. Noise level estimation is important for each measurement when RX power varies significantly. A simple and effective way to estimate the noise floor P_{n} of $h(t,\tau)$ is to observe the mean and standard deviation of its tail after maximum detectable delay where the signal power completely vanishes. When P_{n} is available, the power-delay profile (PDP) can be constrained to $P_{\mathrm{n}}P_{\mathrm{th}}$ such that the power-delay samples in $h(t,\tau)$ falling below the relative power threshold values of P_{th} are excluded, given as

$$h(t,\tau) = \begin{cases} h(t,\tau) & |h(t,\tau)|^2 \leq P_{\mathrm{n}}P_{\mathrm{th}} \\ 0 & \text{otherwise} \end{cases}. \tag{3.10}$$

To improve SNR, $h(t,\tau)$ samples measured at different time instants are averaged, assuming that the channel remains constant during data acquisition and noise is statically independent for different measurement runs. Averaging Q impulse responses will result in $10\log_{10}(Q)\,\mathrm{dB}$ improvement in SNR.

Dynamic range

The instantaneous dynamic range of the system can be defined using the PDP and is the ratio of the power of the strongest multipath in the PDP relative to the power at the noise floor. Instantaneous bandwidth depends on the effective noise bandwidth of the RX. In VNA, intermediate frequency (IF) bandwidth is a key factor in the selectivity of the instrument. Reducing

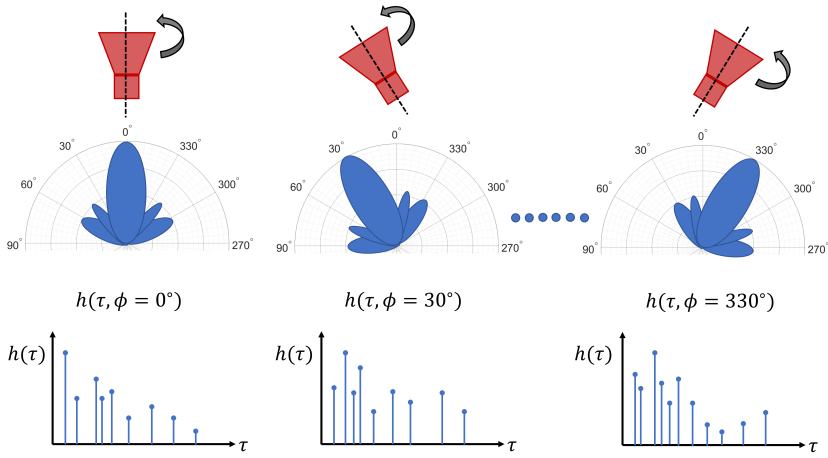

Figure 3.6. Directionally resolved measurements with highly directional antennas at one or both link ends.

the IF bandwidth increases the SNR and extends the dynamic range of measurements. For instance, decreasing IF bandwidth by a factor of 10 will nominally extend the dynamic range by $10\,\mathrm{dB}$; however, this will increases the measurement time substantially.

3.2.3 Directional channel measurements

Directional characterization of radio channels is imperative for the design of multi-antenna systems. The directional measurements do not require a completely different sounder architecture; instead, they are based on an ingenious combination of the possible setups discussed in the preceding sections and antennas. These measurements can be directionally resolved at one link end, i.e., either TX or RX enabling multiple-input single-output (MISO) or single-input multiple-output (SIMO), respectively, or at both link ends that can be generalized as MIMO. There are two approaches to implement directional measurements, which are briefly outlined below.

Rotating directional antennas

In this method, a highly directive antenna, for instance, a horn antenna, is mounted on an electromechanical rotator and connected to the RX of the channel sounder. Thus, the consolidated directional channel impulse response $h(t, \tau, \phi_i)$ is obtained by stepping through different pointing directions ϕ_i of the directive antenna, given as

$$h(t, \tau, \phi_i) = \int h(t, \tau, \phi) \tilde{G}_{\mathrm{RX}}(\phi - \phi_i)\, d\phi, \tag{3.11}$$

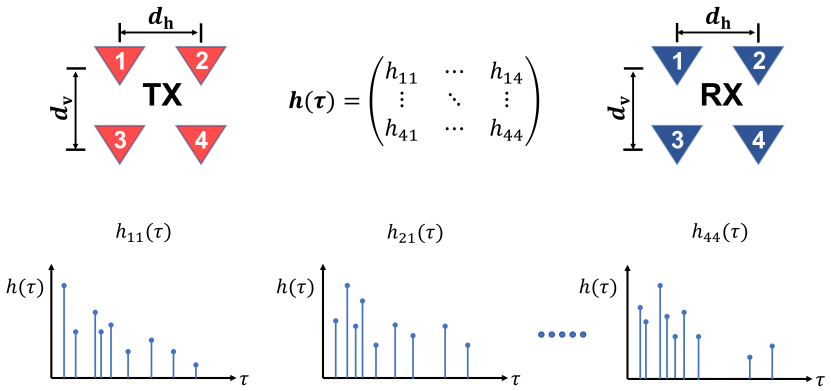

Figure 3.7. Spatially resolved measurements with virtual or real antenna arrays at one or both link ends.

where ϕ_i is the pointing direction of the main-lobe maximum of the antenna radiation pattern and $\tilde{G}_{\mathrm{RX}}$ is the radiation pattern of the TX and/or RX antenna. Figure 3.6 illustrates directionally resolved measurements. A prerequisite to this technique is that the radio channel is time-invariant for total measurement duration when RX antenna traverses all ϕ_i. Furthermore, a sophisticated and well-automated setup is required that ensures precise rotation of the antenna and coordination for acquiring the $h(t, \tau)$. It is noteworthy that in order to achieve better directional resolution, the measurement time increases proportionally.

Antenna arrays

This approach involves antenna arrays, which consist of several antenna elements with low directivity and inter-element spacing d on the order of wavelength. The channel impulse response is measured for each antenna element sequentially or simultaneously, depending on the choice of antenna array implementation. The consolidated channel impulse response is then obtained by subjecting the impulse responses vector of the antenna array elements to array signal processing techniques, such as beamforming or high-resolution subspace algorithms. Figure 3.7 presents an example of 4×4 MIMO measurement with 2×2 planar antenna arrays at both TX and RX sides. Three different antenna array implementation techniques are briefly introduced below.

(a) *Real arrays*: Each antenna element is connected to a dedicated modulator/demodulator chain in real arrays, and measurement of channel impulse response takes place simultaneously for all antenna elements. This antenna array implementation is high-cost and requires

proper design and complex calibration processes.

(b) *Multiplexed arrays*: In this type of array implementation, a single modulator/demodulator chain serves multiple antenna elements through a fast RF switch. The channel impulse response is thus measured for one antenna element and then switched to the next until all are measured. These arrays are best suited for dynamic environments as they provide a decent compromise between measurement speed and hardware complexity.

(c) *Virtual arrays*: This is an inexpensive method of realizing antenna arrays, where only a single element is moved through different antenna positions using an electromechanical scanner and measuring channel impulse response is measured at each antenna element. However, this necessitates that the measurement environment is static and does not change considerably during measurements. Furthermore, since measurements are done sequentially for each antenna element, the scanner movement may result in long measurement times. An apparent disadvantage of long measurement times can be the frequency drift and loss of TX/RX timing synchronization.

3.2.4 Validity of WSSUS

Concerning the validity of the *wide-sense stationary uncorrelated scattering* (WSSUS) assumptions to ensure stationarity in the measured radio channels, it is important to consider a few key factors: (1) the measurement duration should be long enough to capture the statistical variations of the channel while assuming stationarity over that duration. This means a sufficiently large number of channel realizations must be captured, (2) the measurements should have sufficient spatial coverage to capture potential small-scale variations in the channel characteristics, considering the propagation paths, scattering environment, and movement of the TX and RX, (3) the measurement locations should be randomized within the scenario of interest to capture the representative sample of the channel characteristics, and (4) warranting that antenna array aperture does not violate the WSSUS assumptions or if a directional antenna is rotated, the field observation area falls in the stationarity region. A more theoretical perspective on WSSUS assumptions is available in subsequent Section 3.4.4.

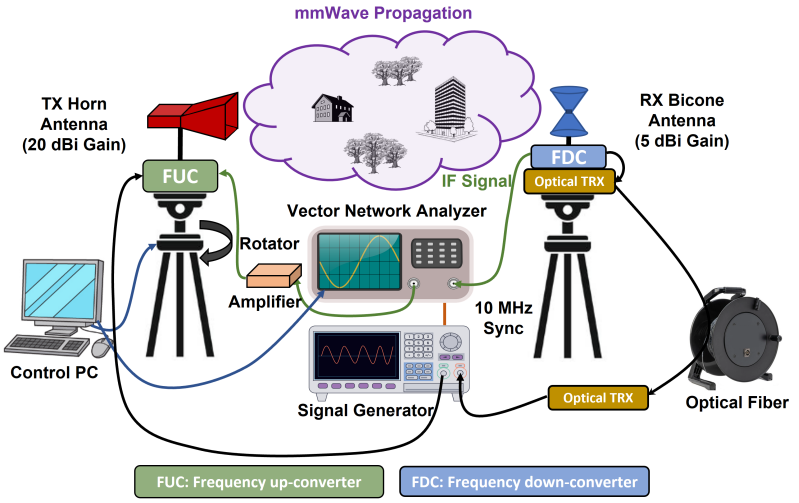

Figure 3.8. mmWave radio channel sounder at Aalto University.

3.2.5 Radio channel sounding at Aalto University

Department of Electronics and Nanoengineering at *Aalto University*, previously known as *Department of Radio Science and Engineering*, has a long history for radio channel sounding, characterization, and modeling at RF and mmWave frequencies. For this purpose, indigenously developed channel sounders have been extensively used [100, 103, 118–122]. The development of wireless communication systems obligates the characterization of radio channels for various scenarios. In the past several decades, many channel sounding campaigns have been undertaken that have become instrumental in understanding radio channels and developing suitable models for them. Extensive measurement campaigns covering various scenarios have been reported in white papers [123–125] under different projects. Indoor measurements are presented in [114, 115, 126–135], [VIII]. Outdoor urban micro and macro cellular measurements are reported in [96, 136–144], while vehicular related measurements are studied in [145–148].

The radio channel measurements performed under the scope of this thesis are based on frequency-domain channel sounding at RF and mmWave frequencies whose setup is outlined in Figure 3.8. The channel sounder employs VNA as the main data acquisition component allowing phase-synchronized measurements of scattering parameters for the device-under-test (DUT), which in this case is the radio channel. The VNA can measure large bandwidths; however, it is limited in practice and is subject to the

radio license. The link range can be extended through (1) optical fiber cable (OFC) replacing lossy coaxial cables and (2) high gain directive horn antenna at the RX for better dynamic range. Horn antennas for both vertical and horizontal polarization with similar radiation patterns are used to measure polarization effects.

Channel measurements at mmWave frequencies are realized by mixing the VNA, and local oscillator (LO) signals in frequency up- and down-converters. The frequency converters are harmonic mixers with internal frequency doublers. The phase of the LO signal is locked to the VNA using a $10\,\mathrm{MHz}$ reference signal. It is noteworthy that the VNA and LO output power is adjusted such that linear operation of the frequency up- and down-converters is ensured. For channel measurements at RF below $6\,\mathrm{GHz}$, the setup in Figure 3.8 is simplified by excluding LO since the available VNA operates in the required frequency range. Furthermore, directional measurements are achieved through a virtual array at one or both link ends, as described in Section 3.2.3.

In order to safeguard the validity of WSSUS assumptions, a sufficient number of channel realizations are captured during each channel measurement campaign for the statistical characterization of the radio channels. Furthermore, the horn antenna in the directionally-resolved measurements is rotated at least in a few small steps within the azimuth half-power beam width of the antenna so that the field observation area is small enough to fit within the stationarity region.

3.3 Characterizing narrowband radio channels

To expand our stratum of understanding for radio propagation channels, let us consider the power received at RX as a function of distance, as depicted in Figure 3.9. The received power varies about $80\,\mathrm{dB}$ over different spatial scales. The power variations on a small-distance scale comparable to a wavelength are called small-scale fading, which occurs due to the multipath interference. The variations in the power averaged over about 10 wavelengths and appearing on a large scale spanning a few hundred wavelengths is known as large-scale fading. These variations are caused by the shadowing of multipath by large objects. The monotonically decreasing large-scale mean over TX-RX separation is related to the spherical spreading of the radiated power from the antenna, called pathloss. Figure 3.10 illustrates different types of received power variations discussed above.

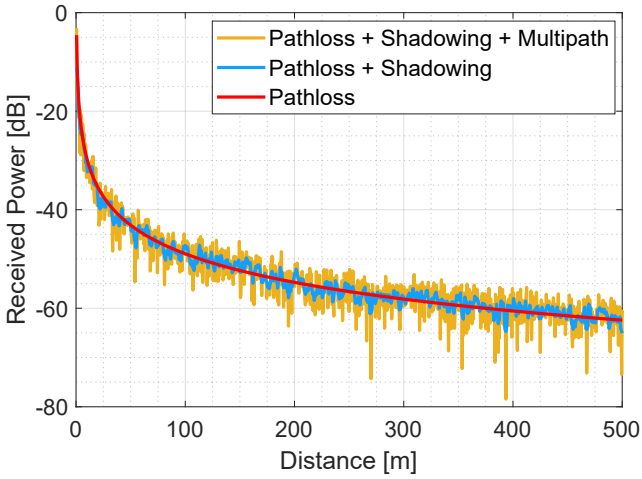

Figure 3.9. Received power as a function of distance, illustrating pathloss, small-scale and large scale variations.

Assuming unit TX power, the received power is directly proportional to the channel gain, and in this case, these terms can be used interchangeably. This section will focus on the statistical description of the channel gain for narrowband wireless systems; however, the discourse is equally applicable for unmodulated carrier signals, i.e., sinusoidal. The narrowband radio channel has an impulse response $h(t, \tau)$ with delta function and slow time-varying attenuation, as given by

$$h(t, \tau) = \alpha(t)\delta(\tau), \tag{3.12}$$

where $\delta(\tau)$ is the delta function with delay bin τ and amplitude $\alpha(t)$. From a time-domain perspective, in a narrowband wireless system, the inverse of signal bandwidth is greater than the delay of the longest multipath; thus, all the multipath falls into a single delay bin. In other words, the shape and duration of the transmitted and received signals are the same.

3.3.1 Pathloss

Pathloss models estimate the average attenuation between TX and RX separated through distance d by taking the spatial average over small-scale and large-scale fading. Small-scale and large-scale fading effects are elaborated on in the subsequent sections. Pathloss is modeled deterministically, and the simplest form of it is the free space path loss with pathloss exponent $n = 2$. Mathematically, it can be expressed as

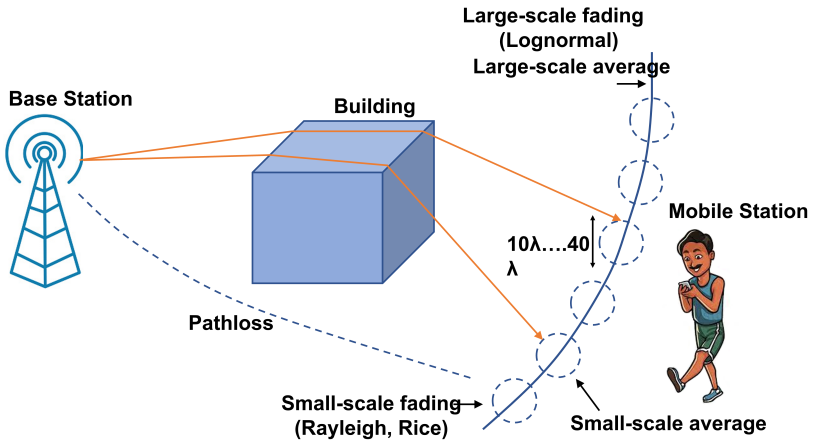

Figure 3.10. Pictorial illustration of the small-scale and large-scale effects causing fluctuations in the received signal power.

$$L_{\mathrm{r}}(d)_{\mathrm{dB}} = L_{\mathrm{r}}(d_{\mathrm{o}}) + 10n\log_{10}\left(\frac{d}{d_{\mathrm{o}}}\right), \tag{3.13}$$

where $L_{\mathrm{r}}(d)$ is the pathloss measured at a given distance, $L_{\mathrm{r}}(d_{\mathrm{o}})$ is the pathloss measured at the reference distance d_{o}, and n is the pathloss exponent which depends on the radio environment. Therefore, it is important to note that measurement setup may influence the estimation of pathloss exponent in terms of measurement range and distance sampling grid.

This implies that the measurement range should accommodate the local large-scale variations, i.e., shadowing, and could be challenging in small indoor environments where building structures set the range boundaries. A more common approach to estimate n is through regression analysis by minimizing the mean square error (MSE) between the measured and modeled pathloss samples as

$$\{\hat{n}, \hat{L_0}\}_{\mathrm{dB}} = \arg\min_{n,L_0} \sum_{k} (L_0 + 10n\log_{10} d_k - L_k)^2, \tag{3.14}$$

where L_k is the measured pathloss at distance d_k. For relatively small distances, this estimation method can be further improved by weighing the MSE with the logarithm of the distance-dependent weighting factor as

$$\{\hat{n}, \hat{L_0}\}_{\mathrm{dB}} = \arg\min_{n,L_{\mathrm{o}}} \sum_{k} (L_0 + 10n\log 10d_k - L_k)^2 \left(\log_{10}\frac{d_{k+1}}{d_k}\right). \tag{3.15}$$

More sophisticated pathloss models, such as, Okumura-Hata [149, 150], COST231-Walfish-Ikegami [151–153], Motley-Keenan [154] models also

consider other factor like building heights, measurement environment, etc.

3.3.2 Large-scale fading: Shadowing

Large-scale or *slow* fading is commonly known as shadowing, which refers to the random fluctuations in the received signal power when TX or RX is moved over relatively large distances, i.e., 10λ or more, and occur due to the shadowing of multipath by the interacting objects. These residual variations are the small-scale averaged power obtained after removing the distance-dependent decay effect from the received signal power. Typically, pathloss at a specific spatial location follows a lognormal (Gaussian) distribution about the mean as

$$L_{\mathrm{r}}(d)_{\mathrm{dB}} = L_{\mathrm{r}}(d_0) + 10n\log_{10}\left(\frac{d}{d_0}\right) + X, \tag{3.16}$$

where $X \sim \mathcal{N}(\mu,\, \sigma^2)$ is the shadowing loss in dB and σ^2 is its variance. The standard deviation σ of the shadowing distribution is also known as *location variability*, which depends on frequency, antenna heights, and the given environment, i.e., it is more for the suburban areas than the open areas [155]. The inverse of X is the shadowing gain ξ_σ. The probability density function (PDF) of the lognormal distribution is given as

$$\mathcal{F}_X(x) = \frac{1}{\sigma_Y\sqrt{2\pi}}\exp\left[-\frac{1}{2}\ln(x) - \mu_Y\right]^2, \tag{3.17}$$

where $\sigma_Y = \sqrt{\ln(\frac{\sigma_X}{\mu_X})^2 + 1}$ is the standard deviation and $\mu_Y = \ln(\mu_X) - \frac{1}{2}{\sigma_Y}^2$ is the expected value of the normal distribution variable $y = \ln(x)$.

To get the physical sense of shadowing, let us consider the situation depicted in Figure 3.10. Now, if the MS moves around the BS at a constant BS-MS separation, the predicted pathloss, according to (3.13), will also be constant. However, in reality, the amplitude of the received signal power changes noticeably since individual multipath may interact with different scatterers along their trajectory from BS to MS, causing variations in the received signal power relative to the nominal predicted pathloss. The lognormal variations of the small-scale averaged received power are typically attributed to the shadowing effects. Notably, this affects the amplitude of the multipath and is unrelated to their constructive or destructive interference effect. Assuming that the individual contribution to the attenuation of the signal along the propagation paths is independent, the total attenuation will be the product and sum of all contributions on

linear and decibel scales, respectively. This can be modeled as the sum of random variables on a decibel scale satisfying the central limit theorem, i.e., lognormal distribution. Note that this description, however, may not apply to all practical situations since all attenuation contributions are not equal [43, 155].

3.3.3 Small-scale fading

Small-scale fading is a process that makes the received signal strength fluctuate more rapidly due to multipath and can be encountered for small displacements of TX or RX comparable with one wavelength. The multipath propagation results in different copies of the transmitted signal, which arrive at RX from different directions and delays after interacting with scatterers in the environment. While the amplitudes of these multipath are constant for the region of the RX, their phases are strongly fluctuating. The addition of complex amplitudes results in significant variations in the summed magnitude. This is because in and out of phase multipath give rise to either constructive or destructive interference. Small-scale fading is sometimes also referred to as *fast* fading due to the relative motion (speed) of TX and/or RX and/or the objects in the propagation environment resulting in fast and significant channel variations even for a short duration. When objects in the propagation environment are stationary, and only TX or RX are subject to motion, the fading can be seen as a spatial phenomenon. However, RX perceives these spatial variations in the temporal domain; in the worst case, the signal may suffer a deep fade at a particular spatial location of the TX. When a relative motion exists between TX and RX, each multipath suffers from a frequency shift attributed to the Doppler shift and depends on the velocity and direction of TX and RX.

The amount of multipath in a radio channel is determined by the given radio environment, and cluttered environments tend to be rich in multipath. Several statistical distributions are used to characterize small-scale fading for narrowband systems, some of which are briefly discussed below.

Rayleigh distribution

Rayleigh distribution is the most frequently employed distribution to capture the small-scale signal variations in the signal envelope x in the absence of a LOS path. The PDF of Rayleigh distribution for a zero mean complex Gaussian signal is given as

$$\mathcal{F}(x) = \frac{x}{\sigma^2} \exp\left(-\frac{x^2}{2\sigma^2}\right), \tag{3.18}$$

where σ is the standard deviation of the received rms signal envelope, and σ^2 is the variance of the time-averaged received signal set according to the central limit theorem. The zero mean makes the distribution suitable for NLOS channel conditions. The popularity of Rayleigh distribution in wireless communications can be attributed to several reasons, including (1) good approximation for a large number of practical scenarios, (2) it conveniently describes the NLOS channel conditions where the dominant path is absent, and (3) it is mathematically tractable depending on a single parameter, i.e., the average received power.

Ricean distribution

When a small-scale fading signal envelope also contains a dominant and non-fading component, such as the LOS path, along with reflected, scattered, and diffracted paths, the envelope tends to follow the Ricean distribution. Ricean distribution approaches Rayleigh distribution when the dominant path is weak and insignificant. The PDF of the Ricean distribution is given as

$$\mathcal{F}(x) = \begin{cases} \dfrac{x}{\sigma^2} \exp\left(-\dfrac{x^2 + A^2}{2\sigma^2}\right) I_0\left(\dfrac{Ax}{\sigma^2}\right), & \forall\ (A \geq 0, x \geq 0) \\ 0. & \forall\ (x < 0) \end{cases} \tag{3.19}$$

where A is the amplitude of the LOS path and $I_0(\cdot)$ is the zeroth order Bessel function. To quantify the contribution of the LOS path, Ricean distribution specifies Ricean K-factor as

$$K = \frac{A^2}{2\sigma^2}, \tag{3.20}$$

and thus (3.19) can be rewritten as

$$\mathcal{F}(x) = \frac{2(K+1)x}{\Omega} \exp\left(-K - \frac{(K+1)x^2}{\Omega}\right) I_0\left(2x\sqrt{\frac{K(K+1)}{\Omega}}\right), \tag{3.21}$$

where $\Omega = E\{x^2\}$ is the mean power of the envelope. When no dominant path exist, $K = 0$ and the expression (3.21) reduces to Rayleigh PDF.

Nakagami distribution

Another widespread probability distribution used to describe the statistical nature of small-scale fading is Nakagami m-distribution. The PDF of the Nakagami distribution is given as

$$\mathcal{F}(x) = \frac{2m^m}{\hat{\gamma}(m)\Omega^m} x^{2m-1} \exp\left(-\frac{m}{\Omega}x^2\right), \qquad \forall\,(x > 0) \tag{3.22}$$

where $\hat{\gamma}(m)$ is the Euler's Gamma function. the shape factor $m \geq 1/2$, and the mean square amplitude $\Omega > 0$. The Nakagami equivalence to Ricean distribution and vice versa can be approximated for $m > 1$ as

$$m = \frac{(K+1)^2}{2K+1}, \tag{3.23}$$

and

$$K = \frac{\sqrt{m^2 - m}}{m - \sqrt{m^2 - m}}. \tag{3.24}$$

3.4 Characterizing wideband and directional radio channels

The practical wireless systems utilize large bandwidths to provide high data rates and enable multiple access and duplexing. Therefore, a multipath radio channel must also be characterized over a large bandwidth. However, the definition of wideband channels is restricted to the assumptions that multipath propagation effects (e.g., reflection, diffraction, penetrations) are constant over channel bandwidth, and relative or fractional bandwidth of the system (B_{F}) is smaller than $20\,\%$. The impact of multipath propagation on wideband wireless systems is interpreted in delay and frequency domains. In the delay-domain, the channel impulse response constitutes echoes of the same signal with different amplitudes arriving at different times referring to *delay dispersion*, which means the received signal has a longer duration than the transmitted signal. In the frequency-domain, the frequency response of the channel varies over the given bandwidth, which is known as *frequency selectivity* of the channel. In other words, both *delay dispersion* and *frequency selectivity* are dual. Furthermore, the wideband systems have two fundamental properties: (1) *inter-symbol interference* (ISI), an impairment caused by the interference of subsequently transmitted symbols, and (2) their ability to alleviate the adverse effects of fading since not all frequency components are attenu-

ated at the same level. The discrete-time channel impulse response of a wideband channel can be approximated by dividing it into $N_{\Delta\tau}$ delay-bins whose width is equal to the inverse of system bandwidth, i.e., $\Delta\tau = 1/B$. The amplitude of each delay-bin is obtained by computing the complex sum of all multipath falling in it, satisfying the central limit theorem. The amplitude of each delay-bin can be described statistically as *Rayleigh* or *Ricean* distribution following the mathematical principles described in the previous section.

The directional description of radio channels is useful on two accounts,i.e., (1) for achieving spatial diversity and multi-antenna systems and (2) de-embedding antenna effects from radio channels to obtain propagation channels. This necessitates a *double-directional* description of the channel impulse response.

3.4.1 The double-directional radio channel

The *double-directional* description of a radio channel provides angular information at both ends of the TX and RX link. Hence, there is a one-to-one correspondence between direction-of-departure (DOD), direction-of-arrival (DOA), and complex weights of a propagation path irrespective of the type and number of interactions associated with the surrounding environment. It also allows us to make a distinction between the *radio channel*, described by a non-directional channel impulse response including TX and RX antennas, and the *propagation channel*, described by the double-directional impulse response excluding the TX and RX antennas [48]. The concept of a double-directional radio channel is graphically illustrated through Figure 3.11. Under the assumption of ideal omnidirectional antennas, the channel impulse response constitutes the contribution of all multipath. Momentarily discounting the polarization, the time-invariant double-directional channel impulse response is given as

$$h(\tau, \Omega_{\mathrm{D}}, \Omega_{\mathrm{A}}) = \sum_{k=1}^{K} h_k(\tau, \Omega_{\mathrm{D}}, \Omega_{\mathrm{A}}), \tag{3.25}$$

where τ, Ω_{D}, and Ω_{A} refer to the path delay, DOD, and DOA, respectively. DOD and DOA can be understood as the spatial angles corresponding to a point on a unit sphere. K is the total number of multipath within the available dynamic range of the system. The time-variant channel impulse response of k-th multipath for plane waves without TX and RX location dependence is given as

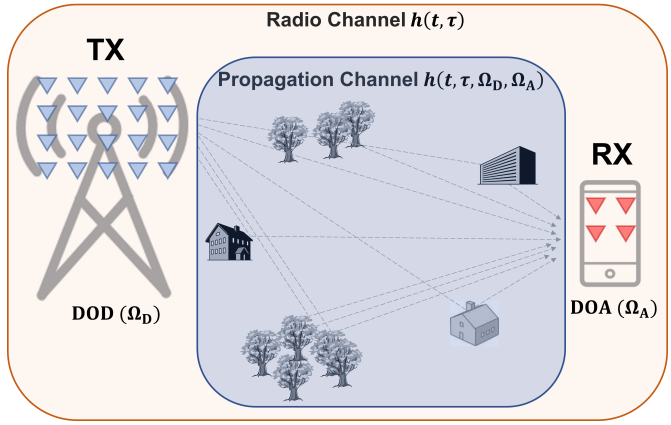

Figure 3.11. Difference between *radio channel* (non-directional) and *propagation channel* (double-directional).

$$h_k(t, \tau, \Omega_{\mathrm{D}}, \Omega_{\mathrm{A}}) = |a_k| e^{j\phi} \delta(\tau - \tau_k) \delta(\Omega_{\mathrm{D}} - \Omega_{\mathrm{D}k}) \delta(\Omega_{\mathrm{A}} - \Omega_{\mathrm{A}k}), \tag{3.26}$$

where $|a_k|$ is the magnitude, and $\Omega_{\mathrm{D}k}$ and $\Omega_{\mathrm{A}k}$ are the DOD and DOA of the k-th multipath. The parameters $(|a|, \Omega_{\mathrm{D}}, \Omega_{\mathrm{A}})$ vary slowly over wavelength, however, the phase ϕ vary rather quickly. The single-directional channel impulse $h(t, \tau, \Omega_{\mathrm{D}})$ can be obtained by integrating double-directional channel impulse response $h(t, \tau, \Omega_{\mathrm{D}}, \Omega_{\mathrm{A}})$ weighted by TX antenna pattern over DOD. While the radio channel impulse response (non-directional) $h(t, \tau)$ can be evaluated by integrating the single-directional impulse response $h(t, \tau, \Omega_{\mathrm{D}})$ weighted by RX antenna pattern over DOA.

Now extending the expression in (3.26) by introducing the complex polarimetric amplitude matrix $\mathbf{a}_{\mathrm{p}}$ describing the coupling between vertical (V) and horizontal (H) polarization, we get

$$\mathbf{H}_k(t, \tau, \Omega_{\mathrm{D}}, \Omega_{\mathrm{A}}) = \mathbf{a}_{\mathrm{p}} e^{j\phi} \delta(\tau - \tau_k) \delta(\Omega_{\mathrm{D}} - \Omega_{\mathrm{D}k}) \delta(\Omega_{\mathrm{A}} - \Omega_{\mathrm{A}k}), \tag{3.27}$$

where $\mathbf{a}_{\mathrm{p}} = \begin{pmatrix} a_k^{\mathrm{VV}} & a_k^{\mathrm{VH}} \\ a_k^{\mathrm{HV}} & a_k^{\mathrm{HH}} \end{pmatrix}$. It is noteworthy that V and H polarization representation is sufficient for characterizing the far-field. The $\mathbf{a}_{\mathrm{p}}$ accounts for the depolarization and reflectivity from the interacting objects or *scatterers* in the environment.

The directional description of a radio channel is beneficial for multi-antenna systems, such as MIMO. In this context, it is highly desirable to evaluate joint impulse responses at different antenna array elements,

thus generating a channel impulse response matrix. If the multi-antenna system represents a SIMO or MISO system, the joint impulse response is a vector. Denoting the TX and RX antenna array element coordinates as $\mathbf{r}_{\mathrm{TX}}^{(1)}, \mathbf{r}_{\mathrm{TX}}^{(2)}, ..., \mathbf{r}_{\mathrm{TX}}^{(N_\mathrm{t})}$, and $\mathbf{r}_{\mathrm{RX}}^{(1)}, \mathbf{r}_{\mathrm{RX}}^{(2)}, ..., \mathbf{r}_{\mathrm{RX}}^{(N_\mathrm{t})}$, respectively. The location dependent channel impulse response from j-th TX to i-th RX antenna element is

$$\begin{aligned}\mathbf{H}_{ij} &= \mathbf{H}_k(\mathbf{r}_{\mathrm{TX}}^{(j)}, \mathbf{r}_{\mathrm{RX}}^{(i)}) \\ &= \sum_{k=1}^{K} \mathbf{H}_k(\mathbf{r}_{\mathrm{TX}}^{(1)}, \mathbf{r}_{\mathrm{RX}}^{(1)}, \tau, \Omega_{\mathrm{D}k}, \Omega_{\mathrm{A}k}) \tilde{G}_{\mathrm{TX}}(\Omega_{\mathrm{D}k}) \tilde{G}_{\mathrm{RX}}(\Omega_{\mathrm{A}k}) \\ &\quad \exp(j\langle \hat{\mathbf{k}}(\Omega_{\mathrm{D}k}), (\mathbf{r}_{\mathrm{TX}}^{(j)} - \mathbf{r}_{\mathrm{TX}}^{(1)})\rangle) \exp(-j\langle \hat{\mathbf{k}}(\Omega_{\mathrm{A}k}), (\mathbf{r}_{\mathrm{RX}}^{(i)} - \mathbf{r}_{\mathrm{RX}}^{(1)})\rangle),\end{aligned} \tag{3.28}$$

where $\tilde{G}_{\mathrm{TX}}$ and $\tilde{G}_{\mathrm{RX}}$ are the complex radiation patterns of TX and RX antennas, respectively, $\hat{\mathbf{k}}$ is the unit wave vector in the direction of k-th DOD or DOA, and $\langle\cdot\rangle$ refers to the dot product. The explicit expression in (3.28) explains that the contribution from k-th multipath at location $\mathbf{r}_{\mathrm{TX}}^{(j)}$ is related to the impulse response at the reference antenna at location $\mathbf{r}_{\mathrm{TX}}^{(1)}$ by a phase shift.

3.4.2 Deterministic description of wideband radio channels

In the preceding discourse, we have established that time-variant impulse response $h(t, \tau)$ is the basic *input delay spreading* function for characterizing a wideband radio channel, which depends on variables time t and delay τ. Taking the Fourier transform of $h(t, \tau)$ with respect to either or both of these variables results in four equivalent representations, which are Fourier transform pairs and popularly known as *Bello functions*. According to the system-theoretic perspective, the simple input-output relationship of the system is

$$y(t) = x(t) * h(t, \tau) = \int_{-\infty}^{\infty} x(t - \tau) h(t, \tau)\, d\tau, \tag{3.29}$$

where $y(t)$ is the received signal at time instant t, which is evaluated by convolving the transmitted signal $x(t)$ with the time-variant impulse response of the channel $h(t, \tau)$.

Intuitively, it is possible to consider the system's behavior as *Linear Time Invariant* (LTI) if the channel impulse response changes slowly with time such that its duration is smaller than the time over which the channel varies significantly. The variable t is then the *absolute* time

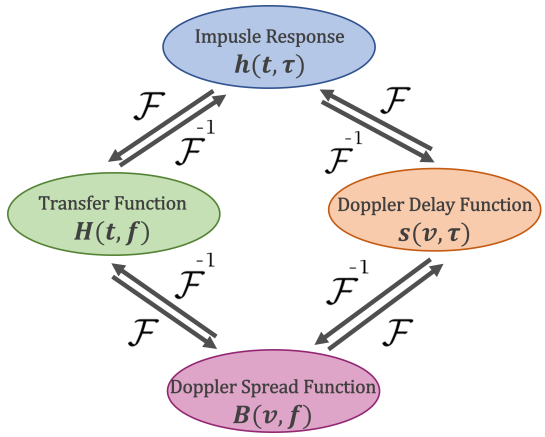

Figure 3.12. Relationship between deterministic *Bello functions*.

that parameterizes $h(\tau)$ and validates it in a large ensemble. The system can then be termed as *quasi-static*. Fourier transform of $h(t,\tau)$ with respect to τ is the time-variant *frequency transfer function*,

$$H(t,f) = \int_{-\infty}^{\infty} h(t,\tau) e^{-j2\pi f\tau}\, d\tau. \tag{3.30}$$

The Fourier transform of $h(t,\tau)$ with respect to t produces a Doppler-variant impulse response known as the *spreading function* $s(v,\tau)$ with a speed variable v. This function describes the spreading of the input signal in the Doppler and delay domains and is given as

$$s(v,\tau) = \int_{-\infty}^{\infty} h(t,\tau) e^{-j2\pi vt}\, dt. \tag{3.31}$$

The *spreading function* $s(v,\tau)$ can be Fourier transformed with respect to the variable τ, resulting in the Doppler-variant transfer function $B(v,f)$, given as

$$B(v,f) = \int_{-\infty}^{\infty} s(v,\tau) e^{-j2\pi ft}\, d\tau. \tag{3.32}$$

The relationship between *Bello functions* is summarized in Figure 3.12.

It is noteworthy that transformation between different*Bello functions*, illustrated in Figure 3.12, needs to be performed under proper conditioning of channel states. *Bello functions* intrinsically assume WSS, which if not satisfied, demands a due consideration of the higher-order moments of channel statistics and non-unique representation of the signals. *Bello functions* constitute a specific set of parameters that determine the window size and type, overlap, frequency bins, and scale selection among other

factors. Optimal values of these parameters are required for a meaningful transformation between different *Bello functions*. Furthermore, the transformation process involves non-linear operations that may cause distortion and artifacts in the transformed representation of the signals, affecting their quality and interpretability. Another aspect is the inherent trade-off between time and frequency resolution of the *Bello functions*. Thus, transforming between functions requires balancing and adapting the resolution characteristics to maintain the desired representation quality of the signal.

3.4.3 Statistical description of wideband radio channels

A full statistical description of wideband radio channels requires a multidimensional PDF of the time-variant channel impulse response, which is a joint PDF of the complex amplitudes at delay and time. In practice, this may be quite complicated to evaluate. A rather subtle approach would be to rely on the second-order description, typically known as *auto-correlation* function (ACF), describing the relationship between the second-order moments of the amplitude PDF of a signal at different time instants, and is given as following in time and frequency domains

$$R_{\mathrm{h}}(t, t', \tau, \tau') = E\{h^*(t, \tau)h(t', \tau')\}, \tag{3.33}$$

and

$$R_{\mathrm{H}}(t, t', f, f') = E\{H^*(t, f)H(t', f')\}. \tag{3.34}$$

It is noteworthy that equations (3.33) and (3.34) have four variables of the implicit 2D stochastic process. The ACF R_{yy} of the received signal $y(t)$ can be evaluated as a combination of ACF R_{xx} of the transmit signal $x(t)$ and the channel impulse response $h(t, \tau)$. This is because expectation over $x(t)$ and $h(t, \tau)$ can be taken independently. Thus,

$$R_{\mathrm{yy}}(t, t') = \int_{-\infty}^{\infty}\int_{-\infty}^{\infty} R_{\mathrm{xx}}(t - \tau, t' - \tau')R_{\mathrm{h}}(t, t', \tau, \tau')\, d\tau\, d\tau'. \tag{3.35}$$

3.4.4 The WSSUS assumption

The WSSUS model employs *wide-sense stationary* (WSS) and *uncorrelated scattering* (US) assumptions to provide a statistical description of short-

term variations in the channel. These are the assumptions about the physics of the channel that helps in simplifying the ACF in (3.33).

Mathematically, the WSS means that R_{h} depends only on the difference of variables $t - t'$, given as

$$R_{\mathrm{h}}(t, t', \tau, \tau') = R_{\mathrm{h}}(t, t + \Delta t, \tau, \tau') = R_{\mathrm{h}}(\Delta t, \tau, \tau'). \tag{3.36}$$

In a physical sense, WSS describes that the statistical properties of a channel do not vary over time. WSS must be satisfied for any given time; however, it is not practically possible since RX typically moves over large distances and mean power fluctuates due to shadowing and pathloss variations. This can be addressed by defining quasi-stationarity on a finite-time interval related to the distance covered by RX over which the channel statistics do not vary significantly. WSS also suggests that multipath with different Doppler shifts experience independent fading.

The US assumption means that the multipath contributions with different delay are uncorrelated. This condition is satisfied if the phase of one multipath is not related to the phase of another multipath with a different delay. When scatterers are spatially distributed randomly, phase variations of paths are uncorrelated even though RX is moved over small distances. The mathematical definition of refers that R_{H} does not depend on the absolute frequency but only on the frequency difference, as

$$R_{\mathrm{H}}(t, t', f, f + \Delta f) = R_{\mathrm{H}}(t, t', \Delta f). \tag{3.37}$$

Combining WSS and US under the WSSUS framework for analyzing radio channels with a better physical interpretation is now straightforward. ACF, under the WSSUS framework, must fulfill the following conditions.

$$R_{\mathrm{h}}(t, t + \Delta t, \tau, \tau') = P_{\mathrm{h}}(\Delta t, \tau)\delta(\tau - \tau'), \tag{3.38}$$

$$R_{\mathrm{H}}(t, t + \Delta t, f, f + \Delta f) = R_{\mathrm{H}}(\Delta t, \Delta f), \tag{3.39}$$

$$R_{\mathrm{s}}(v, v', \tau, \tau') = P_{\mathrm{s}}(v, \tau)\delta(v - v')\delta(\tau - \tau'), \tag{3.40}$$

$$R_{\mathrm{B}}(v, v', f, f + \Delta) = P_{\mathrm{B}}(v, \Delta f)\delta(v - v'), \tag{3.41}$$

where $P_{\mathrm{h}}(\Delta t, \tau)$ is the *delay cross power density*, $R_{\mathrm{H}}(t, t', \Delta f)$ is the *time*

frequency correlation function, $P_{\mathrm{s}}(v,\tau)$ is the *scattering function*, and $P_{\mathrm{B}}(v,\Delta f)$ is the *Doppler cross power density function*, as discussed in [43].

The *scattering function* $P_{\mathrm{s}}(v,\tau)$ may have a physical explanation, i.e., assuming single interaction, each differential element of the *scattering function* corresponds to the power of a path originating from a physical scatterer.

A generic WSSUS condition is possible by introducing the directional dependence in the ACF of channel impulse response given in (3.26). This means that the multipath arriving at the RX from different directions fade independently. The Doppler and multipath directions at the RX are linked where v and Ω_{A} are not independent variables anymore. The condensed description of a directional radio channel is thus given as

$$E[s^{*}(\Omega_{\mathrm{D}},\Omega_{\mathrm{A}},\tau,v)s(\Omega_{\mathrm{D}}^{'},\Omega_{\mathrm{A}}^{'},\tau^{'},v^{'})] = P_{\mathrm{s}}(\Omega_{\mathrm{D}},\Omega_{\mathrm{A}},\tau,v)\delta(\Omega_{\mathrm{D}}-\Omega_{\mathrm{D}}^{'})\delta(\Omega_{\mathrm{A}}-\Omega_{\mathrm{A}}^{'}) \\ \delta(\tau-\tau^{'})\delta(v-v^{'}). \tag{3.42}$$

3.4.5 Power-delay profile and its moments

A most straightforward representation of a wideband radio channel satisfying WSSUS is *Tapped Delay Line* (TDL) model as

$$h(t,\tau) = \sum_{k=1}^{N} a_k(t)\delta(\tau-\tau_k), \tag{3.43}$$

where δ function represents the discrete delay taps, N is the number of taps, $a_k(t)$ refers to the time-variant complex coefficients of the taps, and τ_k is the delay of the k-th tap. The change in tap complex coefficients over time is determined by the Doppler spectrum of the taps, which can be the same or different for the individual taps. $a_k(t)$ can be represented with a zero-mean complex Gaussian random process whose ACF can be obtained by their relevant Doppler spectrum. A physical interpretation of the TDL model represents the multipath propagation in the channel where N corresponds to a set of closely spaced multipath. The TDL model becomes purely deterministic when the arriving multipath are completely resolvable from the discrete scatterers in the environment. However, for practical systems, this depends on the bandwidth (resolution) of RX, limiting the number of resolvable multipath. For NLOS channel conditions, further simplifying the TDL model defined through equation (3.43) would restrict

the amplitudes of taps to Rayleigh fading. For LOS, a time-invariant component can be added without the loss of generality, as

$$h(t,\tau) = a_0\delta(\tau-\tau_0) + \sum_{k=1}^{N} a_k(t)\delta(\tau-\tau_k). \tag{3.44}$$

For wideband signals, the average received power as a function of delay is known as delay *power spectral density*, or popularly as *power-delay profile* (PDP), describing the power decay of multipath as the time delay elapses. PDP can be evaluated by taking the spatial average of magnitude squared channel impulse response $h(t,\tau)$ over multiple observations in a local area or time. It represents the mean power of multipath over delay τ and can be expressed as

$$\mathcal{P}(\tau) = E\left[|h(t,\tau)|^2\right] = \sum_{k=1}^{N} |a_k|^2\delta(\tau-\tau_k), \tag{3.45}$$

where $E[\cdot]$ is the ensemble denoting the statistical average over small-scale fading and is the sample average in the context of measurements. PDP is an essential characterization metric of the channel conditions in the delay domain. The shape of PDP depends on a given radio environment. The most common model describing PDP is known as the exponential decay model and is given as

$$\mathcal{P}(\tau) = \frac{1}{\gamma_d}\exp\left(-\frac{\tau}{\gamma_d}\right)U(\tau), \tag{3.46}$$

where γ_d is the delay decay factor and $U(\tau)$ is the Heaviside step function.

To attempt the statistical modeling of the multipath arrival times, the first-order approximation that the scatterers in the environment are randomly distributed in the space and the excess delays follow a *point Poisson process*. However, the measurement demonstrates that multipath arrives in groups called *clusters*. To characterize this behavior, *Saleh-Velenzuela* [156], $\Delta - K$ [157, 158], and 2-cluster [159] models were proposed.

Several sub-metrics can be derived from PDP, and these well-known normalized moments of PDP are briefly described below.

Excess delay

The discretized PDP has k taps identified by their corresponding delay τ_k and power P_k. Now the delay of any multipath with respect to the first arriving dominant component, typically the LOS path, is known as *Excess*

delay i.e., $\tau_{\mathrm{e},k} = \tau_k - \tau_0$.

Total or maximum excess delay

The difference of delay between the first dominant or LOS path to the last multipath is referred to as *total excess delay*, i.e., $\tau_{\max} = \tau_{\tilde{w}} - \tau_0$. Alternatively, it can also be defined as the time delay during which multipath energy falls to $\tilde{w}\,\mathrm{dB}$ below the maximum.

Mean delay

Also known as the normalized first-order moment of PDP, is the delay corresponding to the center of the PDP and is given as

$$\tau_{\mathrm{m}} = \frac{1}{P_{\mathrm{T}}} \sum_{k=1}^{N} P_k \tau_k, \tag{3.47}$$

where P_{T} is the total power in the radio propagation channel.

RMS delay spread

It is the normalized second-order central moment of PDP, and commonly called as *rms delay spread* defined by

$$\tau_{\mathrm{rms}} = \sqrt{\frac{1}{P_{\mathrm{T}}} \sum_{k=1}^{N} \left(P_k \tau_k^2 - \tau_m^2\right)}, \tag{3.48}$$

where P_{T} is the total power and τ_m is the mean delay.

τ_{rms} carries a special disposition among all other channel characterization metrics. It accounts for the relative power of the multipath and describes the delay dispersion in a given radio channel. It is not influenced by the absolute and mean delay of the paths since it's defined through the relative path delays only. From the system performance standpoint, it indicates the *bit error rate* (BER) of a wireless system. If τ_{rms} is smaller than the symbol duration, *inter-symbol interference* (ISI) can be avoided, and hence, the channel can be considered as *frequency flat*. The BER $\mathcal{P}_e$ can be related to the *rms delay spread* mathematically as

$$\mathcal{P}_e = K\left(\frac{\tau_{\mathrm{rms}}}{T_{\mathrm{B}}}\right), \tag{3.49}$$

where T_{B} is the bit duration and K represents the proportionality constant that depends on the modulation scheme, sampling time, shape of the PDP, and filtering at TX and RX. More detailed discussion on these factors affecting $\mathcal{P}_e$ is available in [43]. The typical value of τ_{rms} for indoor environments may range between $50 - 200\,\mathrm{ns}$ [43]. Further information

about delay spread characterization of various environments is available in [160].

An important parameter related to τ_{rms} is *coherence* bandwidth B_{c}, which refers to the range of frequencies over which the channel is considered as frequency flat, or alternatively, the bandwidth over which two frequencies of a signal have correlated amplitude fading. It is given as [161]

$$B_{\mathrm{c}} \geq \frac{1}{2\pi\tau_{\mathrm{rms}}}. \tag{3.50}$$

3.4.6 Power angular spectrum

Following the double-directional framework of channel impulse response presented in Section 3.4.1, the *delay power spectrum* is derived from (3.42) as

$$\mathcal{Q}_{\mathrm{DPS}}(\Omega, \Psi, \tau) = \int P_{\mathrm{s}}(\Omega, \Psi, \tau, v)\, dv. \tag{3.51}$$

Now, the *power angle-delay profile* (PADP) as observed from the TX antenna is given as

$$\mathcal{Q}_{\mathrm{PADP}}(\Omega, \tau) = \int \mathcal{Q}_{\mathrm{DPS}}(\Omega, \Psi, \tau) G_{\mathrm{TX}}(\Psi)\, d\Psi. \tag{3.52}$$

The *power angular spectrum* (PAS), or alternatively, *angular power spectrum* (APS) is the marginal integral of the $\mathcal{Q}_{\mathrm{PADP}}$ over the delay domain, and is given as

$$\mathcal{Q}_{\mathrm{PAS}}(\Omega) = \int \mathcal{Q}_{\mathrm{PADP}}(\Omega, \tau)\, d\tau, \tag{3.53}$$

where the integration of $\mathcal{Q}$ over Ω recovers the PDP.

The *angle spread* in azimuth or elevation is the second central moment of $\mathcal{Q}_{\mathrm{PAS}}(\Omega)$ if all multipath are incident on azimuth plane $\Omega = \phi$ or elevation plane $\Omega = \theta$, given as

$$\mathcal{S}_{\Omega} = \sqrt{\frac{\int |e^{j\Omega} - \mu_{\Omega}|^2 \mathcal{Q}_{\mathrm{PAS}}(\Omega)\, d\Omega}{\int \mathcal{Q}_{\mathrm{PAS}}(\Omega)\, d\Omega}}, \tag{3.54}$$

where

$$\mu_{\Omega} = \frac{\int e^{j\Omega} \mathcal{Q}_{\mathrm{PAS}}(\Omega)\, d\Omega}{\int \mathcal{Q}_{\mathrm{PAS}}(\Omega)\, d\Omega}, \tag{3.55}$$

is the mean departure angle.

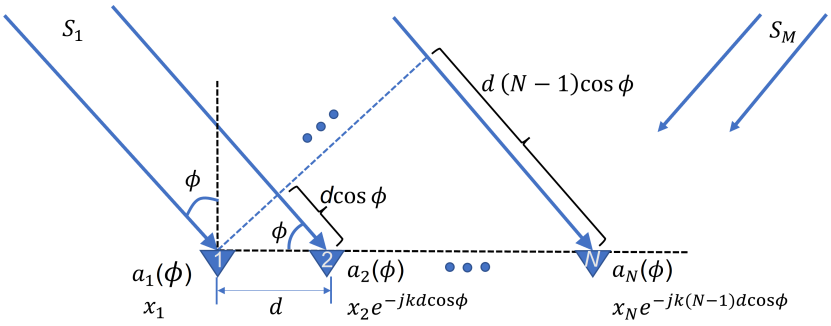

Figure 3.13. Plane wave incident on a uniform linear array (ULA).

Beamforming

The directional information can be extracted from the array measurements described in Section 3.2.3. Beamforming is a basic DOA estimation method, essentially a spatial filtering process of the data sampled at a given antenna array. An angular grid is formed corresponding to the array, and a beam created by it is steered in these discrete directions to sense the maximum array output determining the incoming signal direction. The performance of beamforming depends on array aperture size, i.e., the physical size of the array in wavelengths since the spatial discrimination improves as the aperture size increases [162, 163].

Let us first consider a simple mathematical model assuming a *Uniform Linear Array* (ULA) with total N array elements separated from each other with distance d along x-axis and the signal detected at the n-th array element is represented as $x_n(t)$. Each element of the array is represented as a point receiver in two-dimensional (2D) Cartesian coordinate system as $\mathbf{I}_n = (x_n, y_n)^T$. Now consider plane waves $s_m(t), m = 1, ..., M$ from M different directions are incident on the ULA, where each wave is described by its DOA ϕ. The response of n-th array element can be modeled as

$$x_n(t) = g_n(\phi) \exp\left[-jk(x_n \cos\phi + y_n \sin\phi)\right] s_m(t) + r_n(t), \tag{3.56}$$

where $g_n(\phi)$ is the directivity of the antenna element, $k = 2\pi/\lambda$ refers to as the wavenumber with wavelength λ and $r_n(t)$ is the additive noise.

The equation (3.56) requires the *narrowband assumption*, which means that the array aperture should be less than the inverse relative bandwidth, i.e., $1/B_{\mathrm{F}}$. Applying the superposition principle assuming a linear receiving system, for an N-dimensional array with M signals arriving from discrete directions ϕ_m, the vectored response is given as

$$\mathbf{x}(t) = \sum_{m=1}^{M} \mathbf{a}(\phi_m) s_m(t), \tag{3.57}$$

where $\mathbf{a}(\phi) = [g_0(\phi) \quad g_1(\phi)e^{-jkd\cos\phi} \quad .... \quad g_(n-1)(\phi)e^{-jk(N-1)d\cos\phi}]^T$ refers to the steering vector of the ULA. $\mathbf{A}(\phi) = [\mathbf{a}(\phi_1), \mathbf{a}(\phi_2), ..., \mathbf{a}(\phi_M)]$ corresponds to the $N \times M$ steering matrix. A more compact form of the output at the array is given as

$$\mathbf{x}(t) = \mathbf{A}(\phi)\mathbf{s}(t) + \mathbf{r}(t). \tag{3.58}$$

where $\mathbf{s}(t) = [s_1(t), s_2(t), ..., s_M(t)]^T$ represents the baseband signal waveforms. Finally, the array response steered as a linear combination of array outputs is

$$y(t) = \sum_{n=1}^{N} w_n^* x_n(t) = \mathbf{w}^H \mathbf{x}(t), \tag{3.59}$$

where w_n is the weight at the n-th array element, $(\cdot)^*$ and $(\cdot)^H$ represents the complex conjugate and conjugate transpose, respectively. Thus, the output power $P(\mathbf{w})$ of the array is

$$P(\mathbf{w}) = E[|y(t)|^2] = \mathbf{w}^H E[\mathbf{x}\mathbf{x}^H]\mathbf{w} = \mathbf{w}^H \hat{\mathbf{R}} \mathbf{w}, \tag{3.60}$$

where $E[.]$ denotes the expectation and $\hat{\mathbf{R}}$ is the spatial covariance matrix.

The most straightforward beamforming technique is *Bartlett* beamformer, which estimates the DOA by taking the Fourier transform of the signal vector $\mathbf{x}(t)$ with an angular resolution of $2\pi/N$ [43, 163, 164]. For given array geometry, this simple method maximizes the power of the beamforming output of a given steering angle. The power maximization is achieved as [163]

$$\max_{\mathbf{w}} \left\{ \mathbf{w}^H E[\mathbf{x}\mathbf{x}^H]\mathbf{w} \right\} = \max_{\mathbf{w}} \left\{ E[|s(t)|^2]\mathbf{w}^H |\mathbf{a}(\phi)|^2 + \sigma^2 |\mathbf{w}| \right\}, \tag{3.61}$$

where σ^2 is variance of the white noise with the constraint $|\mathbf{w}| = 1$ resulting in

$$\mathbf{w}_{\mathrm{BF}} = \frac{\mathbf{a}(\phi)}{\sqrt{\mathbf{a}(\phi)^H \mathbf{a}(\phi)}}. \tag{3.62}$$

Finally, the power angular spectrum (PAS) is given as

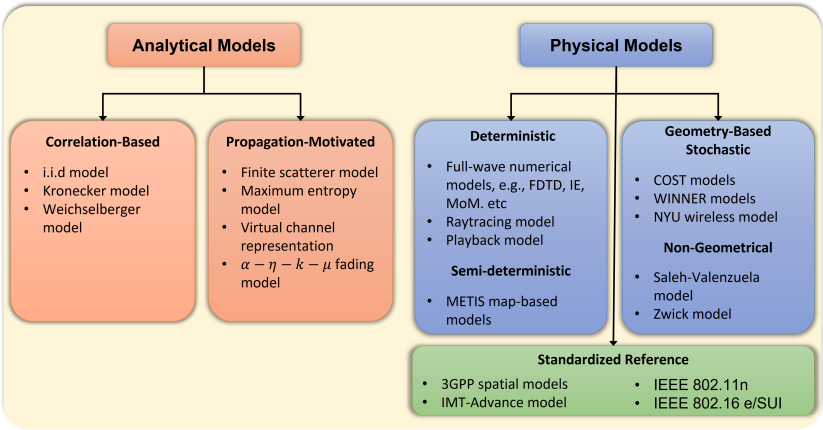

Figure 3.14. Classification of radio channel models [172, 173].

$$P_{\mathrm{BF}}(\phi) = \frac{\mathbf{a}(\phi)^H \hat{\mathbf{R}} \mathbf{a}(\phi)}{\mathbf{a}(\phi)^H \mathbf{a}(\phi)}. \tag{3.63}$$

Although the Bartlett beamformer is simple to implement, it provides low angular resolution. This problem can be addressed by using *high-resolution* algorithms, where the angular resolution is not restricted to the antenna array size but only by the modeling errors and noise. The cost comes in with high computational complexity. Some well-known high-resolution methods include ESPRIT [165], MUSIC [166, 167], Capon MVR [168], SAGE [169], and RIMAX [170, 171].

3.5 Radio channel modeling methods

Radio channel models are inevitable for designing, testing, planning, and deploying wireless systems. The preceding sections discuss the different properties of radio channels mathematically. This section briefly describes various approaches that translate these mathematical details into an objective framework, referred to as a *radio channel model*. Channel modeling can be accomplished differently depending on the requirements and complexity level. A detailed classification is available in [172] and illustrated through Figure 3.14. Channel models can be broadly categorized into *Analytical* and *Physical* models. The latter will be discussed more thoroughly as they fall under the scope of this thesis.

Analytical models aim at characterizing the impulse response or, equivalently, the channel transfer function between TX and RX antennas in an analytical manner without considering the physical wave propagation ef-

fects. These models are famous for synthesizing MIMO matrices for system and algorithm development and verification. For MIMO, the analytical models may be based on first and second-order channel statistics. The most common approach is the independent and identically distributed (i.i.d.) Rayleigh or canonical channel model. Thei.i.d. Rayleigh channel depends on a rich scattering environment assuming that the antenna elements are uncorrelated and statistically independent. It is used for the information-theoretic analysis of MIMO systems. In practice, MIMO channels include spatial correlation effects that can be modeled using approaches such as the Kronecker model [174] and the Weichselberger model [175]. Another category of analytical models is known as propagation-motivated models and are described thoroughly in [172, 173].

Physical models consider radio wave propagation effects through double-directional multipath propagation between TX and RX antennas. They explicitly characterize the multipath propagation parameters, such as complex amplitudes, delay, DOD, DOA, and polarization. Furthermore, these models are essentially and ideally independent of antenna properties and system bandwidth. Physical models are further divided into *deterministic* and *stochastic* channel models.

3.5.1 Deterministic modeling of radio channels

Deterministic radio channel models use the geographical description of the complete physical environment in the form of a computer-aided design (CAD) model and evaluate Maxwell's equations subject to the boundary conditions to determine the field strength in space and time. Since impulse responses are gathered at a specific geographical location, these models are sometimes referred to as *site-specific* models. However, this approach is much easier than costly and laborious measurement campaigns that require skilled human resources and sophisticated equipment. There are significant challenges associated with the deterministic modeling of radio channels including high computational effort, ample storage required for environment databases, inaccuracies in the geometrical databases, and approximation by the numerical methods. Deterministic methods are mainly used to plan and deploy cellular systems so that coverage can be tested for specific deployment options. Two profound categories of deterministic channel models include numerical techniques and ray-based methods.

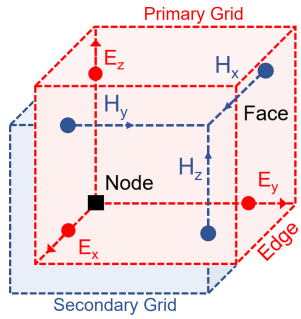

Figure 3.15. 3D Yee grid with **E** and **H** field vectors.

Numerical methods in electromagnetics

In recent times, there has been a concerted effort in electromagnetic research focusing on numerical and asymptotic techniques to solve boundary problems related to antennas and the propagation of electromagnetic waves. The incredible development in computer technology during the past two decades has triggered a profound interest in the numerical solution of many practical electromagnetic analysis and synthesis problems previously regarded as analytically intractable. The most exact deterministic channel modeling method is the *brute* force solution of Maxwell's equations through either integral or differential equations framework applied on the accurate geometrical description of the given environment. The integral equation technique is derived from the well-known *Methods of Moment* (MoM) [176] where a set of basis functions represents the unknown currents on the surface of scatterers. Differential equation approach include *Finite Element Method* (FEM) [177] or the more popular version, i.e., *Finite-difference time-domain* (FDTD) [178–180] method.

The FDTD is one of the popular full-wave numerical techniques for solving electromagnetic problems, mainly because it is straightforward from a conceptual and implementation point of view. It can successfully tackle electromagnetic problems, such as scattering from metal objects and dielectrics, antennas, microstrip circuits, and electromagnetic absorption in the human body exposed to radiation. FDTD is a grid-based numerical method that solves Maxwell's curl equations directly in the time-domain on a space grid called three-dimensional (3D) *Yee cell* illustrated in 3.15. The electric (**E**) and magnetic (**H**) fields are described as vectors in a 3D Cartesian coordinate space and allow us to consider material properties straightforwardly.

Time-dependent Maxwell's equations are discretized to space and time

partial derivatives based on central difference approximations. These finite-difference equations are then solved in a leapfrog manner over an equidistantly spaced mesh until a steady-state electromagnetic behavior is evolved. The transient field can be evaluated with prior knowledge of the initial field, boundary, and source conditions.

The orthogonal grid of dimensions $N_x \times N_y \times N_z$ requires $N = 6(N_x \cdot N_y \cdot N_z)$ degrees of freedom to represent the field vectors in a 3D space, where N is also know as *volumetric grid cells*. The total memory required to store the field and perform coefficient update increases as $O(N)$. In a nutshell, the factors influencing the computational load are the number of volumetric grid cells N, the number of time steps, and accumulative phase errors during numerical wave propagation.

Although a simple technique, FDTD is subject to limitations that become obstacles in using this powerful technique for commercial radio coverage predictions in wideband frequency settings. The three main challenges that are faced by FDTD applications in the field of radio propagation include

(1) *Computational resources*: FDTD method is computationally expensive because it models and discretizes the complete physical model under study into a volumetric mesh grid where the vector field components are computed in a 3D space.

(2) *Validity of numerical model*: Although FDTD provides an efficient approximation of Maxwell's equations, the results still depend on how well a model is described. In addition, it is not always possible to take into account the exact details of the environment description, which is generally subjected to random effects and may be eliminated after careful calibration of the numerical model.

(3) *Numerical dispersion*: A spatially coarse FDTD grid is obtained at the cost of numerical dispersion, which is the variation of numerical wave vector k with angular frequency $\omega = 2\pi f$, limiting the accuracy of wideband simulations. Spatially dense grids can remedy this; however, they increase the computational load.

Ray-based methods

In recent decades, the deterministic modeling of radio wave propagation has attracted a good deal of attraction and is widely studied and ventured. The most commonly used deterministic propagation modeling approach is

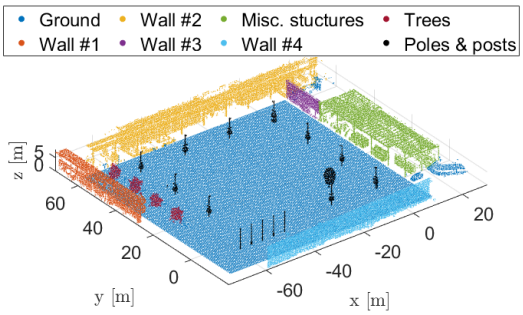

Figure 3.16. Ray-based method using point cloud geometrical description of a radio environment [189].

popularly known as raytracing. This method traces rays from the TX, and their respective paths to the RX are determined through geometric optics (GO) principles, including all fundamental propagation mechanisms. One main reason for their increasing reputation is that they provide a good compromise between accuracy and computation time. Since 5G wireless systems aim to operate at mmWave frequencies and benefit from advanced transmission schemes, raytracing models have become suitable for a variety of applications, such as, the design and planning of these systems, localization, and real-time optimization of wireless systems performance through the concept of network digital twin. Several commercial raytracing softwares are available [181–184], whereas many universities and research institutes have developed their in-house raytracing engines [185, 186].

Despite the increasing benefits, there are also technical challenges involving raytracing models. With the increase in the size of the propagation scenario, the required computational resources also increase proportionally. The advancement in graphical processing unit (GPU) technology and parallel computing alleviate this problem to some extent. Another critical aspect is the availability of an accurate environmental description as 3D digital maps. Light Detection and Ranging (LiDAR) technology allow us to obtain a high-resolution digital database of the desired environment capturing all its relevant details. These are commonly known as point cloud maps [187–189], obtained through laser scanning the environment and can be leveraged to improve the accuracy of site-specific quasi-deterministic modeling. Moreover, the point cloud is helpful at higher frequencies as physically small objects appear electrically large, the effect of which is visible in the coverage analysis. Figure 3.16 depicts an exemplary point cloud geometrical model for raytracing simulations.

Hybrid methods

Full-wave numerical methods can become too complex, and simulations may not converge when the propagation scenario is large, thus restricting their use in such cases. On the other hand, the raytracing methods are not limited by the sheer size of the propagation scenario but provide a less accurate solution for complex propagation effects because it is based on GO approximations that assume electrically large and homogenous material objects. For small and inhomogeneous structures, the accuracy of raytracing reduces. However, a meaningful combination or hybridization of the two modeling approaches may provide an optimal solution for site-specific propagation modeling of large and dense environments [190, 191].

3.5.2 Stochastic modeling of radio channels

Stochastic channel models statistically model channel parameters, such as delay, Doppler shift, and pathloss through probablity distributions. Geometry-based stochastic channel models (GSCMs) are a particular category of stochastic channel models [192–194], which distribute scatterers and assign their properties in a stochastic manner and perform a simplified raytracing. GSCMs also suit better to dynamic environments since they conveniently model the motion of TX, RX, and/or scatterers [195, 196]. A detailed description and classification of stochastic channel models are available in [172, 173].

3.6 Contributions of the thesis

3.6.1 Indoor coverage analysis with full-wave FDTD simulations

The site-specific and deterministic evaluation of radio environments utilizes raytracing or numerical simulations. Raytracing based on physical optics is a popular and efficient method involving approximations that lead to a trade-off between complexity and accuracy. On the other hand, full-wave numerical techniques, such as FDTD, described in Section 3.5.1 are much more accurate but are computationally complex when the electrical size of the environment becomes large. However, this problem can be potentially addressed by using advanced graphics processing unit (GPU) technology that helps accelerate the simulations for their fast convergence.

[VI] endows a narrowband multipath characterization of an indoor office

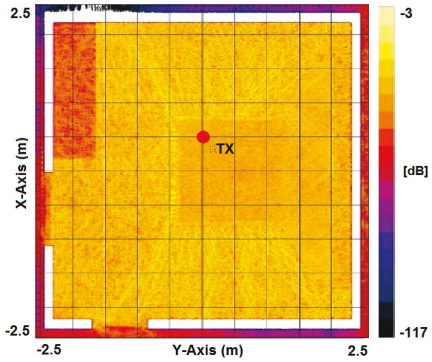

Figure 3.17. Electric field cartograpghy for small indoor office (xy- plane, $z = 1.2\,\mathrm{m}$).

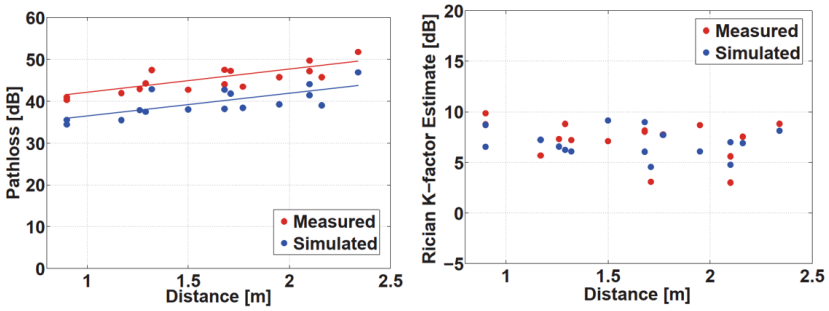

(a) (b)

Figure 3.18. Comparison between measured and FDTD simulations at $3.1\,\mathrm{GHz}$: (a) Pathloss and (b) Ricean K-factor.

room at the center frequencies of $3.1\,\mathrm{GHz}$ and $3.5\,\mathrm{GHz}$. The $3\,\mathrm{GHz}$ is typical for wireless local area network (WLAN) and worldwide interoperability for microwave access (WiMAX). A commercially available 3D full-wave FDTD solver, SEMCAD-X, is used to demonstrate its applicability for large-scale propagation predictions compared to the traditional raytracing method. The simulated pathloss and small-scale K-factor are validated through MIMO channel measurements in the same office room.

Figure 3.17 depicts the 2D electric field map ($z = 1.2\,\mathrm{m}$) generated by the FDTD simulations where the TX is located on a table in the middle of the room. It can be seen that the electric field attenuates at different levels while propagating through the room and interacting with different objects such as cupboards, shelves, and walls.

Figure 3.18(a) illustrates the comparison of simulated and measured pathloss at $3.1\,\mathrm{GHz}$, which are proportional but with a constant offset of about $5.5\,\mathrm{dB}$. Figure 3.18(b) presents the Ricean K-factor estimated from both simulations and measurements at $3.1\,\mathrm{GHz}$, where some random variations were observed with a standard deviation of $5.6\,\mathrm{dB}$.

It was concluded that FDTD numerical simulations with SEMCAD-X capture the distance-decaying factor of the radio wave propagation and the small-scale fading effects but could not predict the absolute pathloss level because of several factors, including numerical wave dispersion, pathloss estimation from the simulated electric field and imperfect absorbing boundary conditions. Since the difference of absolute pathloss level between measurements and simulations is a constant offset, it can be used to correct the simulated pathloss levels. However, this correction factor may vary from simulation scenarios and settings. Hence, it is safe to use SEMCAD-X simulations only for studying the distance dependency of pathloss and not the absolute level.

3.6.2 Comparing multi-frequency power angular spectra for an indoor environment

Developing suitable channel models for system design and performance analysis of 5G wireless systems requires critical insights into the frequency dependency of radio channels and spatial consistency of multipath in the angular domain at a wide range of frequency bands. [VII] provides a detailed comparison of power angular spectra (PAS) at 2, 15, 28, and $60\,\mathrm{GHz}$. The analysis is performed based on multi-frequency radio channel measurements for LOS and NLOS scenarios in the same indoor environment, i.e., a large coffee room. The measurements were carried out using VNA based channel sounder described in Section 3.2.5, which utilized LO at 28 and $60\,\mathrm{GHz}$ frequency bands for generating the mmWave radio signal. At each frequency band, a high delay resolution was achieved by setting the measurement bandwidth of $3\,\mathrm{GHz}$. A MISO measurement configuration was employed at $2\,\mathrm{GHz}$, where a virtual array (12×12) was realized at the RX side. For mmWave frequency bands, rotational measurement setup was accomplished by rotating the directional RX antenna in a 360° azimuth plane, while the omnidirectional TX antenna was kept static. The multipath parameters, i.e., power and DOA at the RX, were extracted by applying a conventional beamformer, explained in Section 3.4.6, on propagation paths at $2\,\mathrm{GHz}$ band. A multi-dimensional multipath estimation algorithm based on local maxima search in the power-angle-delay profile (PADP) was used for other frequency bands and is described in [VII].

Figure 3.19 manifests the normalized PAS plotted concurrently for the studied frequency bands for both LOS and NLOS channel conditions. It can be observed that the $2\,\mathrm{GHz}$ channel is rich in multipath compared to

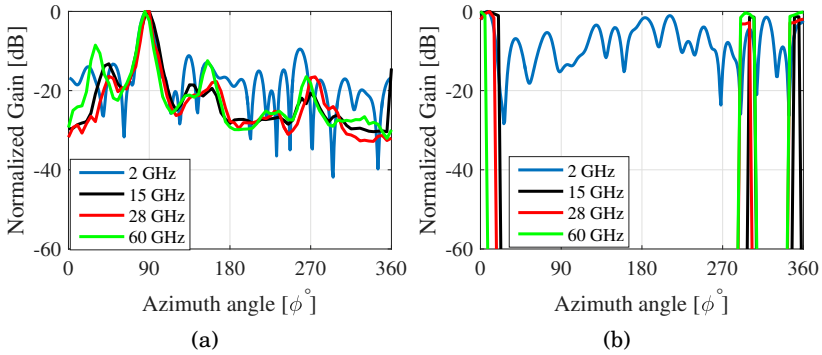

Figure 3.19. Power angular spectrum (PAS) at 15, 28, and 60 GHz: (a) LOS and (b) NLOS.

the channels at other frequency bands. It is also interesting to note that spatially strong paths exist at all frequencies, but paths at 15 and 28 GHz follow each other quite closely.

The radio channels in the LOS condition demonstrate a similar spatial spread at all considered frequency bands and can be spatially modeled similarly. The NLOS channels exhibit a wider spatial spread altogether. The paths in the radio channels at frequencies 15, 28, and 60 GHz appear to be spatially consistent. At the same time, they are less consistent at 2 GHz, where penetrated and diffracted paths also exist in abundance.

3.6.3 Characterizing centimeter and millimeter wave MIMO channels for 5G device-to-device applications

Device-to-Device (D2D) wireless communications refer to direct communication between two wireless nodes or sensors without any interface to traditional wireless infrastructure, such as cell towers in cellular networks. Many applications have been envisaged for D2D networks, including proximity-based networking, tactical communications, and situation awareness of military personnel on a battlefield. The coexistence of multiple frequency bands in a D2D wireless system may improve its reliability and efficiency. This requires a thorough understanding of radio propagation channels at the multiple frequency bands operating in the same radio environment. The joint characterization of cmWave and mmWave frequency bands could help in identifying the frequency dependency of radio channels and enable the development of suitable channel models for D2D applications.

[VIII] presents a detailed description of a propagation channel measurements campaign performed in an outdoor environment within the

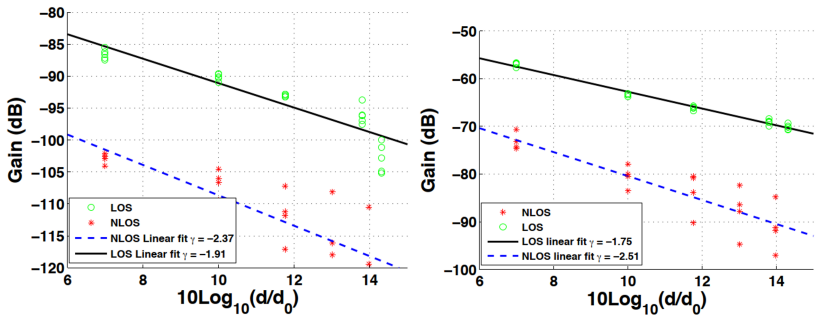

(a) (b)

Figure 3.20. Distance dependent pathloss: (a) cmWave and (b) mmWave.

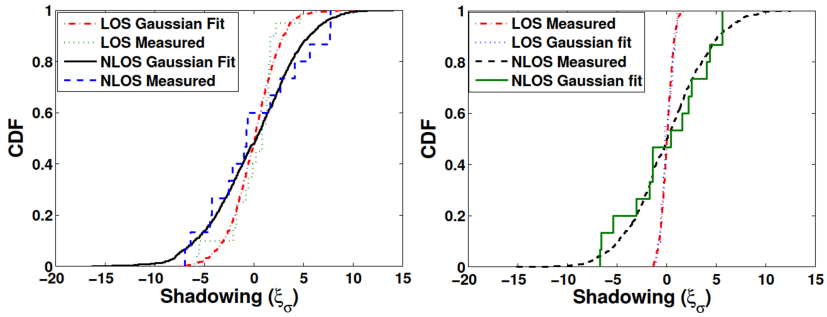

(a) (b)

Figure 3.21. Shadowing fading (ξ_σ): (a) cmWave and (b) mmWave.

cmWave $2-6\,\mathrm{GHz}$ and mmWave $59-63\,\mathrm{GHz}$ and frequency bands. The measurements were conducted for both LOS and NLOS scenarios using a VNA-based frequency-domain channel sounder setup at both frequency bands. The channel sounder generates a mmWave signal by employing frequency up- and down-converters. Different propagation channel parameters such as distance-dependent pathloss exponent (γ), shadowing gain (ξ_σ), rms delay spread (τ_{rms}), and small-scale fading statistics were extracted and compared to motivate suitable channel models in both bands. These channel parameters are mathematically and intuitively discussed in Section 3.3 and 3.4. The results, shown in Figure 3.20, demonstrate substantial similarity for the γ values between cmWave and mmWave bands, with 1.79 and 1.91 for the LOS scenario and 2.51 and 2.37 for the NLOS scenario, respectively. The ξ_σ and τ_{rms} were both modeled with a lognormal distribution. Furthermore, comparing mmWave to cmWave, the standard deviation σ of ξ_σ was $1.7\,\mathrm{dB}$ and $0.64\,\mathrm{dB}$ more in the LOS and NLOS scenarios, respectively, as illustrated in Figure 3.21.

The values of τ_{rms} indicate less delay dispersion in the mmWave channel

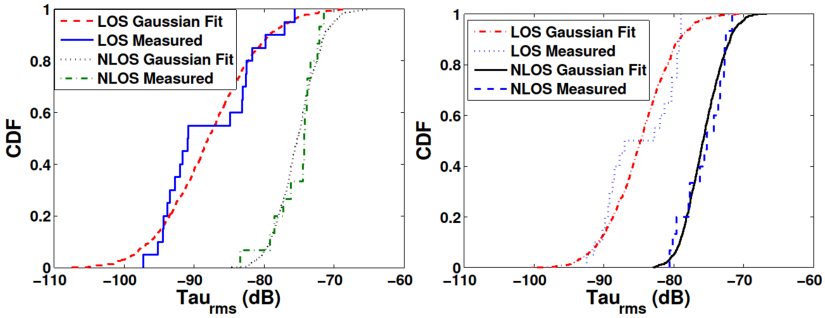

Figure 3.22. RMS delay spread (τ_{rms}): (a) cmWave and (b) mmWave.

compared to the cmWave channel for both LOS and NLOS channels, as shown in Figure 3.22. The m-Nakagami distribution was used to model the small-scale fading statistics for both frequency bands. The m-parameter was found to be a random variable, which was modeled as a Gaussian distribution. However, the mean value of the m-parameter is smaller in the mmWave band than in the cmWave band. This shows that small-scale fading results in a relatively more significant fluctuation of the signal envelope in the mmWave band than in the cmWave band for both LOS and NLOS scenarios.

4. Summary of publications

[I] Characterization of vehicle penetration loss at wireless communication frequencies

The paper presents the characterization of Vehicle Penetration Loss (VPL) at wireless communication frequencies up to $6\,\text{GHz}$. VPL is evaluated both empirically and numerically by exploiting different automotive window coatings. Ultra-wideband (UWB) radio channel measurements were performed for the frequency range of $0.6 - 6.0\,\text{GHz}$ inside an industrial facility employing a modern hatchback passenger car. The measured and simulated results were found in proximity of each other. The results imply that the use of metallized automotive films can adversely affect the communication of radio signals into vehicles.

[II] Estimating reflection and transmission losses for link-obstructing objects at 70 GHz for 5G wireless backhauling

This paper evaluates the reflection and transmission loss due to link-obstructing objects at $70\,\text{GHz}$ frequency band, ranging from the human body to various building materials and vegetation. For this purpose, a free space wideband mmWave channel sounding setup is employed in the anechoic chamber and outdoors. The results indicate that building materials, human beings, and trees cause significant attenuation of the $70\,\text{GHz}$ radio signals, which is, on average $45 - 50\,\text{dB}$. On the other hand, building materials such as windows, laminated or painted plywood, medium-density fiberboard, and plasterboard are good reflectors.

[III] On-site permittivity estimation at 60 GHz through reflecting surface identification in the point cloud

This paper presents a novel method for the on-site estimation of materials permittivities. It utilizes an accurate geometrical database and a limited set of channel measurements of the given environment for identifying flat and smooth surfaces responsible for specular reflections. The method was experimentally tested with limited radio channel measurements at 60 GHz in a large empty office room. The estimated permittivity values are visualized as a 3-D map, giving an intuitive understanding of the materials constituting the environment.

[IV] Modeling human blockage at 5G millimeter-wave frequencies

Recipient of 2021 R.W.P King Paper Award by IEEE Antenna and Propagation Society (AP-S).

The paper presents human blockage measurements in the anechoic chamber at 15, 28, and 60 GHz frequencies employing 15 human subjects of different sizes and weights. An effective 3-D human blockage model as a double-truncated multiple knife-edge (DTMKE) scheme is also proposed. By calculating diffraction using DTMKE, the frequency, body orientation, and antenna height dependence of the blockage are most accurately reproduced compared to the existing models, such as the absorbing double knife-edge model and third-generation partnership project (3GPP) human blockage model.

[V] Full-wave characterization of an indoor office environment for accurate coverage analysis

The paper presents a full-wave characterization of an indoor office environment at a Wireless Local Area Network (WLAN) and Worldwide Interoperability for Microwave Access (WIMAX) frequencies using the finite-difference time-domain (FDTD) numerical technique. Numerical simulations were carried out using a 3D full-wave electromagnetic solver SEMCAD-X, and simulated results, including pathloss and small-scale fading characteristics, are validated through multiple-input multiple-output (MIMO) channel measurements. The simulated and measured results are

found to be in proximity to each other.

[VI] Simulating specular reflections for point cloud geometrical database of the environment

Winner of First Prize IET Best Student Paper Award at Loughborough Antennas and Propagation Conference (LAPC'15), Loughborough, UK, 2015.

The paper presents the mathematical formulation for simulating specular reflections in a point cloud geometrical description of an environment. It evaluates the total specular reflected field as a coherent sum of the individual field contributions originating from the elementary surfaces over an area approximately equal to the first Fresnel reflection zone. The numerical and experimental results demonstrate the accuracy of the proposed formulation.

[VII] Multi-frequency power angular spectrum comparison for an indoor environment

Winner of ESoA Best Student Paper Award at European Conference on Antennas and Propagation (EuCAP'17), Paris, France, 2017.

The paper compares power angular spectra at frequencies below and above 6 GHz, i.e., 2, 15, 28, and 60 GHz. The analysis in the paper is based on multi-frequency radio channel measurements in an indoor coffee room environment for both line-of-sight (LOS) and non-LOS (NLOS) scenarios. For multipath extraction, two different methodologies are used below and above 6 GHz frequency bands, respectively. The results indicate that LOS channels demonstrate a similar spatial spread at all the frequencies considered and can be spatially modeled similarly. The NLOS channels exhibit a larger spatial spread overall. The paths at above 6 GHz channels appear to be spatially more consistent than those below 6 GHz, where penetrated and diffracted paths also exist.

[VIII] Joint characterization of mmWave and cmWave device-to-device fading channels

The paper presents a detailed description of a propagation channel measurement campaign performed in an outdoor environment within the millimeter-wave (mmWave) $59-63$ GHz and centimeter-wave (cmWave) $2-6$ GHz frequency bands. The measurements were conducted for line-of-sight (LOS) and non-LOS (NLOS) scenarios. The propagation channel parameters, such as distance-dependent pathloss exponent (γ), shadowing gain (ξ_σ), root mean square (rms) delay spread (τ_{rms}) and amplitude fading statistics were extracted and analyzed to motivate a suitable channel model in both bands. The model developed can be used for realistic performance evaluations of devices operating in the cmWave and/or mmWave bands.

5. Conclusions

The rapid advancements in the field of wireless communication technologies are driven by immersive and high-end applications demanding extreme data rates. The wireless propagation channel is the premier and central component of any wireless communication system in which radio waves propagate and interact with physical objects of the environment according to the governing Maxwell's equations. Radio wave propagation may become intrinsically complex depending on the radio environment. Therefore, we need to exploit and grasp the perplexities of the wireless propagation channel for designing, developing, and deploying state-of-the-art wireless systems. Moreover, standardization of technologies is a prerequisite for efficient wireless systems and their subsequent services with the objective of achieving compatibility, interoperability, safety, repeatability, and quality. The standardization process requires a reference radio channel model for comparing and evaluating the performance of potential candidate methods. This alludes to a fundamental question, i.e., *what constitutes a good radio channel model?* Ideally, a good radio channel model can reproduce the significant aspects of a radio channel in the context of the wireless system intended to be deployed. In practice, the answer to this question is convoluted and subjective to the required level of accuracy. A radio channel model is a recipe whose ingredients may depend on numerous factors, such as carrier frequency, deployment scenario, mobility, scatterers in the radio environment, etc. A multipurpose radio channel model may become too complicated for practical purposes; hence, radio channel models are desired to be objective and simple, keeping in view the trade-off between their accuracy and simplicity.

The main goal of this thesis was to characterize multipath radio environments at cmWave and mmWave frequencies to assist the process of channel model development for 5G wireless systems, also paving the way for future

generation wireless technologies. To accomplish this goal, we investigated several research problems associated with different aspects of the multi-path radio channels in indoor and outdoor environments. These studies involved considerable radio channel measurements, elaborate numerical simulations, systematic data post-processing and analysis, and rigorous mathematical modeling. Let's reexamine and construe the research questions defined in the scope and discussed in the two main chapters of the thesis to discern if the relevant objectives were realized.

Chapter 2 focused on modeling the interaction of radio waves with physical objects of the environment. We canvassed how different material objects affect radio wave propagation in built environments at mmWave frequencies. For this purpose, transmission and reflection losses were estimated through over-the-air measurements for typical link-obstructing objects present in built environments and outdoors at $70\,\mathrm{GHz}$. The results demonstrate that energy-efficient building windows, laminated plywood, and plasterboard are good reflectors of mmWave signals. In contrast, humans and some energy-efficient windows attenuate mmWave signals as high as $40\,\mathrm{dB}$. These results may enable the adequate design and deployment of mmWave backhaul and beamforming links in urban environments. Further, we evaluated the penetration of cmWave signals into a car of a standard sedan-type chassis and found that when vehicles are equipped with energy-efficient windows, the signals may deteriorate up to $20\,\mathrm{dB}$ thereby reducing the effective coverage inside the vehicle. This may be valuable and serve as a reference for the implementation of V2X wireless systems and allow automobile manufacturers to optimize the location of antennas on the chassis of vehicles.

It is a well-known fact that RF characterization of composite materials through in-situ measurements in built environments is a formidable task, so we endeavored to devise an intelligent solution for evaluating the permittivity of materials in a given radio environment. Thus, we introduced a novel method that employs the point cloud geometrical database and limited radio channel measurements of the environment to obtain material permittivities. The technique works in three simple steps, i.e., (1) utilizes 3D point cloud of the environment in conjunction with the channel measurement data, (2) performs raytracing on the point cloud to identify reflection surfaces, and (3) calculates material permittivities by applying inverse reflection problem. These resulting material permittivities are then classified and visualized through a colored 3D point cloud map of the

environment and found close to the values in the ITU recommendation. The availability of a permittivity map for a given radio environment plays a crucial role in site-specific radio wave propagation simulations intended for 5G small-cell coverage study.

Humans are the most noticeable blockers of mmWave access links expected to be deployed in dense urban areas. We conducted a detailed literature survey and described various available blockage models. For quantifying the impact of human blockage on mmWave signals, we presented the first comprehensive study that determines human blockage losses through anechoic chamber measurements of 15 human subjects with different weights and sizes at 15, 28 and 60 GHz frequency bands. To accurately predict human blockage at mmWave frequencies aligned with the measurements, we proposed a novel and simple DTMKE model, which considers different human body orientations and radiating antenna heights. The results elucidate that human blockage models must consider body width, height, and thickness as these parameters strongly influence blockage loss. For different body orientations, blockage loss is proportional to the cross-section of the human body with respect to the radio link, while it decreases with the increase in the height of the transmitting antenna. Furthermore, the blockage loss increases with the increase in frequency regardless of body orientation or transmitting antenna height. These findings may facilitate 5G mmWave wireless systems and the scientific community to develop and adopt advanced blockage mitigation techniques for improving mmWave link reliability in dense urban environments with frequent human activities.

Chapter 3 discussed the viability of numerical tools that can be utilized for coverage predictions and provide prolific insights into the behavior and differences cmWave and mmWave multipath radio channels. Since full-wave numerical techniques, such as FDTD, provide the most accurate solution of Maxwell's equations for radio waves propagation, we studied the feasibility of FDTD to understand if such techniques can be successfully applied to coverage analysis. We carried out FDTD simulation for a small indoor office using commercially available software, SEMCAD, with graphical processing unit (GPU) acceleration. We observed that FDTD is computationally expensive and a comprise exists between the accuracy and complexity of simulations. Finally, multipath characterization of cmWave and mmWave radio channels is performed for indoor and outdoor radio environments in terms of their behavior in power, delay, and angle param-

eters. The results demonstrate singular and distinct properties of cmWave and mmWave radio channels. The fluctuations in the signal envelope of mmWave channels are larger than their mmWave counterparts. The mmWave channels exhibit less delay dispersion compared to cmWave radio channels. The spatial spread of multipath is similar in the LOS conditions across cmWave and mmWave radio channels. However, in the NLOS propagation conditions, the cmWave radio channels offer more spatial spread of multipath than mmWave radio channels. These inferences may aid the design, performance analysis, and deployment of 5G networks.

In a nutshell, the scientific results disseminated in the publications of this thesis are recognized by the scientific community through international best paper awards, which manifests the quality, significance, timeliness, and impact of the research. Now let us look at the future outlook and possible research directions in the context of the studies performed in this thesis. The next-generation wireless networks rely on mmWave and THz frequency spectrum, requiring a more out-of-the-box approach to radio propagation modeling by considering accurate environment description, scatterers' location, and the properties of massive antennas for beamforming applications. Furthermore, the characterization of RF properties of material objects is scarce above $100\,\mathrm{GHz}$ and must be considered. The concept of network *Digital Twin* would allow emulating the end-to-end digital mirror of the physical network that will work in parallel and enable constant evaluation and optimization of the live network. For this, site-specific coverage analysis of radio environments will have to become more sophisticated, accurate, and real-time to provide a digital mirror of the radio environment.

References

[1] ITU, International Telecommunication Union. World telecommunication/ICT indicators database. [Online]. Available: https://www.itu.int/en/ITU-D/Statistics/Pages/stat/default.aspx

[2] "Ericsson mobility report," Ericsson, Tech. Rep., November 2021. [Online]. Available: https://www.ericsson.com/4ad7e9/assets/local/reports-papers/mobility-report/documents/2021/ericsson-mobility-report-november-2021.pdf

[3] "Ericsson mobility report," Ericsson, Tech. Rep., June 2022. [Online]. Available: https://www.ericsson.com/49d3a0/assets/local/reports-papers/mobility-report/documents/2022/ericsson-mobility-report-june-2022.pdf

[4] C.-X. Wang, J. Huang, H. Wang, X. Gao, X. You, and Y. Hao, "6G wireless channel measurements and models: trends and challenges," *IEEE Vehicular Technology Magazine*, vol. 15, no. 4, pp. 22–32, Dec 2020.

[5] T. Huang, W. Yang, J. Wu, J. Ma, X. Zhang, and D. Zhang, "A survey on green 6G network: architecture and technologies," *IEEE Access*, vol. 7, pp. 175 758 –175 768, December 2019.

[6] C. D. Alwis, A. Kalla, Q.-V. Pham, P. Kumar, K. Dev, W.-J. Hwang, and M. Liyanage, "Survey on 6G frontiers: trends, applications, requirements, technologies and future Research," *IEEE Open Journal of the Communications Society*, vol. 2, pp. 836–886, April 2021.

[7] M. Shafi, A. F. Molisch, P. J. Smith, T. Haustein, P. Zhu, P. De Silva, F. Tufvesson, A. Benjebbour, and G. Wunder, "5G: a tutorial overview of standards, trials, challenges, deployment, and practice," *IEEE Journal on Selected Areas in Communications*, vol. 35, no. 6, pp. 1201–1221, 2017.

[8] Ericsson. (2020, April) 5G wireless access: An overview. [Online]. Available: https://www.ericsson.com/en/reports-and-papers/white-papers/5g-wireless-access-an-overview

[9] A. Osseiran, J. F. Monserrat, and P. Marsch, *5G mobile and wireless communications technology*. New York, NY, USA: Cambridge University Press, 2016.

[10] E. Dahlman, S. Parkvall, and J. Skold, *5G NR: the next generation wireless access technology*. Cambridge, Massachusetts, USA: Academic Press, Elsevier, 2018.

[11] ITU, International Telecommunication Union. 5G standards and specifications. [Online]. Available: https://www.itu.int/en/mediacentre/backgrounders/Pages/5G-fifth-generation-of-mobile-technologies.aspx

[12] T. S. Rappaport, S. Sun, R. Mayzus, H. Zhao, Y. Azar, K. Wang, G. N. Wong, J. K. Schulz, M. Samimi, and F. Gutierrez, "Millimeter wave mobile communications for 5G cellular: it will work!" *IEEE Access*, vol. 1, pp. 335–349, May 2013.

[13] 3GPP 5G specifications set. [Online]. Available: https://www.3gpp.org/dynareport/SpecList.htm?release=Rel-15&tech=4

[14] 5GPP 5G standards and specifications in Europe. [Online]. Available: https://5g-ppp.eu/

[15] ITU-R M.2412, "Guidelines for evaluation of radio interface technologies for IMT-2020," September 2022. [Online]. Available: https://www.itu.int/rec/R-REC-M.2150/en

[16] A. Al-Dulaimi, X. Wang, and I. Chih-Lin, "Standardization: The road to 5G," 2018.

[17] 5G Americas. [Online]. Available: https://www.5gamericas.org

[18] European Union, 5G Research and Standards. [Online]. Available: https://digital-strategy.ec.europa.eu/en/policies/5g-research-standards

[19] 5G Forum. [Online]. Available: http://www.5gforum.org/html/en/main.php

[20] 5G Mobile Communication Forum (5GMF). [Online]. Available: https://5gmf.jp/en

[21] Next Generation Mobile Networking (NGMN) Alliance. [Online]. Available: https://www.ngmn.org/

[22] ITU-R. ITU Radiocommunication Sector. [Online]. Available: https://www.itu.int/en/ITU-R/Pages/default.aspx

[23] X. Lin, J. Li, R. Baldemair, J.-F. T. Cheng, S. Parkvall, D. C. Larsson, H. Koorapaty, M. Frenne, S. Falahati, A. Grovlen *et al.*, "5G new radio: unveiling the essentials of the next generation wireless access technology," *IEEE Communications Standards Magazine*, vol. 3, no. 3, pp. 30–37, 2019.

[24] A. Ghosh, A. Maeder, M. Baker, and D. Chandramouli, "5G evolution: A view on 5G cellular technology beyond 3GPP release 15," *IEEE access*, vol. 7, pp. 127 639–127 651, 2019.

[25] E. Dahlman, S. Parkvall, and J. Skold, *5G NR: the next generation wireless access technology*. Academic Press, 2020.

[26] X. Lin, "An overview of 5G advanced evolution in 3GPP Release 18," *IEEE Communications Standards Magazine*, vol. 6, no. 3, pp. 77–83, 2022.

[27] W. Chen, J. Montojo, J. Lee, M. Shafi, and Y. Kim, "The standardization of 5G-advanced in 3GPP," *IEEE Communications Magazine*, 2022.

[28] RP-213469, "Summary for RAN Rel-18 package." [Online]. Available: http://www.3gpp.org/ftp/tsg_ran/TSG_RAN/TSGR_94e/Docs/RP-213469.zip

[29] W. Saad, M. Bennis, and M. Chen, "A vision of 6G wireless systems: applications, trends, technologies, and open research problems," *IEEE Network*, vol. 34, no. 3, pp. 134–142, 2020.

[30] A. Yazar, S. D. Tusha, and H. Arsalan, "6G vision: an ultra-flexible perspective," *ITU Journal on Future and Evolving Technologies*, vol. 1, no. 1, pp. 121–140, December 2020.

[31] H. Jiang, M. Mukherjee, J. Zhou, and J. Lloret, "Channel modeling and characteristics for 6G wireless communications," *IEEE Network*, vol. 35, no. 1, pp. 296–303, 2021.

[32] H. Tataria, M. Shafi, A. F. Molisch, M. Dohler, H. Sjöland, and F. Tufvesson, "6G wireless systems: vision, requirements, challenges, insights, and opportunities," *Proceedings of the IEEE*, vol. 109, no. 7, pp. 1166–1199, July 2021.

[33] H. Tataria, M. Shafi, M. Dohler, and S. Sun, "Six critical challenges for 6G wireless systems: a summary and some solutions," *IEEE Vehicular Technology Magazine*, vol. 17, no. 1, pp. 16–26, March 2022.

[34] Ericsson. (2022, February) 6G: connecting a cyber physical world. [Online]. Available: https://www.ericsson.com/4927de/assets/local/reports-papers/white-papers/6g--connecting-a-cyber-physical-world.pdf

[35] University of Surrey. 6G wireless: a new strategic vision. [Online]. Available: https://www.surrey.ac.uk/sites/default/files/2020-11/6g-wireless-a-new-strategic-vision-paper.pdf

[36] Nokia. (2022, January) Nokia's vision for the 6G era. [Online]. Available: https://www.nokia.com/about-us/newsroom/articles/nokias-vision-for-the-6g-era/

[37] Rohde & Schwarz. (2022, February) 6G: vision or reality? [Online]. Available: https://www.rohde-schwarz.com/us/about/stories/6g-vision-or-reality/6g-vision-or-reality_255445.html

[38] University of Oulu. 6G Flagship Project. [Online]. Available: https://www.6gflagship.com

[39] S. Hu, F. Rusek, and O. Edfors, "Beyond massive MIMO: the potential of data transmission with large intelligent surfaces," *IEEE Transactions on Signal Processing*, vol. 66, no. 10, pp. 2746–2758, May 2018.

[40] Q. Wu, S. Zhang, B. Zheng, C. You, and R. Zhang, "Intelligent reflecting surface-aided wireless communications: a tutorial," *IEEE Transactions on Communications*, vol. 69, no. 5, pp. 3313–3351, May 2021.

[41] H. Tataria, K. Haneda, A. F. Molisch, M. Shafi, and F. Tufvesson, "Standardization of propagation models for terrestrial cellular systems: a historical perspective," *International Journal of Wireless Information Networks*, vol. 28, no. 6, pp. 20–44, 2021.

[42] T. S. Rappaport, *Wireless communications principles and practice*, 2nd ed. UK: Pearson Education Inc., 2009.

[43] A. Molisch, *Wireless Communications*, 2nd ed. Wiley-IEEE Press, 2011.

[44] T. S. Rappaport, R. W. Heath, R. C. Daniels, and J. N. Murdock, *Millimeter waves wireless communications*, 1st ed. Pearson/Prentice-Hall, 2011.

[45] M. Shafi, J. Zhang, H. Tataria, A. F. Molisch, S. Sun, T. S. Rappaport, F. Tufvesson, S. Wu, and K. Kitao, "Microwave vs. millimeter-wave propagation channels: key differences and impact on 5G Cellular systems," *IEEE Communications Magazine*, vol. 56, no. 12, pp. 14–20, 2018.

[46] J. Medbo, P. Kyösti, K. Kusume, L. Raschkowski, K. Haneda, T. Jämsä, V. Nurmela, A. Roivainen, and J. Meinilä, "Radio propagation modeling for 5G mobile and wireless communications," *IEEE Communications Magazine*, vol. 54, no. 6, pp. 144–151, June 2016.

[47] C.-X. Wang, J. Bian, J. Sun, W. Zhang, and M. Zhang, "A survey of 5G channel measurements and models," *IEEE Communications Surveys and Tutorials*, vol. 20, no. 4, pp. 3142–3168, April 2018.

[48] M. Steinbauer, A. Molisch, and E. Bonek, "The double-directional radio channel," *IEEE Antennas and Propagation Magazine*, vol. 43, no. 4, pp. 51–63, 2001.

[49] S. Ju and T. S. Rappaport, "Millimeter-wave extended NYUSIM channel model for spatial consistency," in *Global Communications Conference (GLOBECOM)*. IEEE, Decmeber 2018.

[50] E. G. Larsson, O. Edfors, F. Tufvesson, and T. L. Marzetta, "Massive MIMO for next generation wireless systems," *IEEE Communications Magazine*, vol. 52, no. 2, pp. 186–195, February 2014.

[51] T. L. Marzetta, E. G. Larsson, H. Yang, and H. Q. Ngo, *Fundamentals of massive MIMO*, 1st ed. Cambirdge, UK: Cambridge University Press, 2016.

[52] A. Yaghjian, "An overview of near-field antenna measurements," *IEEE Transactions on Antennas and Propagation*, vol. 34, no. 1, pp. 30–45, January 1986.

[53] S. Wu, C.-X. Wang, e.-H. M. Aggoune, M. M. Alwakeel, and Y. He, "A non-stationary 3-D wideband twin-cluster model for 5G massive MIMO Channels," *IEEE Journal on Selected Areas in Communications*, vol. 32, no. 6, pp. 1207–1218, June 2014.

[54] X. Gao, O. Edfors, F. Tufvesson, and E. G. Larsson, "Massive MIMO in real propagation environments: do all antennas contribute equally?" *IEEE Transactions on Communications*, vol. 63, no. 11, pp. 3917–3928, November 2015.

[55] 3GPP TR 38.900, "Study on channel model for frequencies above 6 GHz," v. 14.0, April 2022.

[56] 3GPP TR 38.901, "Study on channel model for frequencies from 0.5 to 100 GHz," v. 17.0, April 2022.

[57] P. Bello, "Characterization of randomly time-variant linear channels," *IEEE Transactions on Communications Systems*, vol. 11, no. 4, pp. 360–393, 1963.

[58] 5GCM, "5G channel model for bands up to 100 GHz," Tech. Report, December 2015. [Online]. Available: http://www.5gworkshops.com/5GCM.html

[59] A. F. Molisch, H. Asplund, R. Heddergott, M. Steinbauer, and T. Zwick, "The COST259 directional channel model-part I: overview and methodology," *IEEE Transactions on Wireless Communications*, vol. 5, no. 12, pp. 3421–3433, 2006.

[60] H. Asplund, A. A. Glazunov, A. F. Molisch, K. I. Pedersen, and M. Steinbauer, "The COST 259 directional channel model-part II: macrocells," *IEEE Transactions on Wireless Communications*, vol. 5, no. 12, pp. 3434–3450, 2006.

[61] N. Czink and C. Oestges, "The COST 273 MIMO channel model: three kinds of clusters," in *10th International Symposium on Spread Spectrum Techniques and Applications*. IEEE, 2008, pp. 282–286.

[62] L. Liu, C. Oestges, J. Poutanen, K. Haneda, P. Vainikainen, F. Quitin, F. Tufvesson, and P. De Doncker, "The COST 2100 MIMO channel model," *IEEE Wireless Communications*, vol. 19, no. 6, pp. 92–99, 2012.

[63] H. Tataria and F. Tufvesson, "Impact of spatially consistent channels on digital beamforming for millimeter-wave systems," in *14th European Conference on Antennas and Propagation (EuCAP)*. IEEE, 2020.

[64] D. K. Cheng, *Field and wave electromagnetics*, 2nd ed. Essex, UK: Pearson Education Limited, 2014.

[65] A. Räisänen and A. Lehto, *Radio engineering for wireless communication and sensor applications*. Artech House, 2003.

[66] ITU-R M.2040, "Effects of building materials and structures on radiowave propagation above about 100 MHz," September 2021. [Online]. Available: https://www.itu.int/dms_pubrec/itu-r/rec/p/R-REC-P.2040-2-202109-I!!PDF-E.pdf

[67] H. L. Bertoni, *Radio propagation for modern wireless systems*, 1st ed. Upper Saddle River, N.J: Prentice Hall PTR cop. 2000, 2000.

[68] N. Favretto-Cristini, P. Cristini, and E. De Bazelaire, "Influence of the interface Fresnel zone on the reflected P-wave amplitude modelling," *Geophysical Journal International*, vol. 171, no. 2, pp. 841–846, 11 2007. [Online]. Available: https://doi.org/10.1111/j.1365-246X.2007.03573.x

[69] M. Kvasnicka and V. Cervený, "Analytical expression for Fresnel volumes and interface Fresnel zones of seismic body waves. part 1: direct and unconverted reflected waves," *Studia Geophysica et Geodaetical*, vol. 40, no. 2, pp. 136–155, 04 1996. [Online]. Available: https://link.springer.com/article/10.1007/BF02296354

[70] B. B. Baker and E. T. Copson, *The mathematical theory of Huygens' principle*, 2nd ed. Oxford University Press, 1953.

[71] M. Bon and E. Wolf, *Principles of optics*. Pergamon Press, New York, 1959.

[72] B. B. Baker and E. T. Copson, *Radiation and scattering of waves*. Prentice Hall, Upper Saddle River, N.J., 1973.

[73] J. B. Keller, "Geometrical theory of diffraction," *Josa*, vol. 52, no. 2, pp. 116–130, 1962.

[74] P. H. Pathak, G. Carluccio, and M. Albani, "The uniform geometrical theory of diffraction and some of its applications," *IEEE Antennas and Propagation Magazine*, vol. 55, no. 4, pp. 41–69, 2013.

[75] M. Abramowitz and I. Stegun, *Handbook of mathematical functions: with formulas, graphs, and mathematical tables*, ser. Applied mathematics series. Dover Publications, 1965.

[76] P. Beckmann and A. Spizzichino, *The scattering of electromagnetic waves from rough surfaces*, ser. A Pergamon Press book. Pergamon Press; [distributed in the Western Hemisphere by Macmillan, New York], 1963.

[77] M. G. Kivelson and S. A. Moszkowski, "Reflection of electromagnetic waves from a rough surface," *Journal of Applied Physics*, vol. 36, no. 11, pp. 3609–3612, 1965.

[78] J. A. Holzer and C. C. Sung, "Scattering of electromagnetic waves from a rough surface. II," *Journal of Applied Physics*, vol. 49, no. 3, pp. 1002–1011, 1978.

[79] K. A. O'Donnell and E. R. Mendez, "Experimental study of scattering from characterized random surfaces," *J. Opt. Soc. Am. A*, vol. 4, no. 7, pp. 1194–1205, Jul 1987. [Online]. Available: https://opg.optica.org/josaa/abstract.cfm?URI=josaa-4-7-1194

[80] J. A. Ogilvy, "Wave scattering from rough surfaces," *Reports on Progress in Physics*, vol. 50, no. 12, p. 1553, dec 1987. [Online]. Available: https://dx.doi.org/10.1088/0034-4885/50/12/001

[81] A. Ishimaru, J. S. Chen, P. Phu, and K. Yoshitomi, "Numerical, analytical, and experimental studies of scattering from very rough surfaces and backscattering enhancement," *Waves in Random Media*, vol. 1, no. 3, pp. S91–S107, 1991.

[82] P. Spiga, G. Soriano, and M. Saillard, "Scattering of electromagnetic waves from rough surfaces: a boundary integral method for low-gazing angles," *IEEE Transactions on Antennas and Propagation*, vol. 56, no. 7, pp. 2043–2050, 2008.

[83] R. Vaughan and J. Bach Andersen, *Channels, propagation and antennas for mobile communications*, 1st ed. London: IEE electromagnetic waves series 50, 2003.

[84] A. Bole, A. Wall, and A. Norris, "Chapter 3 - Target detection," in *Radar and ARPA Manual*, 3rd ed., A. Bole, A. Wall, and A. Norris, Eds. Oxford: Butterworth-Heinemann, 2014, pp. 139–213.

[85] D. Didascalou, M. Dottling, N. Geng, and W. Wiesbeck, "An approach to include stochastic rough surface scattering into deterministic ray-optical wave propagation modeling," *IEEE Transactions on Antennas and Propagation*, vol. 51, no. 7, pp. 1508–1515, 2003.

[86] V. Degli-Esposti, "A diffuse scattering model for urban propagation prediction," *IEEE Transactions on Antennas and Propagation*, vol. 49, no. 7, pp. 1111–1113, 2001.

[87] M. Bensebti, J. McGeehan, and M. Beach, "Indoor multipath radio propagation measurements and characterisation at 60 GHz," in *21st European Microwave Conference*, vol. 2. IEEE, 1991, pp. 1217–1222.

[88] G. Delisle and L. Talbi, "Narrow and wideband measurements for millimeter waves PCS channel characterization," in *4th International Conference on Universal Personal Communications (ICUPC)*. IEEE, 1995, pp. 206–210.

[89] P. F. Smulders and L. Correia, "Characterisation of propagation in 60 GHz radio channels," *Electronics & Communication Engineering Journal*, vol. 9, no. 2, pp. 73–80, 1997.

[90] M. G. Sánchez, A. M. Hammoudeh, E. Grindrod, and J.-P. Kermoal, "Coherence bandwidth characterization in an urban microcell at 62.4 GHz," *IEEE Transactions on Vehicular Technology*, vol. 49, no. 2, pp. 607–613, 2000.

[91] A. Swindlehurst, G. German, J. Wallace, and M. Jensen, "Experimental measurements of capacity for MIMO indoor wireless channels," in *Third Workshop on Signal Processing Advances in Wireless Communications (SPAWC). Workshop Proceedings (Cat. No.01EX471)*. IEEE, 2001, pp. 30–33.

[92] H. Nguyen, J. Andersen, and G. Pedersen, "A stochastic model of spatio-temporally correlated narrowband MIMO channel based on indoor measurement," in *15th International Symposium on Personal, Indoor and Mobile Radio Communications (IEEE Cat. No.04TH8754)*, vol. 3. IEEE, 2004, pp. 1827–1831.

[93] N. Moraitis and P. Constantinou, "Indoor channel measurements and characterization at 60 GHz for wireless local area network applications," *IEEE Transactions on Antennas and Propagation*, vol. 52, no. 12, pp. 3180–3189, December 2004.

[94] A. H. Henderson, C. J. Durkin, and G. D. Durgin, "Finding the right small-scale fading distribution for a measured indoor 2.4 GHz channel," in *Antennas and Propagation Society International Symposium*. IEEE, Septemeber 2008.

[95] H. Tsuchiya, "Characterization of the radio propagation channel in residential environment for smart meter communications," in *Asia-Pacific Microwave Conference 2011*, December 2011, pp. 713–716.

[96] V. Semkin, U. Virk, A. Karttunen, K. Haneda, and A. V. Räisänen, "E-band propagation channel measurements in an urban street canyon," in *9th European Conference on Antennas and Propagation (EuCAP)*. IEEE, 2015.

[97] Hewlett Packard (HP), "Spectrum analysis....Field strength measurements," in *Spectrum Analyzer Series, Application Note 150-10*, September 1976.

[98] T. Felhauer, P. W. Baier, W. König, and W. Mohr, "Optimized wideband system for unbiased mobile radio channel sounding with periodic spread spectrum signals," *IEICE Transactions on Communications*, vol. 76, no. 8, pp. 1016–1029, 1993.

[99] J. Proakis and M. Salehi, *Digital communications*. McGraw-Hill, 2008. [Online]. Available: https://books.google.fi/books?id=ABSmAQAACAAJ

[100] J. Kivinen, T. Korhonen, P. Aikio, R. Gruber, P. Vainikainen, and S.-G. Haggman, "Wideband radio channel measurement system at 2 GHz," *IEEE Transactions on Instrumentation and Measurement*, vol. 48, no. 1, pp. 39–44, 1999.

[101] R. J. Pirkl and G. D. Durgin, "Optimal sliding correlator channel sounder design," *IEEE Transactions on Wireless Communications*, vol. 7, no. 9, pp. 3488–3497, 2008.

[102] M. Kmec, J. Sachs, P. Peyerl, P. Rauschenbach, R. Thomä, and R. Zetik, "A novel ultra-wideband real-time MIMO channel sounder architecture," *XXVIIIth General Assembly of URSI*, pp. 23–29, 2005.

[103] V.-M. Kolmonen, J. Kivinen, L. Vuokko, and P. Vainikainen, "5.3-GHz MIMO radio channel sounder," *IEEE Transactions on Instrumentation and Measurement*, vol. 55, no. 4, pp. 1263–1269, 2006.

[104] R. Müller, D. A. Dupleich, C. Schneider, R. Herrmann, and R. S. Thomä, "Ultrawideband 3D mmWave channel sounding for 5G," in *XXXIth URSI General Assembly and Scientific Symposium (URSI GASS)*, 2014.

[105] G. R. MacCartney and T. S. Rappaport, "A flexible millimeter-wave channel sounder with absolute timing," *IEEE Journal on Selected Areas in Communications*, vol. 35, no. 6, pp. 1402–1418, 2017.

[106] G. Simon and J. Schoukens, "Robust broadband periodic excitation design," *IEEE Transactions on Instrumentation and Measurement*, vol. 49, no. 2, pp. 270–274, 2000.

[107] K. Remley, "Multisine excitation for ACPR measurements," in *MTT-S International Microwave Symposium Digest*, vol. 3. IEEE, 2003, pp. 2141–2144.

[108] N. B. Carvalho, K. A. Remley, D. Schreurs, and K. G. Gard, "Multisine signals for wireless system test and design [Application Notes]," *IEEE Microwave Magazine*, vol. 9, no. 3, pp. 122–138, 2008.

[109] D. M. Pozar, *Microwave engineering*, 2nd ed. New York, USA: Wiley, 1998.

[110] J. W. Cooley, P. A. W. Lewis, and P. D. Welch, "The fast Fourier transform and its applications," *IEEE Transactions on Education*, vol. 12, no. 1, pp. 27–34, 1969.

[111] E. O. Brigham, *The fast Fourier transform and its applications*. Prentice-Hall, Inc., 1988.

[112] E. Weisstein. Fourier transform from MathWorld–A wolfram web resource. [Online]. Available: https://mathworld.wolfram.com/FourierTransform.html

[113] J. Jarvelainen, M. Kurkela, A. Karttunen, K. Haneda, and J. Putkonen, "70 GHz radio wave propagation prediction in a large office," in *Loughborough Antennas and Propagation Conference (LAPC)*, 2014, pp. 420–424.

[114] K. Haneda, J. Jarvelainen, A. Karttunen, M. Kyro, and J. Putkonen, "Indoor short-range radio propagation measurements at 60 and 70 GHz," in *8th European Conference on Antennas and Propagation (EuCAP)*, 2014, pp. 634–638.

[115] J. Vehmas, J. Jarvelainen, S. L. H. Nguyen, R. Naderpour, and K. Haneda, "Millimeter-wave channel characterization at Helsinki airport in the 15, 28, and 60 GHz bands," in *84th Vehicular Technology Conference (VTC)*, 2016.

[116] C.-L. Cheng and A. Zajić, "Characterization of propagation phenomena relevant for 300 GHz wireless data center links," *IEEE Transactions on Antennas and Propagation*, vol. 68, no. 2, pp. 1074–1087, 2020.

[117] T. Rappaport, K. Remley, C. Gentile, A. Molisch, and A. Zajić, *Radio propagation measurements and channel modeling: Best practices for millimeter-wave and sub-terahertz frequencies*. Cambridge University Press, 2022. [Online]. Available: https://books.google.fi/books?id=1D2CEAAAQBAJ

[118] J. Kivinen and P. Vainikainen, "Wideband Indoor Radio Channel Measurements at 5.3 GHz," in *27th European Microwave Conference*, vol. 1, 1997, pp. 464–469.

[119] S. Ranvier, J. Kivinen, and P. Vainikainen, "Millimeter-Wave MIMO Radio Channel Sounder," *IEEE Transactions on Instrumentation and Measurement*, vol. 56, no. 3, pp. 1018–1024, 2007.

[120] S. Ranvier, M. Kyro, K. Haneda, T. Mustonen, C. Icheln, and P. Vainikainen, "VNA-based wideband 60 GHz MIMO channel sounder with 3-D arrays," in *Radio and Wireless Symposium*. IEEE, 2009, pp. 308–311.

[121] V.-M. Kolmonen, P. Almers, J. Salmi, J. Koivunen, K. Haneda, A. Richter, F. Tufvesson, A. F. Molisch, and P. Vainikainen, "A dynamic dual-link wideband MIMO channel sounder for 5.3 GHz," *IEEE Transactions on Instrumentation and Measurement*, vol. 59, no. 4, pp. 873–883, 2010.

[122] P. Koivumäki, M. Heino, K. Haneda, M. Puranen, and J. Pesola, "Dynamic polarimetric wideband channel sounding in an elevator shaft," in *European Conference on Networks and Communications (EuCNC)*, 2019, pp. 295–299.

[123] 5G Workshops, "5G channel model for bands up to 100 GHz." [Online]. Available: http://www.5gworkshops.com/2015/5G%20channel%20model%20for%20bands%20up%20to%20100%20GHz%20-%20Second%20revisioin.pdf

[124] mmMagic, "6-100 GHz channel modeling for 5G: measurements and modeling plan in mmMagic." [Online]. Available: https://bscw.5g-ppp.eu/pub/bscw.cgi/d76988/mmMagic_WhitePaper-W2.1.pdf

[125] K. Haneda, M. Peter, J. Medbo, M. Beach, R. d'Errico, S. Wu, and J.-M. Conrat, "Radio channel sounding campaigns in EU H2020 mmMAGIC project for 5G channel modeling," in *International Symposium on Antennas and Propagation (ISAP)*. IEEE, 2016, pp. 596–597.

[126] J. Kivinen, X. Zhao, and P. Vainikainen, "Empirical characterization of wideband indoor radio channel at 5.3 GHz," *IEEE Transactions on Antennas and Propagation*, vol. 49, no. 8, pp. 1192–1203, 2001.

[127] S. Geng, S. Ranvier, X. Zhao, J. Kivinen, and P. Vainikainen, "Multipath propagation characterization of ultra-wide band indoor radio channels," in *International Conference on Ultra-wideband*. IEEE, 2005, pp. 11–15.

[128] S. Geng, J. Kivinen, X. Zhao, and P. Vainikainen, "Millimeter-wave propagation channel characterization for short-range wireless communications," *IEEE Transactions on Vehicular Technology*, vol. 58, no. 1, pp. 3–13, 2008.

[129] J. Poutanen, K. Haneda, J. Salmi, V.-M. Kolmonen, F. Tufvesson, and P. Vainikainen, "Analysis of radio wave scattering processes for indoor MIMO channel models," in *20th International Symposium on Personal, Indoor and Mobile Radio Communications*. IEEE, 2009, pp. 102–106.

[130] J. Poutanen, K. Haneda, J. Salmi, V.-M. Kolmonen, J. Koivunen, P. Almers, and P. Vainikainen, "Analysis of radio wave propagation from an indoor hall to a corridor," in *Antennas and Propagation Society International Symposium*. IEEE, 2009.

[131] S. Wyne, K. Haneda, S. Ranvier, F. Tufvesson, and A. F. Molisch, "Beamforming effects on measured mm-wave channel characteristics," *IEEE Transactions on Wireless Communications*, vol. 10, no. 11, pp. 3553–3559, 2011.

[132] K. Haneda, A. Khatun, M. Dashti, T. A. Laitinen, V.-M. Kolmonen, J.-I. Takada, and P. Vainikainen, "Measurement-based analysis of spatial degrees of freedom in multipath propagation channels," *IEEE Transactions on Antennas and Propagation*, vol. 61, no. 2, pp. 890–900, 2012.

[133] K. Haneda, C. Gustafson, and S. Wyne, "60 GHz spatial radio transmission: Multiplexing or beamforming?" *IEEE Transactions on Antennas and Propagation*, vol. 61, no. 11, pp. 5735–5743, 2013.

[134] K. Haneda, J. Järveläinen, A. Karttunen, M. Kyrö, and J. Putkonen, "A statistical spatio-temporal radio channel model for large indoor environments at 60 and 70 GHz," *IEEE Transactions on Antennas and Propagation*, vol. 63, no. 6, pp. 2694–2704, 2015.

[135] K. Haneda, S. L. H. Nguyen, J. Järveläinen, and J. Putkonen, "Estimating the omni-directional pathloss from directional channel sounding," in *10th European Conference on Antennas and Propagation (EuCAP)*. IEEE, 2016.

[136] K. Kalliola and P. Vainikainen, "Dynamic wideband measurement of mobile radio channel with adaptive antennas," in *48th Vehicular Technology Conference (VTC). Pathway to Global Wireless Revolution (Cat. No. 98CH36151)*, vol. 1. IEEE, 1998, pp. 21–25.

[137] X. Zhao, J. Kivinen, P. Vainikainen, and K. Skog, "Propagation characteristics for wideband outdoor mobile communications at 5.3 GHz," *IEEE Journal on Selected Areas in Communications*, vol. 20, no. 3, pp. 507–514, 2002.

[138] J. Laurila, K. Kalliola, M. Toeltsch, K. Hugl, P. Vainikainen, and E. Bonek, "Wideband 3D characterization of mobile radio channels in urban environment," *IEEE Transactions on Antennas and Propagation*, vol. 50, no. 2, pp. 233–243, 2002.

[139] K. Kalliola, H. Laitinen, P. Vainikainen, M. Toeltsch, J. Laurila, and E. Bonek, "3-D double-directional radio channel characterization for urban macrocellular applications," *IEEE Transactions on Antennas and Propagation*, vol. 51, no. 11, pp. 3122–3133, 2003.

[140] F. Fuschini, H. El-Sallabi, V. Degli-Esposti, L. Vuokko, D. Guiducci, and P. Vainikainen, "Analysis of multipath propagation in urban environment through multidimensional measurements and advanced ray tracing simulation," *IEEE Transactions on Antennas and Propagation*, vol. 56, no. 3, pp. 848–857, 2008.

[141] M. Kyro, S. Ranvier, V.-M. Kolmonen, K. Haneda, and P. Vainikainen, "Long range wideband channel measurements at 81–86 GHz frequency range," in *4th European Conference on Antennas and Propagation (EUCAP)*. IEEE, 2010.

[142] M. Kyro, V.-M. Kolmonen, and P. Vainikainen, "Experimental propagation channel characterization of mm-wave radio links in urban scenarios," *IEEE Antennas and Wireless Propagation Letters*, vol. 11, pp. 865–868, 2012.

[143] R. Naderpour, J. Vehmas, S. Nguyen, J. Järveläinen, and K. Haneda, "Spatio-temporal channel sounding in a street canyon at 15, 28 and 60 GHz," in *27th Annual International Symposium on Personal, Indoor, and Mobile Radio Communications (PIMRC)*. IEEE, 2016.

[144] M. D. Balde, J. Vehmas, S. L. Nguyen, K. Haneda, H. Houas, and B. Uguen, "A 32 GHz urban micro cell measurement campaign for 5G candidate spectrum region," in *11th European Conference on Antennas and Propagation (EUCAP)*. IEEE, 2017, pp. 1803–1807.

[145] P. Aikio, R. Gruber, and P. Vainikainen, "Wideband radio channel measurements for train tunnels," in *48th Vehicular Technology Conference (VTC). Pathway to Global Wireless Revolution (Cat. No. 98CH36151)*, vol. 1. IEEE, 1998, pp. 460–464.

[146] L. Vuokko, V.-M. Kolmonen, J. Salo, and P. Vainikainen, "Measurement of large-scale cluster power characteristics for geometric channel models," *IEEE Transactions on Antennas and Propagation*, vol. 55, no. 11, pp. 3361–3365, 2007.

[147] O. Renaudin, V.-M. Kolmonen, P. Vainikainen, and C. Oestges, "Non-stationary narrowband MIMO inter-vehicle channel characterization in the 5-GHz band," *IEEE Transactions on Vehicular Technology*, vol. 59, no. 4, pp. 2007–2015, 2010.

[148] ——, "Wideband measurement-based modeling of inter-vehicle channels in the 5-GHz band," *IEEE Transactions on Vehicular Technology*, vol. 62, no. 8, pp. 3531–3540, 2013.

[149] M. Hata, "Empirical formula for propagation loss in land mobile radio services," *IEEE Transactions on Vehicular Technology*, vol. 29, no. 3, pp. 317–325, August 1980.

[150] Y. Okumura, E. Ohmori, T. Kawano, and K. Fukuda, "Field strength and its variability in VHF and UHF land-mobile radio service," *Review of the Electrical Communications Laboratory*, vol. 16, pp. 825–873, September 1968.

[151] J. Walfisch and H. Bertoni, "A theoretical model of UHF propagation in urban environments," *IEEE Transactions on Antennas and Propagation*, vol. 36, no. 12, pp. 1788–1796, 1988.

[152] F. Ikegami, T. Takeuchi, and S. Yoshida, "Theoretical prediction of mean field strength for urban mobile radio," *IEEE Transactions on Antennas and Propagation*, vol. 39, no. 3, pp. 299–302, 1991.

[153] E. Damosso and L. E. Correia, "Digital mobile radio towards future generation systems communications," COST 231 Final Report, CEC, Brussels, Belgium, Tech. Rep., 1999. [Online]. Available: http://www.lx.it.pt/cost231

[154] A. Motley and J. Keenan, "Personal communication radio coverage in buildings at 900 MHz and 1700 MHz," *Electronics Letters*, vol. 24, pp. 763–764, June 1988. [Online]. Available: https://digital-library.theiet.org/content/journals/10.1049/el_19880515

[155] S. R. Saunders and A. Aragon-Zavala, *Antennas and propagation for wireless communication systems*, 1st ed. Chichester: Wiley cop., 2007.

[156] A. Saleh and R. Valenzuela, "A statistical model for indoor multipath propagation," *IEEE Journal on Selected Areas in Communications*, vol. 5, no. 2, pp. 128–137, 1987.

[157] G. Turin, F. Clapp, T. Johnston, S. Fine, and D. Lavry, "A statistical model of urban multipath propagation," *IEEE Transactions on Vehicular Technology*, vol. 21, no. 1, pp. 1–9, 1972.

[158] H. Suzuki, "A statistical model for urban radio propogation," *IEEE Transactions on Communications*, vol. 25, no. 7, pp. 673–680, 1977.

[159] S. Venkatesh, J. Ibrahim, and R. Buehrer, "A new 2-cluster model for indoor UWB channel measurements," in *Antennas and Propagation Society Symposium*, vol. 1. IEEE, 2004, pp. 946–949 Vol.1.

[160] A. Molisch and F. Tufvesson, *Multipath propagation models for broadband wireless systems*. CRC Press, 2004, pp. 2.1–2.43.

[161] B. Fleury, "An uncertainty relation for WSS processes and its application to WSSUS systems," *IEEE Transactions on Communications*, vol. 44, no. 12, pp. 1632–1634, 1996.

[162] B. Van Veen and K. Buckley, "Beamforming: a versatile approach to spatial filtering," *IEEE ASSP Magazine*, vol. 5, no. 2, pp. 4–24, 1988.

[163] H. Krim and M. Viberg, "Two decades of array signal processing research: the parametric approach," *IEEE Signal Processing Magazine*, vol. 13, no. 4, pp. 67–94, 1996.

[164] M. S. Bartlett, "Periodogram analysis and continous spectra," *Biometrika*, vol. 37, no. 1–2, pp. 1–16, 06 1950. [Online]. Available: https://doi.org/10.1093/biomet/37.1-2.1

[165] R. Roy and T. Kailath, "ESPRIT-estimation of signal parameters via rotational invariance techniques," *IEEE Transactions on Acoustics, Speech, and Signal Processing*, vol. 37, no. 7, pp. 984–995, 1989.

[166] R. Schmidt, "Multiple emitter location and signal parameter estimation," *IEEE Transactions on Antennas and Propagation*, vol. 34, no. 3, pp. 276–280, 1986.

[167] D. Spielman, A. Paulraj, and T. Kailath, "Performance analysis of the MUSIC algorithm," in *International Conference on Acoustics, Speech, and Signal Processing (ICASSP)*, vol. 11, 1986, pp. 1909–1912.

[168] J. Capon, "High-resolution frequency-wavenumber spectrum analysis," *Proceedings of the IEEE*, vol. 57, no. 8, pp. 1408–1418, 1969.

[169] J. Fessler and A. Hero, "Space-alternating generalized expectation-maximization algorithm," *IEEE Transactions on Signal Processing*, vol. 42, no. 10, pp. 2664–2677, 1994.

[170] A. Richter, M. Landmann, and R. Thomä, "RIMAX-a flexible algorithm for channel parameter estimation from channel sounding measurements," *COST273, TD (04)*, vol. 45, pp. 26–28, 2004.

[171] A. Richter and R. Thoma, "Joint maximum likelihood estimation of specular paths and distributed diffuse scattering," in *61st Vehicular Technology Conference (VTC)*, vol. 1. IEEE, 2005, pp. 11–15.

[172] P. Almers, E. Bonek, A. Burr, N. Cznik, M. Debbah, V. Deglo-Esposti, H. Hofstetter, P. Kyösti, D. Laurenson, G. Matz, A. Molisch, C. Oestges, and H. Özcelik, "Survey of channel and radio propagation models for wireless MIMO systems," *EURASIP Journal on Wireless Communications and Networking*, pp. 1–19, 2007.

[173] A. Roivainen, "Three-dimensional geometry-based radio channel model: parameterization and validation at 10 GHz," Doctoral thesis, Faculty of Information Technology and Electrical Engineering, Communications Engineering, University of Oulu, 2017. [Online]. Available: http://urn.fi/urn:isbn:9789526215549

[174] J.-P. Kermoal, L. Schumacher, K. I. Pedersen, P. E. Mogensen, and F. Frederiksen, "A stochastic mimo radio channel model with experimental validation," *IEEE Journal on Selected Areas in Communications*, vol. 20, no. 6, pp. 1211–1226, 2002.

[175] W. Weichselberger, M. Herdin, H. Ozcelik, and E. Bonek, "A stochastic MIMO channel model with joint correlation of both link ends," *IEEE Transactions on Wireless Communications*, vol. 5, no. 1, pp. 90–100, 2006.

[176] W. C. Gibson, *The method of moments in electromagnetics*. Chapman and Hall/CRC, 2021.

[177] O. Zienkiewicz, R. Taylor, and J. Zhu, *The finite element method: its basis and fundamentals*. Elsevier Science, 2005.

[178] K. Yee, "Numerical solution of initial boundary value problems involving maxwell's equations in isotropic media," *IEEE Transactions on Antennas and Propagation*, vol. 14, no. 3, pp. 302–307, 1966.

[179] A. Taflove, "Application of the finite-difference time-domain method to sinusoidal steady-state electromagnetic-penetration problems," *IEEE Transactions on Electromagnetic Compatibility*, vol. 22, no. 3, pp. 191–202, 1980.

[180] A. Taflove and S. Hagness, *Computational electrodynamics: the finite-difference time-domain method*, ser. Artech House Antennas and Propagation Library. Artech House, 2005.

[181] REMCOM, "Wireless InSite: 3D Wireless Prediction Software," November 2022. [Online]. Available: https://www.remcom.com/wireless-insite-em-propagation-software

[182] Wavecall, "Wavesight: Raytracing Software," November 2022. [Online]. Available: https://www.wavecall.com/wavesight/

[183] Altair, "Winprop Telecom," November 2022. [Online]. Available: https://web.altair.com/winprop-telecom

[184] SIRADEL, "Volcano," November 2022. [Online]. Available: https://www.siradel.com/telecommunications/volcano/

[185] V. Degli-Esposti, D. Guiducci, A. de'Marsi, P. Azzi, and F. Fuschini, "An advanced field prediction model including diffuse scattering," *IEEE Transactions on Antennas and Propagation*, vol. 52, no. 7, pp. 1717–1728, 2004.

[186] J. Pyhtila, P. Sangi, H. Karvonen, M. Berg, R. Lighari, E. Salonen, A. Parssinen, and M. Juntti, "3-D Ray tracing based GPU accelerated field prediction radio channel simulator," in *89th Vehicular Technology Conference (VTC)*. IEEE, 2019.

[187] J. Järveläinen, K. Haneda, and A. Karttunen, "Indoor propagation channel simulations at 60 GHz using point cloud data," *IEEE Transactions on Antennas and Propagation*, vol. 64, no. 10, pp. 4457–4467, 2016.

[188] J. Järveläinen, "Measurement-based millimeter-wave radio channel simulations and modeling," Doctoral thesis, School of Electrical Engineering, Aalto University, 2016. [Online]. Available: http://urn.fi/URN:ISBN:978-952-60-6972-2

[189] P. Koivumäki, G. Steinböck, and K. Haneda, "Impacts of point cloud modeling on the accuracy of ray-based multipath propagation simulations," *IEEE Transactions on Antennas and Propagation*, vol. 69, no. 8, pp. 4737–4747, 2021.

[190] J.-M. Jin, F. Ling, S. T. Carolan, J. M. Song, W. C. Gibson, W. C. Chew, C.-C. Lu, and R. Kipp, "A hybrid SBR/MoM technique for analysis of scattering from small protrusions on a large conducting body," *IEEE Transactions on Antennas and Propagation*, vol. 46, no. 9, pp. 1349–1357, 1998.

[191] Y. Wang, S. Safavi-Naeini, and S. K. Chaudhuri, "A hybrid technique based on combining ray tracing and FDTD methods for site-specific modeling of indoor radio wave propagation," *IEEE Transactions on Antennas and Propagation*, vol. 48, no. 5, pp. 743–754, 2000.

[192] J. Fuhl, A. F. Molisch, and E. Bonek, "Unified channel model for mobile radio systems with smart antennas," *IEE Proceedings-Radar, Sonar and Navigation*, vol. 145, no. 1, pp. 32–41, 1998.

[193] P. Petrus, J. H. Reed, and T. S. Rappaport, "Geometrical-based statistical macrocell channel model for mobile environments," *IEEE Transactions on Communications*, vol. 50, no. 3, pp. 495–502, 2002.

[194] H. Hofstetter and G. Steinbock, "A geometry-based stochastic channel model for MIMO systems," in *ITG Workshop on Smart Antennas (IEEE Cat. No. 04EX802)*. IEEE, 2004, pp. 194–199.

[195] A. F. Molisch, A. Kuchar, J. Laurila, K. Hugl, and R. Schmalenberger, "Geometry-based directional model for mobile radio channels—principles and implementation," *European Transactions on Telecommunications*, vol. 14, no. 4, pp. 351–359, 2003.

[196] A. F. Molisch, "A generic model for MIMO wireless propagation channels in macro-and microcells," *IEEE Transactions on Signal Processing*, vol. 52, no. 1, pp. 61–71, 2004.

In an era where the invisible threads of communication weave our world together, the realm of wireless connectivity stands as an essential cornerstone of modern life. At the heart of this intricate web lies the enigmatic radio channel – a conduit through which signals traverse, bridging distances and connecting lives. But the radio channel is far from a simple conduit; it is a dynamic and ever-shifting medium that demands understanding, prediction, and optimization. This is where the art and science of radio channel modeling and characterization step onto the stage, guiding us through the complex dance of signals and revealing pathways to enhanced communication. It is fundamental in advancing wireless communication technologies and crucial for designing robust systems that deliver consistent and efficient communication experiences, shaping the future of wireless connectivity. This thesis focuses on modeling the interaction of radio waves with the material objects in radio environments and characterizing multipath radio channels at centimeter and millimeter wave frequencies.

Aalto-DT 136/2023

ISBN 978-952-64-1408-9 (printed)
ISBN 978-952-64-1409-6 (pdf)
ISSN 1799-4934 (printed)
ISSN 1799-4942 (pdf)

Aalto University
School of Electrical Engineering
Department of Electronics and Nanoengineering
www.aalto.fi

BUSINESS + ECONOMY

ART + DESIGN + ARCHITECTURE

SCIENCE + TECHNOLOGY

CROSSOVER

DOCTORAL THESES